Improving accuracy of information extraction from quantitative magnetic resonance imaging

Valentin Hamy

Centre for Medical Imaging

Department of Medical Physics and Bio-engineering

University College London

A dissertation submitted in partial fulfilment

of the requirements for the degree of

Doctor of Philosophy

of

University College London

2014

I, Valentin Hamy confirm that the work presented in this thesis is my own. Where information has been derived from other sources, I confirm that this has been indicated in the thesis.

Abstract

Quantitative MRI offers the possibility to produce objective measurements of tissue physiology at different scales. Such measurements are highly valuable in applications such as drug development, treatment monitoring or early diagnosis of cancer. From microstructural information in diffusion weighted imaging (DWI) or local perfusion and permeability in dynamic contrast (DCE-) MRI to more macroscopic observations of the local intestinal contraction, a number of aspects of quantitative MRI are considered in this thesis. The main objective of the presented work is to provide pre-processing techniques and model modification in order to improve the reliability of image analysis in quantitative MRI.

Firstly, the challenge of clinical DWI signal modelling is investigated to overcome the biasing effect due to noise in the data. Several methods with increasing level of complexity are applied to simulations and a series of clinical datasets. Secondly, a novel Robust Data Decomposition Registration technique is introduced to tackle the problem of image registration in DCE-MRI. The technique allows the separation of tissue enhancement from motion effects so that the latter can be corrected independently. It is successfully applied to DCE-MRI datasets of different organs. This application is extended to the correction of respiratory motion in small bowel motility quantification in dynamic MRI data acquired during free breathing. Finally, a new local model for the arterial input function (AIF) is proposed. The estimation of the arterial blood contrast agent concentration in DCE-MRI is augmented using prior knowledge on local tissue structure from DWI.

This work explores several types of imaging using MRI. It contributes to clinical quantitative MRI analysis providing practical solutions aimed at improving the accuracy and consistency of the parameters derived from image data.

Acknowledgment

During my experience as a PhD student I have had the occasion to meet and interact with a number of people who supported me in many different ways. Firstly I would like to thank my principal supervisor David Atkinson for his help and advices all along this experience. I also thank my fellow research student Alex Menys for discussing ideas, and sharing his views and ambitions with me. More generally, I would like to thank all the members the UCL Centre for Medical Imaging for sharing this experience with me.

I also would like to thank all my friends who also do or did a PhD for sharing the many good (and the few less good) moments with me. I particularly want to thank my sisters and brothers: Clotilde, Agathe, Alexandre and Antoine as well as my girlfriend Julie for their interest in my work and their constant moral support. I finally want to thank my parents for their invaluable help and support at many occasions during these three and a half years.

The work presented in this thesis was supported by the National Institute for Health Research University College London Hospitals Biomedical Research Centre.

List of publications

Journal papers:

Dikaios, N; Arridge, S; Hamy, V; Punwani, S; Atkinson, D; (2014) Direct parametric reconstruction from undersampled (k, t)-space data in dynamic contrast enhancement MRI. (Submitted to Med Image Anal)

Menys, A*; Hamy, V*; Hoad, C; Makanyanga, J; Odille, F; Gowland, P; Taylor, S; Atkinson, D; (2014) Dual Registration of Abdominal Motion in free-breathing datasets acquired using dynamic MRI. (Submitted to Physics in Medicine and Biology).**Joint contribution*

Hamy, V; Dikaios, N; Punwani, S; Melbourne, A; Latifoltojar, A; Makanyanga, J; Chouhan, M; Helbren, E; Menys, A; Taylor, S; Atkinson, D; (2014) Respiratory motion correction in dynamic MRI using robust data decomposition registration - Application to DCE-MRI. Med Image Anal 2014, 18 (2) pp. 301 - 313.

Hamy, V; Menys, A; Helbren, E; Odille, F; Punwani, S; Taylor, S; Atkinson, D; (2013) Respiratory motion correction in dynamic-MRI: Application to small bowel motility quantification during free breathing. In: Lecture Notes in Computer Science. (pp. 132 - 140).

Dikaios, N; Punwani, S; Hamy, V; Purpura, P; Rice, S; Forster, M; Mendes, R; Taylor, S; Atkinson, D; (2013) Noise estimation from averaged diffusion weighted images: Can unbiased quantitative decay parameters assist cancer evaluation? Magnetic Resonance in Medicine 2013. *(in press)*

Conference proceedings:

Hoad, C; Hamy, V; Garsed, K; Marciani, L; Spiller, R; Taylor, S; Atkinson, D; Gowland, P; Menys, A; (2014) Preliminary investigations of colonic motility from Cine MRI; use of registration techniques for quantitative analysis. In: (Proceedings) ISMRM 2014. *(accepted abstract)*

Menys, A; Hamy, V; Hoad, C; Makanyanga, J; Odille, F; Gowland, P; Taylor, S; Atkinson, D; (2014) Dual Registration of Abdominal Motion in free-breathing data sets acquired using dynamic MRI. In: (Proceedings) ISMRM 2014. *(accepted abstract)*

Hamy, V; Modat, M; Dikaios, N; Cleary, J; Punwani, S; Shipley, R; Ourselin, S; Atkinson, D; Melbourne, A; (2014) Multi-modal pharmacokinetic modelling for DCE-MRI: using diffusion weighted imaging to constrain the local arterial input function. In: (Proceedings) SPIE Medical Imaging 2014. *(in press)*

Dikaios, N; Tremoulhéac, B; Menys, A; Hamy, V; Arridge, S; Atkinson, D; (2013) Joint reconstruction of low-rank and sparse components from undersampled (k, t)-space small bowel data. In: (Proceedings) IEEE MIC 2013. *(in press)*

Johnson, A; Latifoltojar, A; Hamy, V; Punwani, S; Shmueli, K; (2013) Characterising the Contribution of Hypoxia to R2* Differences between Prostate Tumours and Normal Tissue. In: (Proceedings) ISMRM 2013, pp. 919.

Hamy, V; Punwani, S; Makanyanga, J; Taylor, S; Atkinson, D; (2013) Motion Correction in Small Bowel DCE-MRI using Robust Data Decomposition Registration. In: (Proceedings) ISMRM 2013, pp. 2705.

Dikaios, N; Hamy, V; Punwani, S; Atkinson, D; (2013) Noise estimation for averaged DW MR images. In: (Proceedings) ISMRM 2013, pp. 2080.

Hamy, V; Melbourne, A; Trémoulhéac, B; Punwani, S; Atkinson, D; (2012) Registration of DCE-MRI using Robust Data Decomposition. In: (Proceedings) ISMRM 2012. pp. 749.

Hamy, V; Walker-Samuel, S; Atkinson, D; Punwani, S; (2012) Apparent diffusion coefficient estimation in prostate DW-MRI using maximum likelihood. In: (Proceedings) ISMRM 2012. pp. 1854.

Dikaios, N; Punwani, S; Hamy, V; Purpura, P; Fitzke, H; Rice, S; Taylor, S; Atkinson, D; (2012) Maximum likelihood ADC parameter estimates improve selection of metastatic cervical nodes for patients with head and neck squamous cell cancer. In: (Proceedings) ISMRM 2012. pp. 3579.

Hamy, V; Atkinson, D; Walker-Samuel, S; Punwani, S; (2011) Comparison of least squares and maximum likelihood for apparent diffusion coefficient estimation in prostate diffusion-weighted MRI (DW-MRI). In: (Proceedings) RSNA 2011.

Hamy, V; Walker-Samuel, S; Punwani, S; Atkinson, D; (2011) Comparison of least squares and maximum likelihood for apparent diffusion coefficient estimation in prostate DW-MRI. In: (Proceedings) MIUA 2011.

Abbreviations

MRI	Magnetic Resonance Imaging
NMR	Nuclear Magnetic Resonance
RF	Radio Frequency
GRAPPA	GeneRalized Autocalibrating Partially Parallel Acquisitions
SENSE	Sensitivity Encoding
SE	Spin Echo
GE	Gradient Echo
SGE	Spoilt Gradient Echo
EPI	Echo Planar Imaging
bSSFP	balanced Steady State Free Precession
DWI	Diffusion Weighted Imaging
ADC	Apparent Diffusion Coefficient
CT	Computed Tomography
Gd	Gadolinium
Gd-DTPA	Gadolinium in Diethylene Triamine Pentaacetic Acid
DCE	Dynamic Contrast Enhanced (-MRI)
EES	Extracellular Extravascular Space
AIF	Arterial Input Function
DSC	Dynamic Susceptibility Contrast (-MRI)
ASL	Arterial Spin Labelling
ROI	Region Of Interest
SNR	Signal to Noise Ratio
PDF	Probability Density Function
SOS	Sum Of Squares
SMF	Spatial Matched Filter
LS	Least Squares

ML	Maximum Likelihood
MD	Median
MP	Maximum Probability
PZ	Peripheral Zone
TZ	Transition Zone
FT	Fourier Transform
SSD	Sum of Squares Difference
CC	Correlation Coefficients
MI	Mutual Information
NMI	Normalized Mutual Information
FFD	Free Form Deformation
PPCR	Progressive Principal Component Registration
PCA	Principal Component Analysis
RPCA	Robust Principal Component Analysis
SVD	Singular Value Decomposition
IALM	Inexact Augmented Lagrangian Multiplier
RC	Residual Complexity
DCT	Discrete Cosine Transform
GT	Ground Truth
TIC	Time Intensity Curve
RMSE	Root Mean Squared Error
AUC_{60}	Area Under the Curve (for 60 seconds after bolus arrival)
OF	Optical Flow registration
DRAM	Dual Registration of Abdominal Motion
BTFE	Balanced Turbo Field Echo
BA	Bland Altman
LoA	Limit of Agreement

TRE	Target Registration Error
FOV	Field Of View

Table of contents

List of Figures

List of Tables

1 Introduction

Magnetic resonance imaging (MRI) is a non-invasive and relatively new medical imaging technique. It is based on nuclear magnetic resonance and thus avoids the use of ionising radiation, contrary to other modalities based on X-rays or radioactive isotopes. In addition to this characteristic, MRI has the advantage of providing good soft-tissue contrast and making possible the acquisition in any direction of space.

In traditional qualitative MRI, the scanner is used as a sophisticated camera providing images that can only be read by a trained radiologist. Alternatively, using specific acquisition methods, MRI scanners can serve as a measurement tool providing information directly related to one or more aspects of tissue physiology. That way, morphological evaluation of traditional MR sequences (e.g. T1 or T2 weighted) can be augmented by functional and micro-structural measures coming from quantitative MRI. In processes such as diagnosis, therapy monitoring, tumour staging or even cross-site comparison, quantitative information is the key.

Quantitative MRI is an important area of research and includes different types of acquisition such as Diffusion Weighted MRI or Dynamic Contrast Enhanced MRI which have aroused considerable interest in recent years. These techniques are capable of characterising tissue and facilitating new opportunities in imaging. For example, early prediction of treatment response based on the assessment of cellularity and tissue perfusion prior to morphologic alterations appear among the main applications of multi-parametric quantitative MRI.

However, extracting useful information from the acquired data often requires the use of a model describing the observed mechanisms (e.g. diffusion weighted signal decay, contrast enhancement in tissue) and involves pre-processing to account for perturbations occurring during the acquisition (e.g. noise, motion). The different projects presented in this thesis focus on the description of issues related to both the pre-processing and the modelling step and solutions proposed to address these challenges.

Following this introduction, the second chapter provides a theoretical description of the different MRI based quantitative imaging techniques used during this PhD. In each case, both data acquisition and analysis are presented. A summary of a number of challenges related to quantitative MRI is then described.

In the third chapter, the nature and effects of noise in DW-MRI are discussed. Depending on the acquisition strategy (e.g. number of receiving coils, reconstruction technique, use of image averaging) the nature of noise in magnitude diffusion weighted images can vary. Such a noise induces a bias in the estimation of relevant parameters and should be investigated. The proposed solutions utilise noise modelling methods applied to simulations and to different types of patient data (18 prostate, 40 head and neck cancer) to assess the impact of the bias correction in a clinical context.

Chapter four is about motion correction in DCE-MRI. The monitoring of contrast uptake and washout in tissue requires long scan times (several minutes) and image misalignments arise due to patient motion during the acquisition. Such misalignments can cause errors in the modelling of tissue enhancement and therefore should be corrected for. Although many registrations techniques are available these often rely on intensity changes to align features and can be misled by contrast enhancement, potentially resulting in unrealistic deformations. A novel registration technique based on data decomposition introduced and defined as: Robust Data Decomposition Registration (RDDR). The application of RDDR to a total of 57 DCE-MRI data sets for comparison with other existing methods is presented. The data processed cover a range of imaged organs (liver, small bowel and prostate) and breathing protocols (multiple breath-holds, free breathing).

Some properties of RDDR are of interest in other types of data as discussed in the fifth chapter. For example, bowel motility can be quantified from abdominal dynamic MRI acquired during breath-hold. However, for data acquired during free breathing, respiratory motion can confound the analysis. The use of data decomposition in RDDR allows for the separation of peristalsis from respiratory motion, so that the latter can be corrected for while preserving the former. Experiments include the application of RDDR to dynamic MR

scans of 20 healthy subjects to assess the benefit of using it as a pre-processing step for peristaltic motility quantification in data acquired during free breathing.

The last chapter describes a study combining the work undertaken on both DW-MRI and DCE-MRI, with a focus on DCE-MRI modelling. Pharmacokinetic models require an Arterial Input Function (AIF) to provide information on the arrival and transit of the contrast agent bolus in tissue. However this AIF is often based on a population model or derived from a single source (e.g. major artery in the imaged field of view). This project investigates the potential benefit of incorporating local information on tissue microstructure obtained from DWI-MRI to obtain a specific AIF for each region. The proposed model is applied to head and neck scans from 27 subjects (18 patients and 9 healthy volunteers) and includes the previous work involving registration of DCE-MRI data with RDDR and analysis of DW-MR images using noise modelling. The effect of using a local AIF was assessed based on parametric mapping (e.g. K^{Trans}) in normal/cancer lymph nodes and residual fitting errors.

2 Quantitative MRI and Related Challenges

2.1 Introduction

This chapter introduces the context and key challenges addressed in this thesis. Morphological evaluation of traditional MR sequences can be augmented by functional and micro-structural measures coming from quantitative MRI. Such methods are capable of characterising tissue and facilitating new opportunities in imaging, for example early prediction of treatment response based on the assessment of cellularity and tissue perfusion prior to morphologic alterations. This often requires repeat imaging of the same anatomical features to monitor changes related to a certain mechanism or tissue characteristic. However factors with no link to the property of interest may also vary and bias the measurement. These must be accounted for in the analysis process. Subsequently a set of parameters can be derived from the data through the use of a specific mathematical model providing physiological description of the tissue.

In the following, a brief description of the concept of magnetic resonance imaging is given along with a more specific presentation of the different types of quantitative MRI techniques used in this thesis. These include: Dynamic Contrast Enhanced MRI, Diffusion Weighted Imaging and dynamic imaging of the small bowel. The different issues, related to both data acquisition and analysis, are also introduced.

2.2 Magnetic Resonance imaging (MRI)

2.2.1 History

MRI is based on nuclear magnetic resonance (NMR). In physics, resonance corresponds to the sensitivity of some systems to a certain frequency: excitation at this resonance frequency causes the system to enter an oscillating regime before returning to its initial state. More particularly, NMR describes the fact that protons immersed in a static magnetic field can be excited by a varying field at the resonance frequency (which is proportional to

the field strength). This phenomenon was discovered in the late 1930's by Rabi and experimented upon for the first time in the mid 1940's by Bloch and Purcell independently [1]. In the early 1970's Damadian highlighted that different types of tissue (e.g. normal tissue and cancer) excited at the same frequency have different resonance characteristics [1]. This opened the era of MRI for medical use. Following such a discovery many research groups started developing techniques and systems of acquisition (e.g. field gradient for local NMR localization, Lauterbur 1973 [2]; high field scanners, 1984) leading to modern MRI and its generalisation in clinical practice. Nowadays MRI has become a very common imaging tool used for multiple purposes (e.g. diagnosis, surgery planning, and follow up of treatment) and presents a range of acquisition techniques.

2.2.2 Principle

The principle of MRI derives from quantum physics. Hydrogen nuclei (from water representing 70% of human body mass) possess an intrinsic angular momentum or spin. These spins act like magnetic dipoles. In the absence of an external magnetic field, the different magnetic moments of neighbouring spins cancel out. However when immersed into a static magnetic field, $\vec{B}_0$ spins align in the same direction (that of $\vec{B}_0$) and precess at the Larmor frequency. This precession is described by the Bloch equation:

$$\frac{d\vec{\mu}}{dt} = \gamma\vec{\mu} \times \vec{B}_0 = \vec{w} \times \vec{\mu} \qquad (2.1)$$

$$\text{with } w = \gamma B_0$$

where w is the Larmor angular frequency, γ is the gyromagnetic ratio (42.58 $MHz.T^{-1}$ for protons i.e. hydrogen 1H) and $\vec{\mu}$ is the spin vector. In such a situation spins can either have the same orientation as $\vec{B}_0$ (spin up) or point in the opposite way (spin down). At body temperature the relative proportion of these two states is approximately the same with a slightly higher number of spins up, which results in a net magnetization.

Magnetic resonance occurs when a radiofrequency (RF) pulse at the Larmor frequency is applied. Changes in $\vec{B}$ stimulate the spins which causes a tipping of the precession angle followed by a return to the initial state called relaxation (see Figure 2.1). For a group of nuclei, all the spins have the same phase when excited by the RF pulse which results in a coherent transverse magnetization. The dephasing due to spins interaction during relaxation causes a loss of coherence and a decrease of this magnetization. In the presence of a receiver coil, the variation of the transverse magnetization produces a current which can be measured.

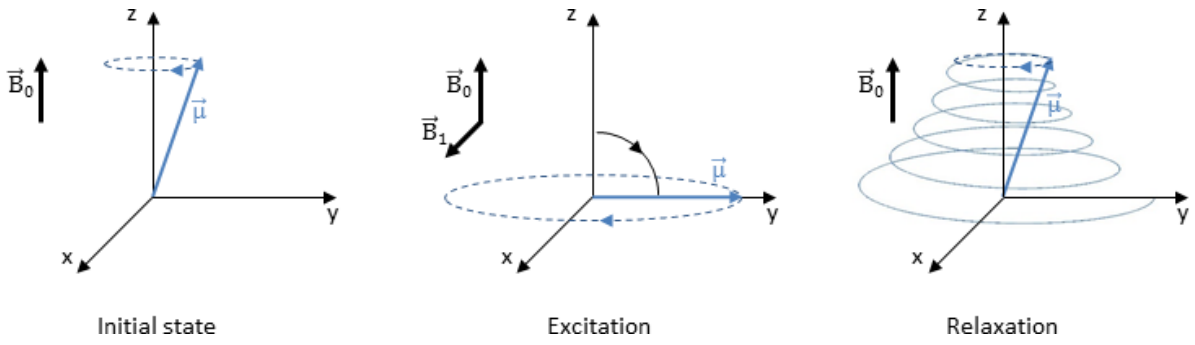

Figure 2.1: Effect of a radiofrequency pulse (here 90°) on a hydrogen nucleus spin. The presence of the pulse $\vec{B}_1$ tips the spin which then relaxes back to its initial state.

Such a relaxation can be decomposed into two mechanisms: longitudinal relaxation of the M_z component (along the Z axis in Figure 2.1), and transverse relaxation of the M_{xy} component (in the X-Y plane). Both depend on intrinsic characteristics of the magnetised body. M_z undergoes an exponential recovery characterised by the time constant T1. It corresponds to the spin lattice relaxation (i.e. how spins lose energy to the surroundings). M_{xy} undergoes an exponential decay characterised by the time constant T2. It corresponds to the spin-spin relaxation (i.e. exchange of energy between nearby molecules that act as coupled oscillators). However magnetic field inhomogeneities induce an additional dephasing of the spins which makes the decay of M_{xy} shorter (time constant $T2^* < T2$). Specific imaging sequences offer the possibility of removing the effect of field inhomogeneities to produce signals reflecting tissue T2 (see section 2.2.3.3).

2.2.3 Acquisition

2.2.3.1 Spatial encoding

To be able to spatially locate different types of tissue it is necessary to get separate signal from elementary volumes of space (voxels). In two-dimensional imaging, only one physical slice is excited at a time. Slice selection is achieved using a field gradient in conjunction with the RF pulse along a given axis of space (depending on the chosen acquisition plane) so that a thin slab of tissue is excited. Each element of the two-dimensional slice is then encoded in phase and frequency defining its k-space representation which establishes a link between the received signal and its origin in space. A phase encoding magnetic field gradient is applied for a short period of time along the k-space columns so that each line is assigned a different phase. Spatial encoding along the line is then achieved using a frequency encoding magnetic field gradient. Nuclei experience different field strength and thus resonate at different frequencies determined by their position in the line. Importantly, there is no restriction on the choice of slice orientation and the phase and frequency encoding can be assigned to any orthogonal directions. Since each imaged slice is encoded in the frequency domain, an inverse Fourier transform is used to retrieve image data. Three-dimensional acquisition can also be achieved by exciting a slab of tissue and applying phase encoding in two directions.

2.2.3.2 Hardware

Elements constituting an MRI scanner include: the magnet which is commonly a coil made of superconducting material immersed in liquid helium and carrying a high current to produce the magnetic field $\vec{B}_0$; the shim coils used to increase $\vec{B}_0$ homogeneity inside the scanner bore; the gradient coils producing the field gradients; and the radiofrequency coil which is used to produce the pulse and also to receive signals from tissue. Alternatively separate coils (e.g. surface coils, head coils) can be used instead of the latter to image specific body parts. However these are usually receive-only.

Note that the use of multiple receiver coils enable parallel imaging. Such a technique relies on limited acquisition in the phase encoding direction of k-space (i.e. under sampling) to increase acquisition speed. Provided that a sensitivity map is available for each coil, the information received by the different receiver coils can be combined to reconstruct the imaged data as if it had been fully sampled. Reconstruction can be carried out either in k-space (e.g. generalized auto-calibrated partially parallel acquisition - GRAPPA [3]) or in the image domain after inverse Fourier transform (e.g. sensitivity encoded MRI - SENSE [4])

2.2.3.3 Pulse sequences

In MRI, signals can be generated using either spin echo (SE) or gradient echo (GE) [1]. In the basic spin echo sequence (Figure 2.2) a 90^o RF pulse is first used to excite the hydrogen nuclei. After a certain time period during which the spins dephase naturally, an additional 180^o pulse is applied. Such a pulse inverts the dephasing causing a rephasing of the spins, or echo, after a period equal to the time lapse between the two pulses. The 180^o RF pulse cancels the static magnetic field inhomogeneities so that the received signal depends on T2 rather than T2*. The expression for the corresponding signal is given in equation (2.2).

$$S_{SE} \approx S_0 \left(1 - \exp(-TR/T_1)\right)\exp(-TE/T_2) \qquad (2.2)$$

where TR is the repetition time (i.e. the time between two successive 90^o RF pulses), TE is the echo time (i.e. the time between the 90^o RF pulse and the spin echo) and S_0 is the proton density. Depending on the values chosen for TR and TE, the contribution of the spin-lattice relaxation (T1-weighting), the spin-spin relaxation (T2-weighting) and the proton density to the output signal can be adjusted.

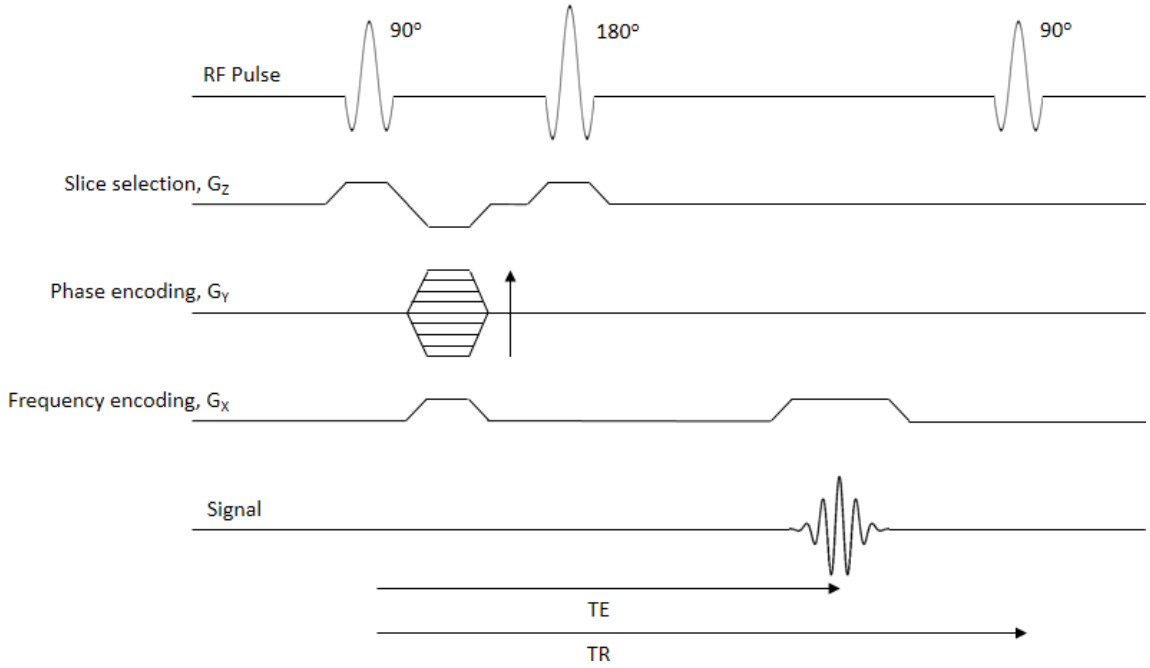

Figure 2.2: Time diagram of the basic spin echo sequence

In GE sequences (Figure 2.3) the RF pulse is set to produce a magnetisation rotation angle, α, lower than 90º and is combined with short TEs and TRs. A negative gradient is applied directly after the pulse and then reversed. When phase changes caused by the negative gradient are cancelled a gradient echo is produced (i.e. when the positive and negative gradient areas are equal). The signal obtained in this type of sequence depends on $T2^*$. However the time needed to produce an echo is much shorter compared to spin echo sequences. The expression for the corresponding signal (at steady state) is given in equation (2.3).

$$S_{GE} \approx S_0 \frac{(1-\exp(-TR/T_1))\sin(\alpha)}{1-\exp(-TR/T_1)\cos(\alpha)} \exp(-TE/T_2{}^*) \qquad (2.3)$$

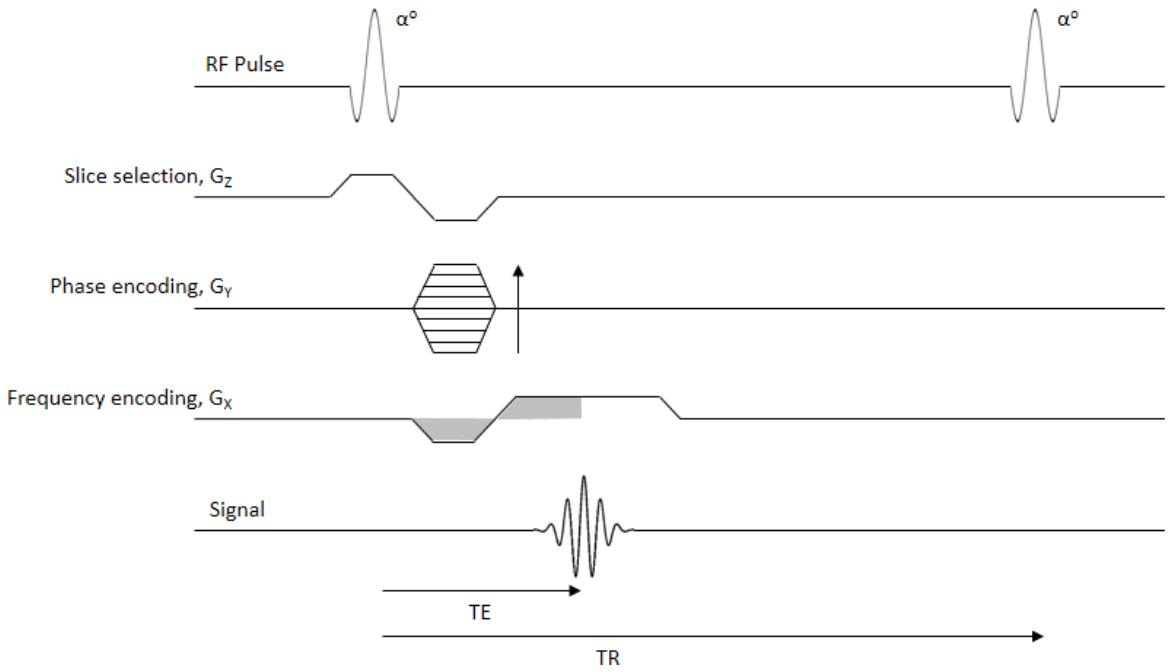

Figure 2.3: Time diagram of the basic gradient echo sequence

Many modifications of these two basic sequences have been proposed to further reduce the time required to obtain the desired signals [1]. In this thesis we focus on two particular examples: the spoiled gradient echo (SGE) and the echo planar imaging (EPI) sequences.

In SGE, the basic GE sequence is complemented by gradient spoilers and RF phase cycling (Figure 2.4) to destroy any remaining transverse magnetization after the echo, thus enabling the use of short TRs ($\sim 5\text{ms}$). Another type of pulse sequence referred to as balanced steady state free precession (bSSFP), uses balanced gradients (i.e. the area under each field gradient is zero over a TR period) which allows keeping part of the transverse magnetization from previous RF excitations. The kept magnetization contributes to the signal acquired in the subsequent repetitions of the sequence. This produces signals with both T1 and T2 weighting and high signal to noise ratio (SNR), which is especially useful for cine imaging.

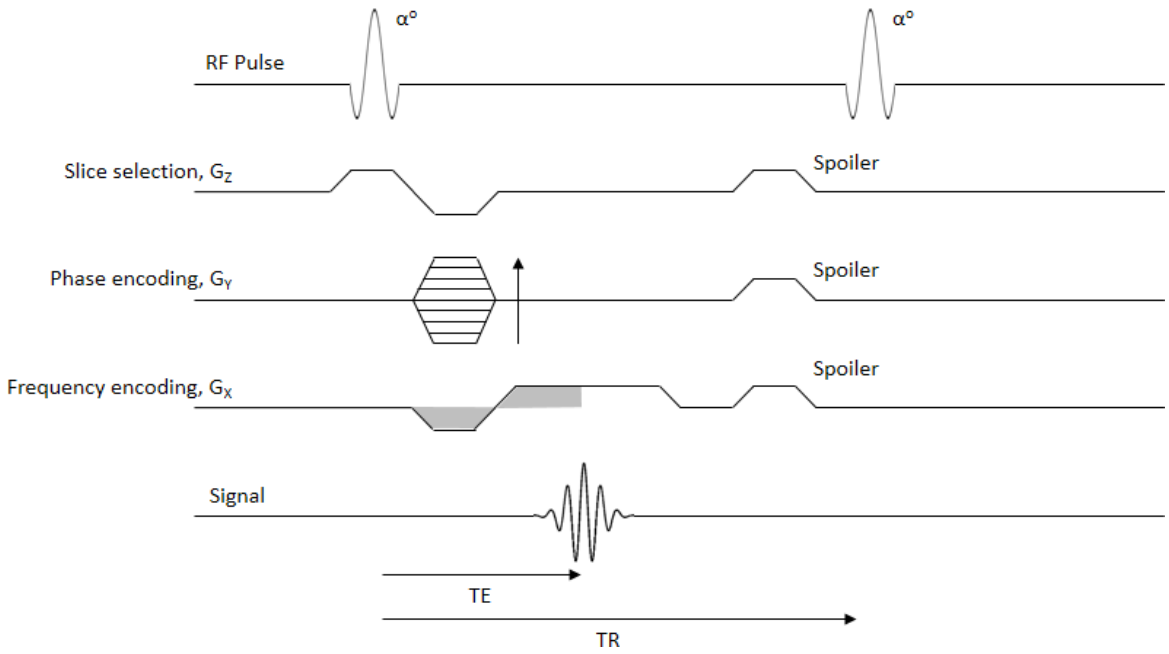

Figure 2.4: Time diagram of the spoiled gradient echo sequence

In EPI (see Figure 2.5), a single 90º RF pulse is applied, followed by multiple gradient reversals. A large negative phase encoding gradient is applied right after the RF pulse. Small positive phase encoding gradient are then applied after each gradient echo so that an entire slice can be acquired in a single shot.

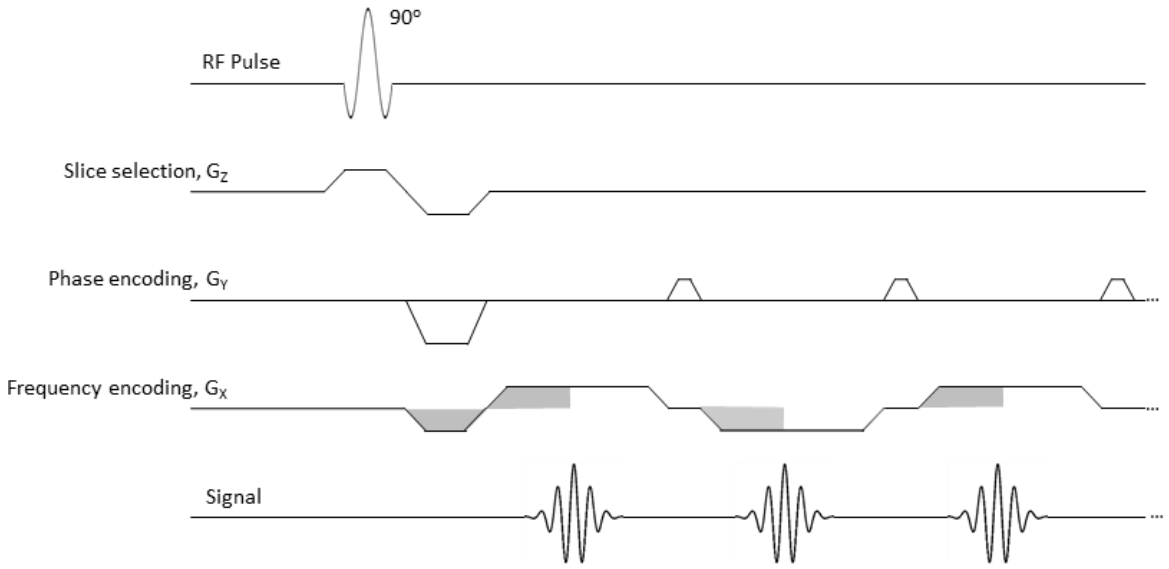

Figure 2.5: Time diagram of the (gradient) echo planar imaging sequence

The sequence shown Figure 2.5 uses gradient echo, and thus produces $T2^*$ weighted images. Alternatively, a single 180° RF refocusing pulse can be added before the first positive G_X gradient to produce a spin echo and obtain a T2 weighted signal. This timing also allows for the insertion of diffusion weighting gradients (see section 2.3.1)

2.3 Quantitative MRI: Diffusion Weighted MRI (DWI)

2.3.1 Principle

In the absence of constraints, water molecules undergo self-diffusion (i.e. Brownian motion). For a large ensemble of molecules over a certain time period the mean squared displacement depends on a diffusion coefficient D. In tissue, motion is restricted by cellular structures and therefore D is decreased. The degree of reduction of the diffusion coefficient reflects tissue microstructure and can be quantified in MRI.

In Diffusion Weighted Imaging (DWI) two high amplitude gradients are applied (along one direction of space) on either side of an 180° RF pulse (Figure 2.6). The presence of these gradients affects the spin echo obtained at the end of the sequence. Moving molecules acquire a dephasing which is proportional to their displacement along the gradient direction. The greater the displacement in the direction of the gradient, the larger the dephasing. As spins are moving randomly, rapid diffusion causes larger phase dispersion between the individual spins, which produces a drop in signal. On the contrary, in the case of slow or restricted diffusion the relative dephasing between spins is more limited which results in a higher signal.

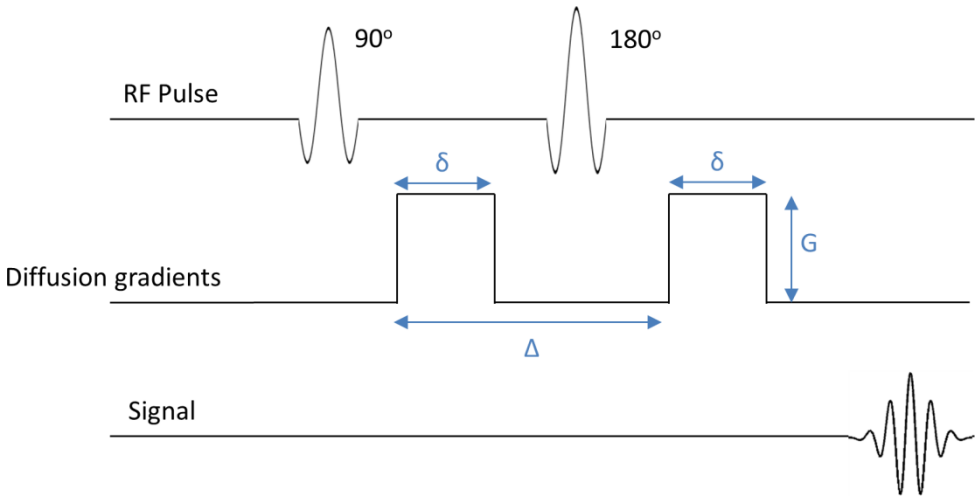

Figure 2.6: Time diagram of the Diffusion Weighted MRI sequence. G is the gradient amplitude, δ the duration, and Δ the front edge separation. The signal readout, not detailed in this diagram, is often an EPI module.

By manipulating the different characteristics of these gradients (direction, amplitude G, duration δ, and front edge separation Δ) the diffusion weighting or b-value, can be controlled. Such a parameter is varied to assess the degree of diffusion in tissue in a given direction. Repeat measurements at different b-values (see Figure 2.7) in different directions allow the extraction of the apparent diffusion coefficient (ADC) reflecting the local microstructure. The expression for the b-value is given in equation (2.4).

$$b = \gamma^2 G^2 \delta^2 \left(\Delta - {}^{\delta}/_{3}\right) \text{ in s.mm}^{-2} \qquad (2.4)$$

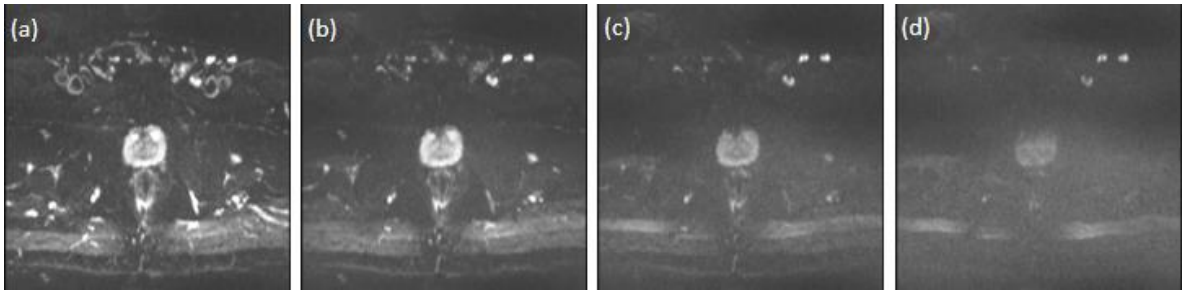

Figure 2.7: Example of DWI data of the prostate at b-values: 0 (a), 150 (b), 500 (c) and 1000 s.m^{-2} (d).

In DWI, images are generally acquired in three directions of space and combined into a "trace" image producing data at a given b-value. However in applications such as Diffusion Tensor Imaging measurement in multiple direction of space (at least 6) can be used to produce a tensor at each voxel, and a mapping of fibre tracts in the tissue of interest (e.g. white matter) following eigenvalue decomposition. Because a high number of

measurements is necessary to obtain a full DWI data set (multiple directions and b-values per slice), spin echo EPI acquisition is usually chosen due to its speed.

2.3.2 Diffusion modelling

Several models have been proposed to describe the decay of the DWI magnitude signal as a function of increasing b-values. These assume that diffusion weighted signals are related to one or several mechanisms with different degrees of complexity, taking place at a microstructural level. Each model applies to pixels in trace images which are insensitive to anisotropy.

2.3.2.1 Mono-exponential

The simplest way of describing the diffusion weighted magnitude signal decay is an exponential model:

$$S(b) = S_0 \exp(-bD) \tag{2.5}$$

where S is the signal at a given b-value b, S_0 is the signal intensity when no diffusion weighting is applied (i.e. at $b = 0$), and D is the ADC.

2.3.2.2 Bi-exponential: Intra Voxel Incoherent Motion (IVIM)

LeBihan et al. [5], [6] introduced a bi-exponential model that accounts for tissue perfusion and blood microcirculation at a pixel level.

$$S(b) = S_0(f \exp(-bD^*) + (1 - f) \exp(-bD)) \tag{2.6}$$

where D is the ADC, D^* is an additional pseudo diffusion parameter accounting for the perfusion effect (mainly present at lower b values) and f is the perfusion fraction.

2.3.2.3 Stretched Exponential

The stretched exponential model was developed to account for intra-voxel heterogeneity in diffusion weighted signal decay [7] with no restriction on the number of compartments.

$$S(b) = S_0 \ \exp(-bD)^{\alpha}$$
$$0 \leq \alpha \leq 1 \tag{2.7}$$

where D is the distributed diffusion coefficient (which is related to the ADC), and α is the stretching parameter that characterizes the deviation from a mono-exponential decay.

2.3.3 Applications

DWI is used in oncology for tumour grading and follow up of treatment. The microstructural properties of cancerous tissue such as changes in cellularity can be indirectly measured in DWI and provide useful contrast difference between normal and tumour region. Another important clinical application is the investigation, prognosis and management of ischaemic strokes [1]. In this context DWI provides useful information on the type of stroke (e.g. chronic, acute) earlier than other imaging techniques (CT, T2 weighted MRI).

2.4 **Quantitative MRI: Dynamic Contrast Enhanced MRI**

2.4.1 Principle

Contrast agents can be used to provide additional information on tissue metabolism and improve sensitivity and specificity. The most common paramagnetic contrast agent is G gadolinium (Gd) encapsulated in a chelating agent, for example diethylene-triamine pentaacetic acid (Gd-DTPA). Gd is not directly visible in MRI but its presence affects the relaxation characteristics of surrounding water molecules (decreased T1 and T2).

In dynamic contrast enhanced (DCE-) MRI we are interested in the T1 decrease caused by Gd. A contrast agent dose is injected through a vein, and its arrival and distribution in tissue is monitored (see Figure 2.8). This is achieved using repeat imaging of the feature of interest – commonly with a T1 weighted SGE sequence. When passing through microvasculature Gd diffuses into the extracellular-extravascular space (EES) and after extraction through the venous system, is cleared out by renal excretion. The analysis of the resulting local intensity variations as a function of time provides information on the amount of Gd reaching specific regions, which reflects tissue perfusion. Examples of DCE-MRI time

intensity-curves are shown in Figure 2.9. In addition the timing of such changes (e.g. fast contrast agent arrival and slow washout) provides further knowledge on the local tissue vascular properties.

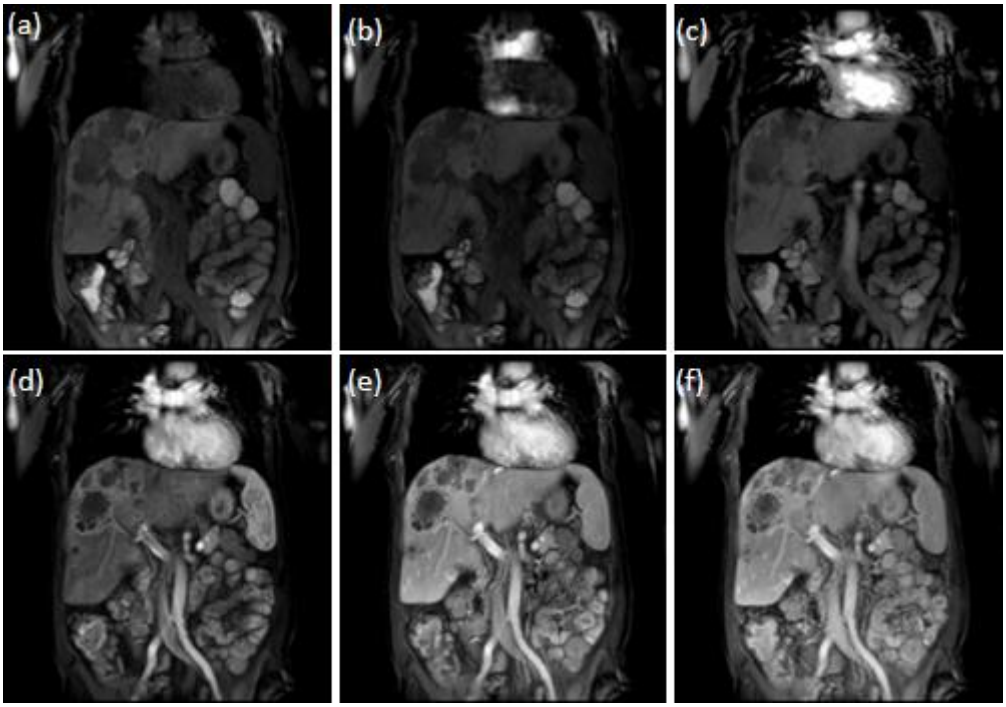

Figure 2.8: Examples of DCE-MRI data of a patient with liver cancer, acquired in the coronal plane. (a) pre-contrast frame, (b) (c) (d) bolus arrival and contrast agent uptake, (e) (f) post contrast washout phase.

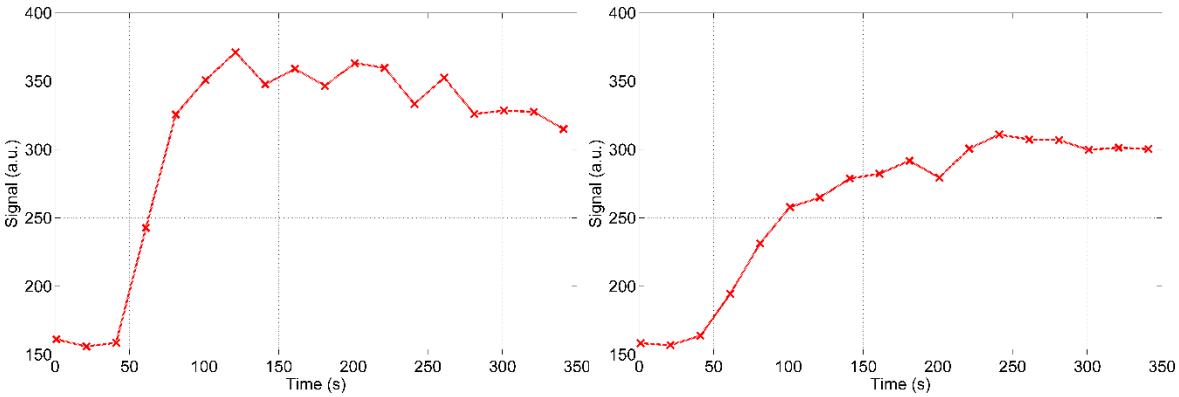

Figure 2.9: Examples of time intensity curves obtained in DCE-MRI. The shape of the enhancement profiles show differences in the contrast agent uptake and washout reflecting the local tissue properties. Additional fluctuations are related to noise and/or motion during acquisition (see section 2.6)

2.4.2 Data analysis

2.4.2.1 Modelling

Extracting the physiologic characteristics of relevant tissue from DCE-MRI can be done through pharmacokinetic modelling. Models developed in the early 90s have become a standard in many applications. The Tofts model [8] (mathematically equivalent to the Kety model [9]) describes the transfer of contrast agents between the capillaries and the EES. The flow of tracer from blood plasma into the EES is governed by equation (2.8), where K^{Trans} is the transendothelial transfer coefficient related to tissue permeability (and perfusion depending on the tissue vascularisation [10]), and v_e is the volume fraction of EES where the contrast agent has diffused. C_t is the contrast agent concentration in tissue. The arterial plasma concentration C_p is also called the arterial input function (AIF).

$$\frac{dC_t}{dt} = K^{Trans}\left(C_p - \frac{C_t}{v_e}\right) \tag{2.8}$$

The extended Tofts model [11] includes an additional compartment accounting for the contribution of Gd in the blood plasma to the total tissue concentration. This provides the expression of C_t given in equation (2.9):

$$\begin{aligned} C_t(t) &= v_p C_p(t) + K^{Trans}\int_0^t C_p(t) e^{\frac{-K^{Trans}}{v_e}(t-\tau)} d\tau \\ C_t(t) &= v_p C_p(t) + K^{Trans} C_p(t) \otimes e^{\frac{-K^{Trans}}{v_e}t} \end{aligned} \tag{2.9}$$

where v_p is the fractional volume of plasma in tissue – often small compared to v_e – which is related to perfusion. This two-compartment model is summarized in Figure 2.10.

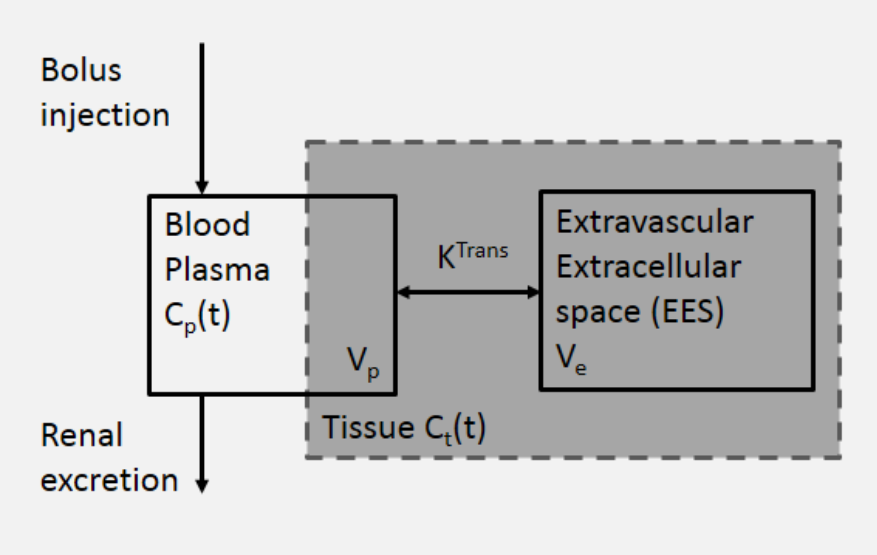

Figure 2.10: Schematic representation of the extended Tofts model

Other models developed by Larsson [12] or Brix [13] apply in a similar way to the description of MRI signal enhancement as a function of time. A review aiming at standardizing the quantities and parameters involved in these various models has been published [14]. More elaborate models have also been proposed [15]. However data analysis based on complex models is often difficult due to acquisition related limitations (see section 2.6).

2.4.2.2 Deriving tissue concentration

The complete analysis of the contrast enhancement profile from a single voxel or a region of interest requires several steps. First, intensity changes in image data must be converted to contrast agent concentration (this can be done before or with the model fitting). As fast gradient echo sequences are commonly used for DCE-MRI acquisition, equation (2.3) can be used to retrieve changes in T1 if the proton density S_0 is known. Then tissue concentration can be derived from equation (2.10) provided that tissue baseline T1, $T1_0$ is available. A value fixed of the Gd relaxivity r_1 (measured in vitro) is often used.

$$\frac{1}{T_1(t)} = \frac{1}{T_{10}} + r_1 C_t(t) \qquad (2.10)$$

$$r_1 = 4.5\ s^{-1}mM^{-1}$$

S_0 and $T1_0$ can be estimated, for example using multiple flip angle acquisition [16]. This technique uses repeat rapid T1-weighted GE imaging with varying RF pulse flip angles. The evolution of tissue signal with respect to the flip angle value describes a curve characterized by their T1 and proton density (see Figure 2.11). Fitting equation (2.3) to such curves allows the derivation of a $T1_0$ map. Tissue T1 measurement is also possible through other techniques (e.g. Look-Locker [17], modified Look-Locker inversion recovery [18]).

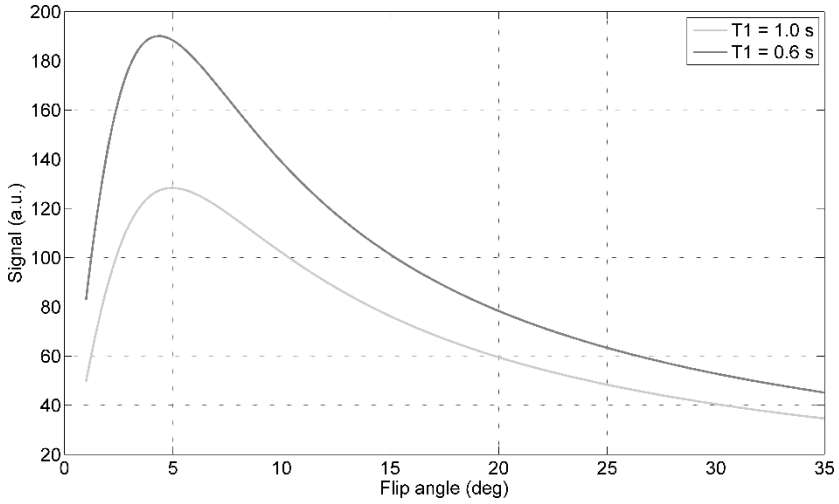

Figure 2.11: Signal evolution with respect to flip angle value for T1 = 0.6s and T1 = 1s. In both cases S_0 and TR were set to 1000 and 1.5ms respectively.

2.4.2.3 Estimating the arterial input function

Secondly, the AIF must be estimated. A number of methods have been developed to this end (see section 6.2); it may be estimated at a global level directly from a population specific function or via local fitting of an expected shape to a purely vascular region of interest. Alternatively the fitting of a given model to the tissue time concentration curves can be carried out, as shown in Figure 2.12.

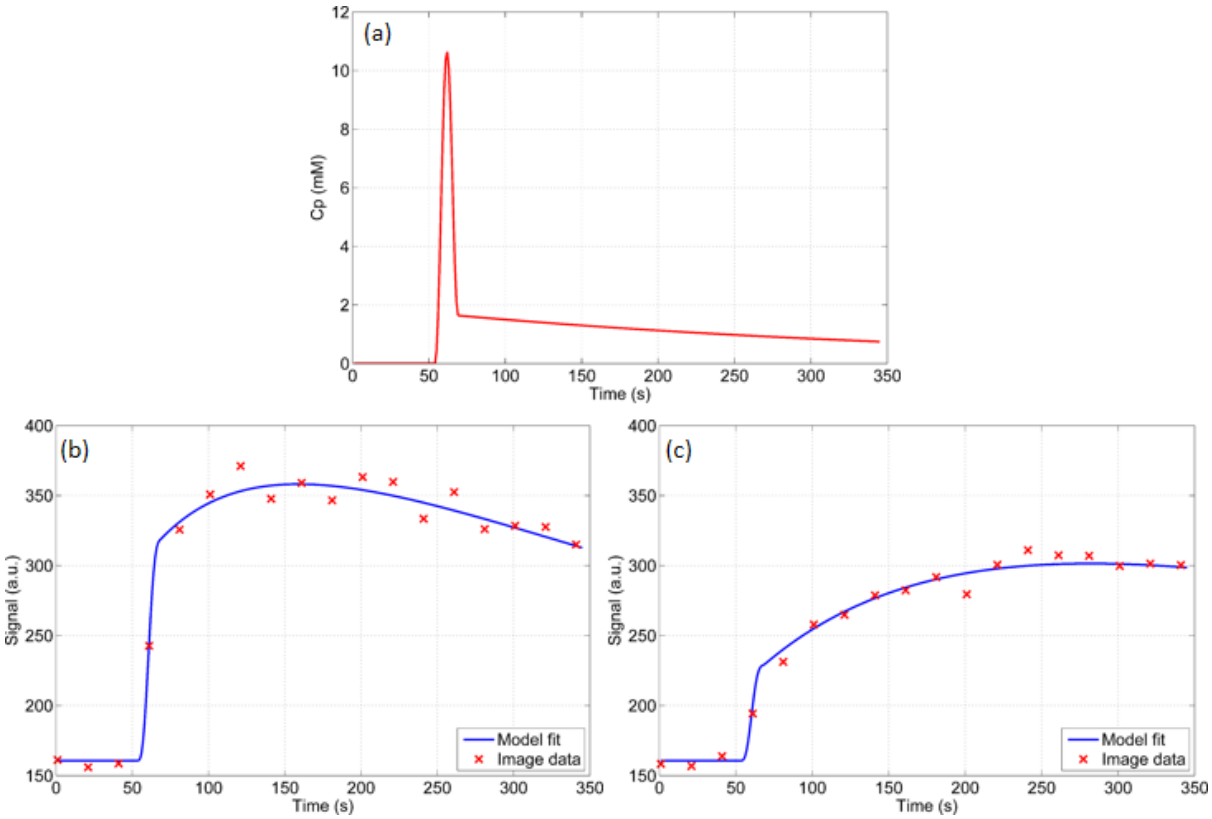

Figure 2.12: Example AIF model (a) and Tofts model fitting for the time intensity curves from Figure 2.9 (b) (c). The estimated pharmacokinetic parameters for both curves are: (b) K^{trans} = 0.37, V_e = 49%, V_p = 0.1%, and (c) K^{trans} = 0.13, V_e = 47%, V_p = 0%. Here the concentrations have been converted back to signal intensities after the fitting.

2.4.2.4 Pseudo-quantitative analysis

At a more simple level, some semi-quantitative parameters can be extracted directly from tissue enhancement curves (Figure 2.13): bolus arrival time, T_b; time to peak, T_p; area under the curve over a period of 60 or 90 seconds after the uptake, $AUC_{60/90;}$ and the peak height, H_p. Although they provide a description of the tissue enhancement profile independent of AIF, such parameters lack the clear link to a physiological meaning that the Tofts model provides.

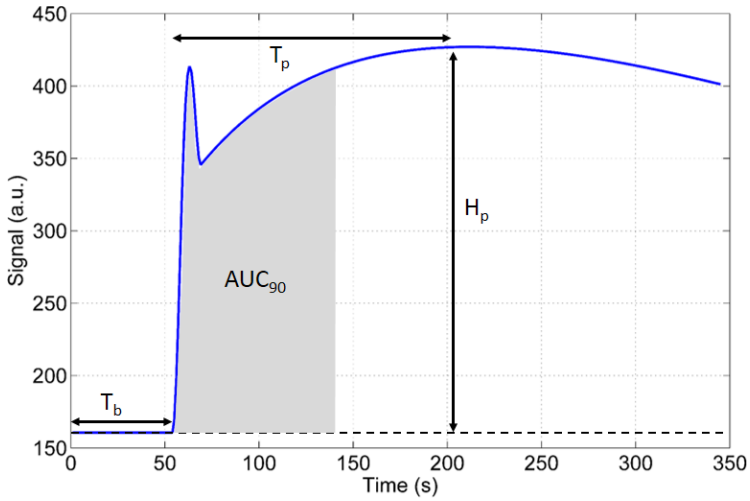

Figure 2.13: Pseudo-quantitative parameters in DCE-MRI analysis: bolus arrival time, T_b; time to peak, T_p; area under the curve, $AUC_{90;}$ and the peak height, H_p. Here AUC_{90} and H_p are given in terms of signal intensity but could similarly be calculated in terms of tissue concentration.

2.4.3 Applications

Quantifying tissue vasculature plays an important role in oncology. Thus the main application of DCE-MRI is the assessment of tumour growth and aggressiveness [10], [19]–[21]. The development of tumours triggers (pathological) angiogenesis – creation of blood vessels – to provide nutrients to cancer tissue. However, the rapid growing of the new vessels differs from normal angiogenesis. This causes the tumour capillary network to be highly disorganized with varying blood flow and abnormally permeable tortuous vessels. As a result, in DCE-MRI cancer regions demonstrate rapid, intense enhancement followed by rapid washout compared to normal tissue [20]. A number of treatments are aimed at stopping a tumour's blood supply (e.g. antivascular and antiangiogenic therapies). Due to its sensitivity to perfusion, DCE-MRI represents a useful, non-invasive tool to assess the effect of such therapies [21]. Other applications of DCE-MRI include the assessment of renal (except in case of renal insufficiency) and myocardial function [22], as well as liver [23] and intestinal diseases [24] diagnosis.

2.4.4 Other techniques

This section focuses on DCE-MRI but there are other MRI based techniques allowing perfusion imaging. Dynamic susceptibility contrast (DSC-) MRI relies on the T2 (and $T2^*$) decrease caused by the passage of Gd in tissue. The analysis of the DSC-MRI time series has similarities with that of DCE-MRI. However, DSC-MRI, often used in brain imaging, requires a single compartment model due to the blood brain barrier preventing the contrast agent from leaking into the EES. This also causes the shape of time-concentration curves to be different with very quick washout compared to DCE-MRI. Quantitative parameters are typically extracted from such curves using gamma-variate function fitting [1]. DSC-MRI is commonly used to quantify cerebral perfusion [25]–[27] and is usually acquired using gradient-echo EPI [28].

Arterial spin labelling (ASL) is another technique based on magnetically labelling the protons in the arterial blood supply flowing into the imaged slice [1]. The labelling consists of applying an RF pulse prior to image acquisition. Spins in the flowing blood are in a different magnetic state compared to that of surrounding static tissue and thus alter the local net magnetization. This results in a perfusion weighting of the output signal. ASL has the advantage of being fully non-invasive since no contrast agent injection is required and is often acquired using EPI. However, this technique is limited by low signal-to-noise ratio and by the delay between spin labelling and image acquisition which is required to give time for the blood to reach the region of interest. This delay causes a reduction of the label magnitude resulting in a reduction of the perfusion weighting [29]. The main application of ASL is the measurement of cerebral blood flow [29]–[31], often for research purposes.

2.5 Dynamic MRI for motion quantification

2.5.1 Principle

Similarly to DCE-MRI, dynamic MRI with high temporal resolution can be used to monitor mechanisms associated with rapid local motion or deformation of specific anatomical features. Moving organs (e.g. heart, gastrointestinal system) have a function associated with their motion (e.g. blood propagation, food processing and chyme propagation). Thus measuring such motion can provide useful information on these organs' physiological state.

An emerging type of dynamic MRI measurement applies to small bowel motility [32]. Motion in the bowel can be represented as the association of complex mechanisms including slow waves along the gastro intestinal tract, referred to as peristalsis, and radial contractions [33], [34]. After ingestion of Mannitol in oral solution, used for contrast, repeat imaging using a balanced Steady State Free Precession sequence (see section 2.2.3.3) may be carried out.

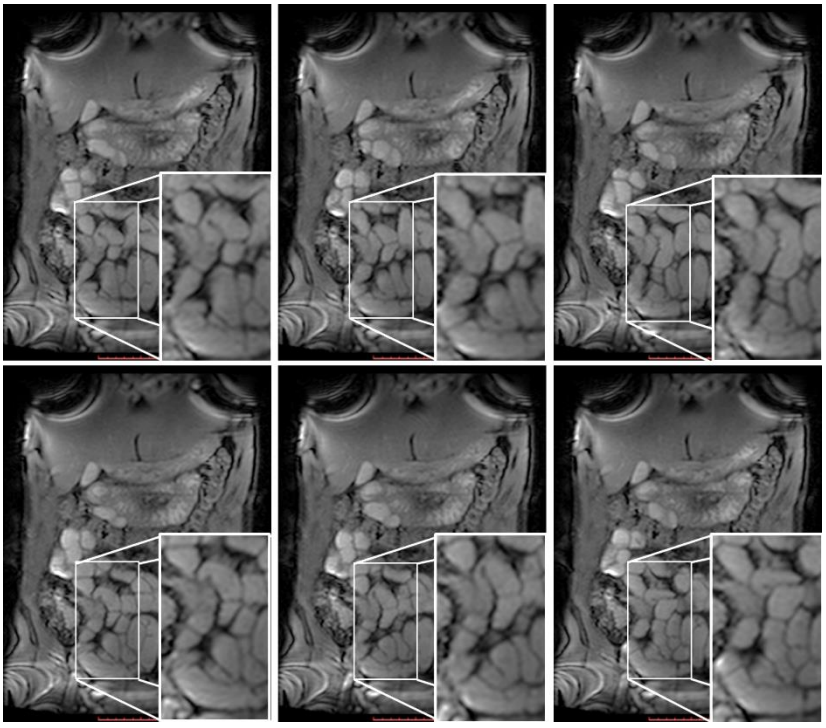

Figure 2.14: Example of Dynamic MRI of the small bowel in a healthy subject. In each time point a zoom on a small bowel region is shown to highlight bowel displacements related to peristalsis over time.

The resulting image time-series makes possible the identification of peristaltic abnormalities [35].

2.5.2 Data Analysis

Motility in a particular section of the bowel can be assessed by visual inspection [34]–[36]. Alternatively, a line region of interest (ROI) can be drawn in the bowel cross-section and manually propagated through all time points. The variation in the ROI length with time provides information on the amplitude and rate of the contractions. Alternatively automated methods based on image registration have been investigated [34], [36], [37].

Registration is the process of aligning the anatomical features from two different images: the target and source image [38]. It consists of computing a displacement vector for all pixels in the source image to make it match the target. Such a displacement field can be constrained to produce rigid, affine, or non-rigid transformation. Registration is particularly useful for motion correction, estimation of structural changes or differences, and fusion of data from different imaging modalities [38]. More details are given in section 4.2.1 .

In order to assess small bowel motility, non-rigid registration can be used to re-align the bowel wall in all the frames of the acquired time series. The computed bowel deformation through time can be measured (e.g. using the Jacobian determinant magnitude, see section 5.2.2) to quantify local and global motility [34]. Note that in this context, local motion is the mechanism of interest, which is modelled using the registration deformation field.

2.5.3 Applications

Several diseases affect small bowel motility, these include: dyspepsia, irritable bowel syndrome, Crohn's disease, intestinal pseudo obstruction and bacterial growth [34]–[36]. Dynamic MRI can be useful for the investigation of all these examples.

2.6 Challenges in Quantitative MRI

Extracting information from quantitative MRI comes with a number of challenges related to both data acquisition and analysis. Some of these concern MR imaging in general, while others are more specific to quantitative imaging. This section focuses on the second category.

2.6.1 Temporal Resolution

Quantitative measurements require the acquisition of a set of images, either to monitor a phenomenon or analyse the changes caused by a varying parameter. In DCE-MRI rapid contrast changes due to the uptake of contrast agent in tissue occur within seconds. Likewise, the period of the small bowel radial contractions can be as short as a few seconds. These effects necessitate a temporal resolution (i.e. time per frame acquisition) as high as possible to avoid sub-sampling of the mechanism of interest. Figure 2.15 illustrates the effect in the example of DCE-MRI: if the temporal resolution is too low, essential features of the enhancement profile might be missed. This can be particularly critical for example for the estimation of the AIF [15].

The main limitation of MRI in terms of temporal resolution, is the trade-off between temporal and spatial resolution. High dynamic temporal resolution can be achieved but this necessitates lower spatial resolution either in plane or in terms of slice thickness. In such case anatomical features might not be well defined which can hinder the identification and analysis of diseased tissue. Alternatively, more complex reconstruction techniques such as parallel imaging (see section 2.2.3.2) or compressed sensing [39] can speed up the acquisition of time frames. Compressed sensing techniques take advantage of sparsity from a limited number of random incoherent measurements to recover the signal using non-linear optimization. Undersampling results in an inherent loss of data and care must be taken to find a compromise between speed and image quality.

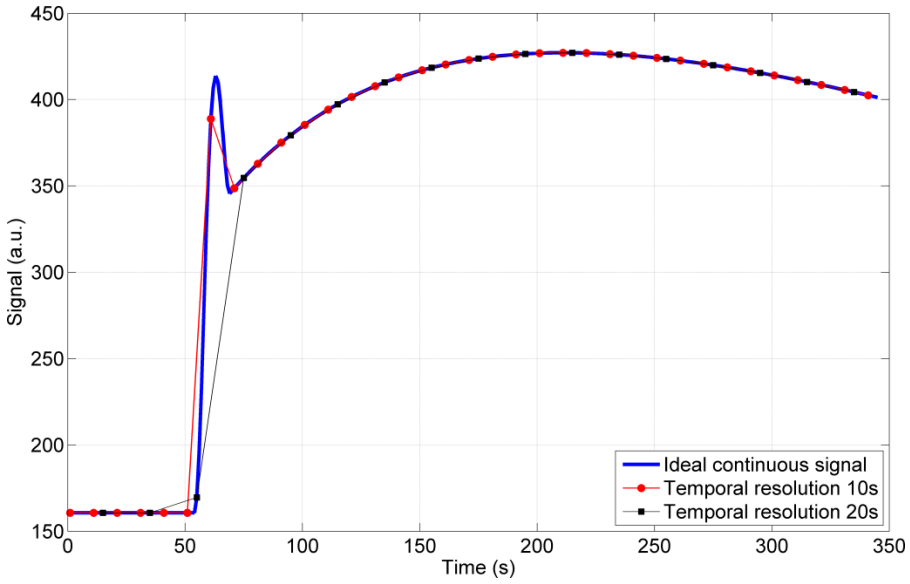

Figure 2.15: Effect of temporal resolution in the example of DCE-MRI. When sampled every 10 second the resulting signal still shows the peak in the uptake. However for a temporal resolution of 20 seconds the peak is missing from the signal which will bias the pharmacokinetic parameters estimate.

2.6.2 Motion

The problem is further complicated by subject motion (e.g. breathing) occurring during the acquisition. Importantly, respiratory motion can cause ghosting and blurring artefacts in each individual frame [40] and inter frame misalignments are likely to appear. These misalignments can have a dramatic impact on the data analysis because changes will then be related to both motion and the monitored effect, leading to a bias in the estimated quantitative parameters (see Figure 2.16, a). The use of breath-holds allows the reduction of intra-frame blurring, particularly likely to deteriorate the MR data when organs near the diaphragm are imaged using a free-breathing protocol [41]. Since patients cannot hold their breath for much longer than 20 seconds, repeat breath-holds may be performed to increase the imaging time period. In some cases irregular measurements can be taken by synchronizing acquisition with breath-holds period (see Figure 2.16, b). However, misalignments may occur due to the poor reproducibility between successive breath-holds.

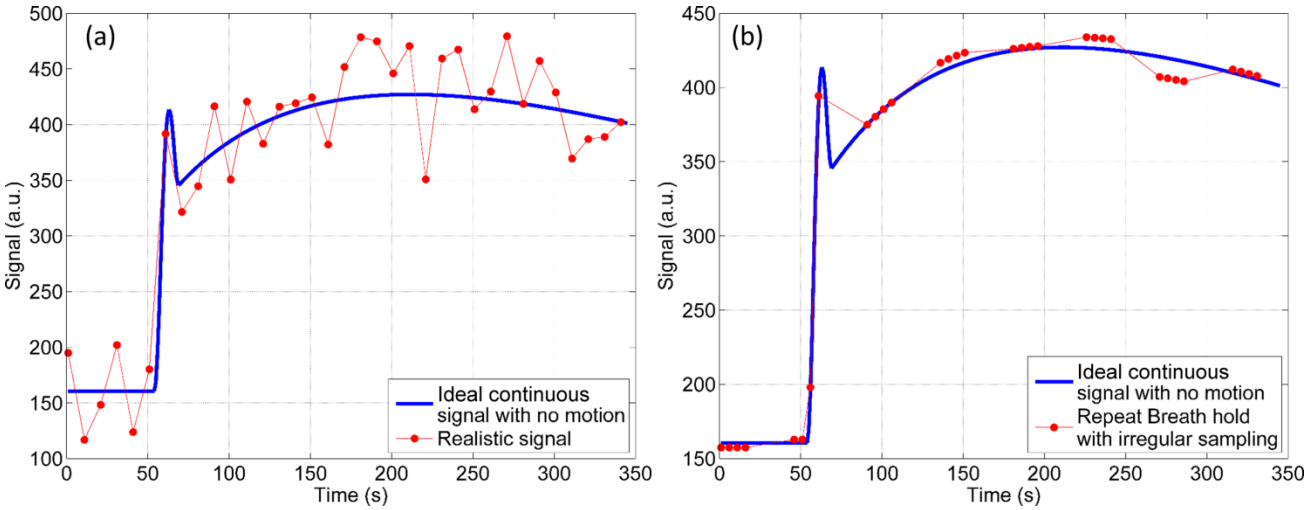

Figure 2.16: Effect of Motion in the example of DCE-MRI in the case of free breathing (a) and multiple breath-hold (b) acquisition. In both cases misalignments due to respiratory motion can bias the pharmacokinetic parameters estimates.

Such effect is not limited to dynamic imaging. Motion can affect DWI causing misalignments between measurements in different directions for the same b-values and between images at different b-values. It can also affect the estimation of tissue T1 when using the techniques mentioned in section 2.4.2.2.

2.6.3 Noise

Although noise is a well-known issue in qualitative imaging (not only MRI), it has a different impact in the case of quantitative imaging as it can bias the parameters estimated from the data. Similarly to motion, pixel intensity variation caused by noise can mislead a modelling processes. This is particularly important in the case of poor signal to noise ratio (SNR). As the name suggests the SNR is defined by the meaningful information divided by noise. In MRI this is often approximated by pixel intensities (within a ROI) divided by the standard deviation of the noise distribution.

2.6.4 Modelling

Extracting quantitative physiological information from MRI requires a wisely chosen model. If not adapted to the data the modelling process may result in an incorrect interpretation

that does not reflect the actual tissue properties. This could be the case, for example, in DWI: the bi-exponential model produces reliable estimates if the data have been acquired using at least 10 different b-values [42]. For a limited number of b-values (e.g. 3 or 4) the mono-exponential model should be preferred to the bi-exponential in order to obtain a meaningful estimate of the ADC. Another example applies to DCE-MRI of the liver where blood supply comes from two different sources: the hepatic artery and the portal vein. Thus, accurate pharmacokinetic modelling in the liver should use two independent AIFs to get reliable estimates of the hepatic tissue properties [43]. Also, the choice of the model in DCE-MRI should be based on the expected tissue vascularisation [10].

2.7 Conclusion

This first chapter has described the context of the studies carried out during this PhD and introduced key challenges related to quantitative MRI analysis. The following chapters will discuss some of these challenges in more detail and the proposed solutions.

For all clinical data presented in this thesis, a local ethics committee approved the retrospective use of anonymised patient data. For prospective data, all patients and healthy volunteers provided written informed consent as part of a protocol agreed by the local ethics committee.

3 Noise Modelling and Correction in DW-MRI

3.1 Introduction

In this chapter we present a number of approaches for noise modelling in the estimation of quantitative parameters from clinical diffusion weighted imaging (e.g. Apparent Diffusion Coefficient). The objective is to investigate the potential benefit of applying recent modelling techniques to routine clinical scans.

DWI provides useful quantitative information on tissue microstructure but has inherently low SNR because of the diffusion weighting gradients (see section 2.3.1). Due to the non-normal distribution of magnitude DWI data, commonly used techniques for model fitting (e.g. least squares) yield biased parameter estimates. The first part of this chapter consists of a description of the noise distributions that are expected to appear in DW images depending on the hardware and the choice of reconstruction scheme. In the following sections, we present the different estimation methods and, separately for each, the application to both simulated and clinical data. These techniques are presented in logical order (see Figure 3.1) starting with simple assumptions on the data acquisition, and gradually accounting for more complex imaging schemes. Comparison and analysis of the estimated parameters obtained with each method are used to assess the importance of taking into account and correcting for noise in routine clinical imaging. We applied some of the described methods to prostate cancer, which is the most common cancer in the male population [44]. DW-MRI is routinely used in combination with T2-weighted MRI and DCE-MRI to localise prostate cancer [45], [46]. Moreover, ADC thresholds have been proposed for tumour detection [47] and negatively correlated with Gleason grade in peripheral zone prostate cancer [48]. The application of DWI to head and neck cancer is also of interest and was addressed in the last part of the study [49], [50].

The work presented in this chapter focuses on the mono-exponential model (introduced in section 2.3.2.1). In chronological order, this work started with translational application of the pre-clinical work published in [51] leading to conference publications at MIUA 2011 [52],

RSNA 2011 [53] and ISMRM 2012 [54]. However, accounting for changes due to parallel acquisition and averaging in clinical data led to more sophisticated methods and a journal publication by Dikaios et al. [55] to which the author contributed. Contributions included investigation on the nature of noise in parallel imaging with multiple averaging and modelling of the noise distributions along with the generation of simulated data.

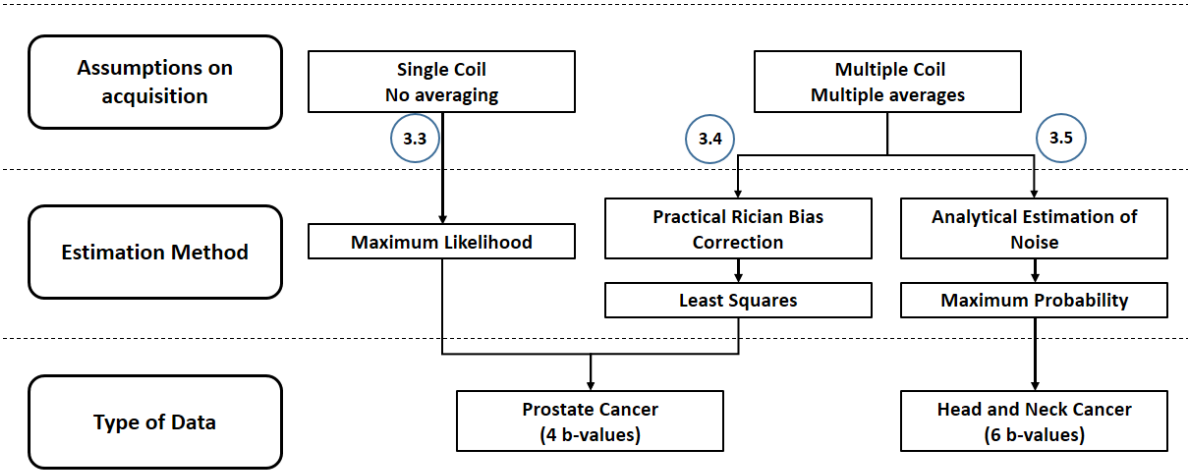

Figure 3.1: Flow chart outlining the content of the chapter. Different assumptions on the acquisition scheme estimation methods are considered. Blue circles indicate the sub-section in which each approach is described.

3.2 Noise in Magnitude DW-MRI

Noise due to thermal agitation follows a Gaussian distribution in the signal acquired in the K-space. However, depending on the choices of acquisition settings, hardware and data reconstruction strategy, the noise distribution in DW-MR images can vary. The following section details some of the situations that can be encountered.

3.2.1 Rician distribution

DW-MR images are created from signals obtained when applying diffusion gradients in the three or more directions of space. Magnitude data M are derived from the modulus of the real, Re and imaginary, Im parts of the complex MR signal:

$$\mathrm{M} = \sqrt{\mathrm{Re}^2 + \mathrm{Im}^2} \tag{3.1}$$

Thermal agitation causes normally distributed noise in both of these components which leads to Rice distributed data in DW-MRI [56] modelled by the following probability density function (PDF):

$$p(M|S,\sigma_R) = \frac{M}{\sigma_R^2}\exp\left(-\frac{M^2+S^2}{2\sigma_R^2}\right)I_0\left(\frac{MS}{\sigma_R^2}\right) \quad (3.2)$$

where M is the observed noisy magnitude MR signal, S is the true magnitude, σ_R is the Rician noise parameter, corresponding to the standard deviation of the underlying Gaussian distribution, and I_0 is the 0^{th} order modified Bessel function of the first kind. In particular, the Rician PDF matches the Rayleigh distribution in the absence of signal (i.e. in the image background) and gets closer to a Gaussian at high SNR [57].

3.2.2 Multiple receiver coils

The Rician model described in the previous paragraph is always valid in the case of magnitude data obtained from a single receiver coil, with a single source of complex signal. However, the nature of noise can be altered by the use of parallel imaging with multiple receiver coils. Depending on the imaging and/or reconstruction method chosen, noise may not be Rice distributed in the output data.

Dietrich et al. described the type of noise distributions that should be expected in a number of cases [58]. This is summarized in Table 3.1. Data reconstruction from multiple channels can be computed using the root sum of squares (SOS) method or alternatively using the spatial matched filter (SMF) that maximizes the SNR. SMF consists of using the coils sensitivity at each pixel as a weighting factor for the linear combination of signals from the different channels [59]. Accelerated acquisition using parallel imaging is based on under-sampled data coming from different receivers and the incorporation of coil sensitivity profiles in the reconstruction process. It can be based on the frequency domain as in the Generalized Auto-calibrated Partially Parallel Acquisition (GRAPPA) [3] or on the image domain as in Sensitivity Encoded MRI (SENSE) [4]. Depending on the choice of the

aforementioned techniques and the associated reconstruction strategy, magnitude data can be corrupted with noise following non-central χ or Rice distributions.

Acquisition/ Reconstruction	Noise Distribution
Multi coil, SOS	non-central χ
Multi coil, SMF	Rice
Multi coil GRAPPA, SOS	non-central χ
Multi coil GRAPPA, SMF	Rice
Multi coil SENSE	Rice

Table 3.1: Summary of the expected noise distributions depending for different acquisition schemes [59]

In addition, accelerated acquisition with GRAPPA or SENSE involves data reconstruction from under-sampled images weighted by the coils sensitivity maps which leads to non-stationary noise [60].

3.2.3 Signal to noise ratio and the effect of averaging

As introduced in section 2.3.1, higher diffusion weighting gradients lead to a lower observed signal while thermal agitation remains the same. Thus, the SNR in DW-MRI is significantly lower at higher b-values.

A common method to overcome the problem of low SNR in DW-MRI (other than reducing the image spatial resolution) is to run multiple measurements of the same physical slice and take the average. When complex data is averaged this increases the SNR by a factor equal to the square root of the number of measurements. The effect of averaging magnitude MR data on the noise distribution has been described by Kristoffersen et al. [61]. If the increase in SNR due to averaging is high enough, the Rice distribution approaches a Gaussian (as per the central limit theorem). However if the number of averages is too low to allow the Gaussian approximation the new PDF can be modelled by the convolution of the Rician PDFs of each measurement [55], [61].

One should also notice that although multiple averages make Rician distribution closer to a Gaussian distribution, such a Gaussian remains centred on the non-zero mean of the Rice PDF (see Figure 3.2).

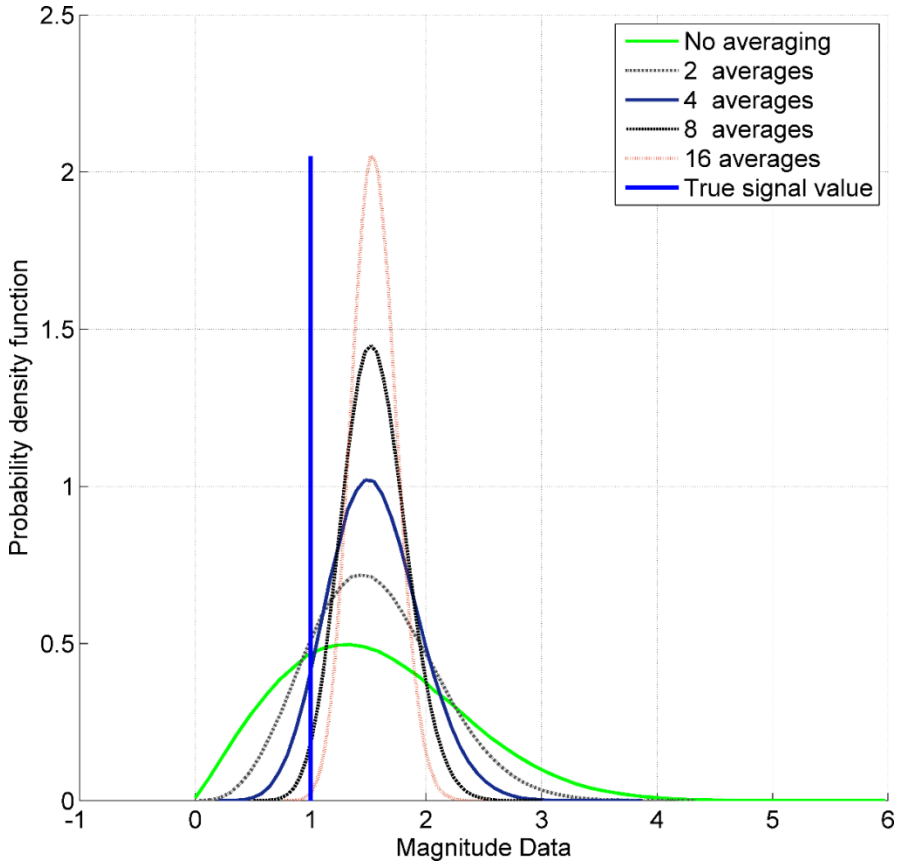

Figure 3.2: Illustration of the effect of averaging on the noise distribution (initial SNR = 1). The SNR increases with the number of measurements (as indicated by the narrower PDFs) and the data distribution gets closer to a Gaussian. However the bias caused by Rician noise is not reduced

3.2.4 Challenge in Noise modelling

The derivation of ADC maps from diffusion weighted images can be done on a pixel-by-pixel basis or for a defined region of interest. It is usually performed using the least squares (LS) fitting method due to its speed and ease of implementation. However such an algorithm makes an incorrect assumption on the type noise corrupting the data as it considers noise in the measured signal magnitude to be normally distributed. Therefore if the nature of the noise distribution is not carefully studied the LS fit of a given model to diffusion weighted data is likely to yield biased estimates (as illustrated in Figure 3.3).

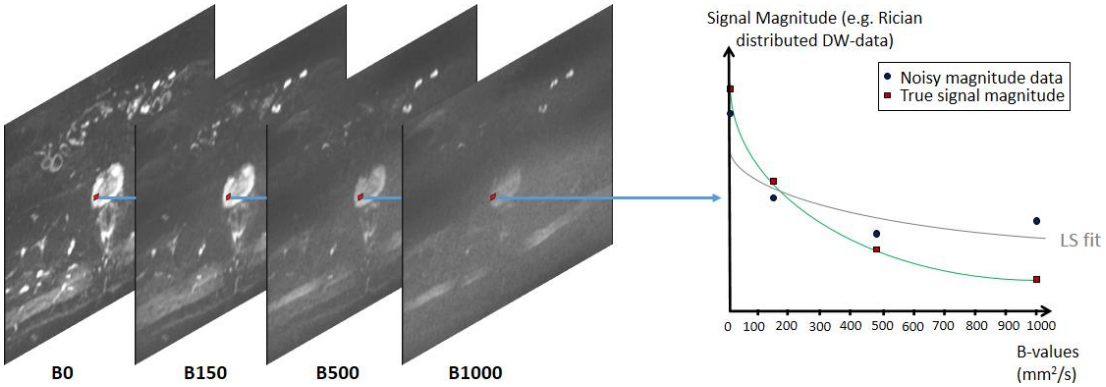

Figure 3.3: Schematic view of pixel-by-pixel ADC extraction using fitting of DW-MR data. At high b-values where the SNR is poor, the presence of noise increases the signal intensity which can result in the underestimation of ADC when using a simple LS estimation scheme

LS estimation consists of approximating the ADC by minimizing the sum of squared differences between the observed noisy magnitude MR signal M and one of the models S given in (2.5), (2.6) or (2.7) as presented in section 2.3.2.

$$L_{LS}(ADC, S_0; M) = \sum_{i=1}^{N} (M_i - S(b_i))^2 \tag{3.3}$$

Several studies aiming at providing accurate noise estimation [41], [60], [62]–[66] and reducing the estimation bias [51], [55], [60], [61], [67], [68] have been conducted. In the following section we describe in more details some of the methods that have been proposed to increase the robustness to noise and produce reliable ADC estimates.

3.3 **Maximum Likelihood estimation**

3.3.1 Theory

LS provides an accurate estimate only when the noise is Gaussian distributed. The first level of refinement to increase modelling robustness is to account for Rice distributed data, assuming uniform distribution. Sijbers et al. defined an approach using maximum likelihood (ML) to estimate MR signal intensity corrupted with Rician noise [66]. Following that work, Walker-Samuel et al. [51] applied the ML approach to mouse diffusion weighted MR data. Given the Rician PDF described in (3.2), the Likelihood function is defined as follows:

$$\mathrm{L}(\mathrm{ADC}, \mathrm{S}_0; \mathrm{M}, \sigma_\mathrm{R}) = \prod_{\mathrm{i}=1}^{\mathrm{N}} \mathrm{p}(\mathrm{M}_\mathrm{i}|\mathrm{S}_\mathrm{i}, \sigma_\mathrm{R}) \tag{3.4}$$

where N is number of B-values, and σ_R is the standard deviation of the Rayleigh distribution from a background region. Then by taking the negative logarithm of the Likelihood function:

$$\mathrm{Log}\big(\mathrm{L}(\mathrm{ADC}, \mathrm{S}_0; \mathrm{M}, \sigma_\mathrm{R})\big) = \sum_{\mathrm{i}=1}^{\mathrm{N}} \frac{\mathrm{S}(\mathrm{b}_\mathrm{i}|\mathrm{ADC}, \mathrm{S}_0)^2}{2\sigma_\mathrm{R}^2} - \sum_{\mathrm{i}=1}^{\mathrm{N}} \log\left(\mathrm{I}_0\left(\frac{\mathrm{S}(\mathrm{b}_\mathrm{i}|\mathrm{ADC}, \mathrm{S}_0)\mathrm{M}_\mathrm{i}}{2\sigma_\mathrm{R}^2}\right)\right) \tag{3.5}$$

This negative log-likelihood function can be minimized with respect to the ADC and S_0, yielding the most likely value of ADC given the data, and Rician noise model. Note that some terms independent of S have been omitted in (3.5).

3.3.1.1 Noise parameter estimation

The likelihood function given in (3.5) requires a prior estimate of the noise parameter σ_R. It can be estimated using a background (i.e. air) region of interest using fitting to Rayleigh distribution [51].

3.3.2 Data and Experiments

All the experiments described in this section were focused on the application of DWI to prostate cancer imaging. The increased cellularity in prostatic tumours causes a decrease of ADC compared to normal tissue due to the more restricted displacement of water molecules. Thus DWI imaging is of interest for prostate cancer characterization [45]. The following paragraphs present simulated and clinical datasets used to assess the performance of ML estimation.

3.3.2.1 Monte Carlo simulation

Monte Carlo simulation based on 1-D signals were first run to compare results obtained with ML and LS. A total of 10^4 fittings were run for each value of ADC in the range $[0.1 - 3] \times 10^{-3}$ ($\mathrm{mm}^2.\mathrm{s}^{-1}$) and for each SNR in the range $[1 - 15]$. Here the SNR is defined, similarly to [51], as the ratio of the magnitude signal divided by the noise standard

deviation. These values of SNR and ADC were chosen in order to cover the possible values encountered in prostate DW-MR at 1.5T [69]. The generated signals were sampled at the following b-values: $[0\ 150\ 500\ 1000]$ (s.mm^{-2}) for fitting. This is summarized in Figure 3.4.

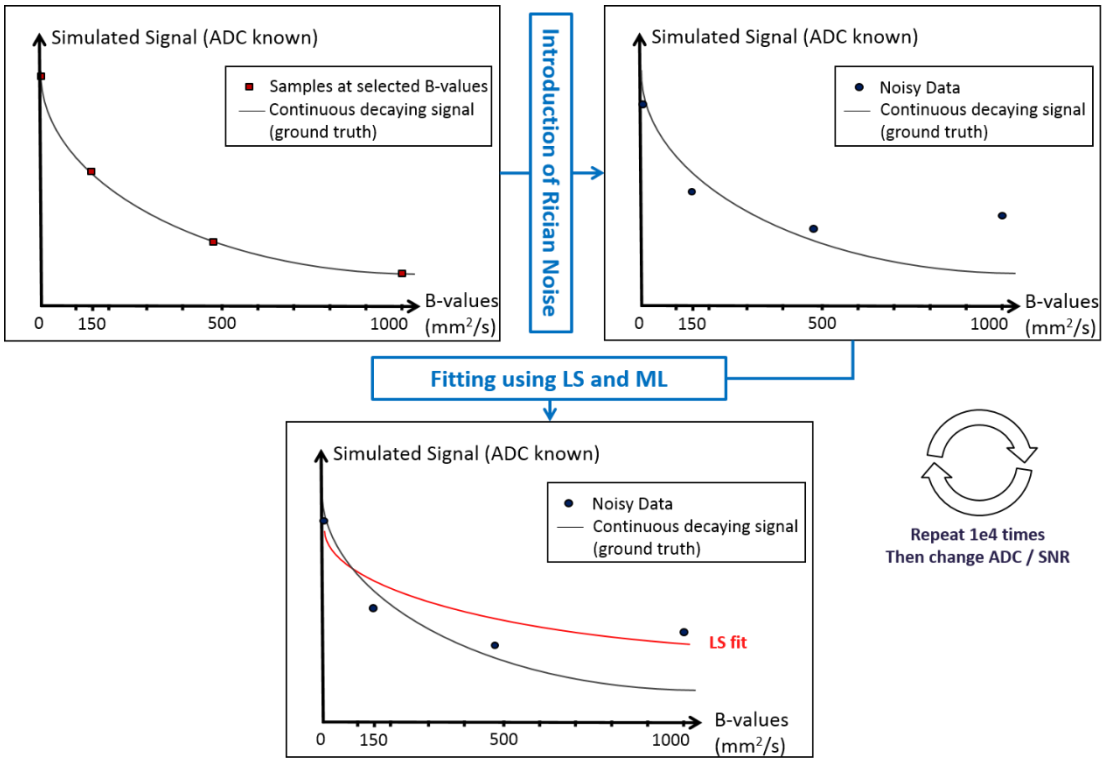

Figure 3.4: Flow chart of Monte Carlo simulation. The decaying signal is created based on a given value of ADC (top-left), then Rician noise is introduced based on a given value of SNR (top-right) and the two fitting methods are applied (bottom)

The objective of this experiment was to highlight statistical differences in accuracy between the LS and ML, as well as potential variation with respect to the ground truth values of ADC and SNR. These were evaluated by calculating the median absolute error and Inter-Quartile Range (IQR) of estimates for each couple (ADC, SNR).

3.3.2.2 Phantom based simulation

Further assessment of the two methods was achieved using 2-D phantom simulations performed to assess whether region of interest (ROI) based estimates of ADC, as are commonly used for radiological studies, differ significantly between ML and LS generated ADC images and from the “ground truth” ADC. Fields of view containing a tumour region

surrounded by prostate normal tissue were created. Varying size was used for the tumour (radii between 2.7 and 8.5 mm) to cover the typical size range observable in clinical data. Ground truth ADC values were chosen for tumour (1.02×10^{-3} mm^2.s^{-1} in the peripheral zone, 0.94×10^{-3} mm^2.s^{-1} in the transition zone) and normal tissue (1.8×10^{-3} mm^2.s^{-1} in the peripheral zone, 1.34×10^{-3} mm^2.s^{-1} in the transition zone) based on previous studies [69], [70]. For the selection of a SNR range a set of 18 individual patient prostate multi-parametric MRI studies was interrogated (see section 3.3.2.3). Signal intensities for pixels within each of simulated diffusion weighted image were then corrupted with Rician noise estimates derived from patients' data (see example Figure 3.5). A ground truth ADC image (non-noisy) was generated for each tumour size with a central circular tumour region surrounded by normal prostatic tissue (see Figure 3.6), and used as a reference for assessing the accuracy of ML and LS estimated ADC values. Diffusion weighted images corresponding to individual "ground truth" ADC images were generated at the following b-values: $[0\ 150\ 500\ 1000]$ (s.mm^{-2}). The initial signal intensity of simulated tumour and peripheral zone areas was set to a mean value estimated from the patient data. Finally, ML and LS algorithms were applied to generate separate ML and LS ADC images. Median ADC for the entire simulated tumour and a corresponding sized ROI placed within the simulated normal peripheral or transition zone was recorded from ML and LS generated ADC images. This process was repeated 10^3 times using randomly generated noise distributions applied at each SNR for each tumour size.

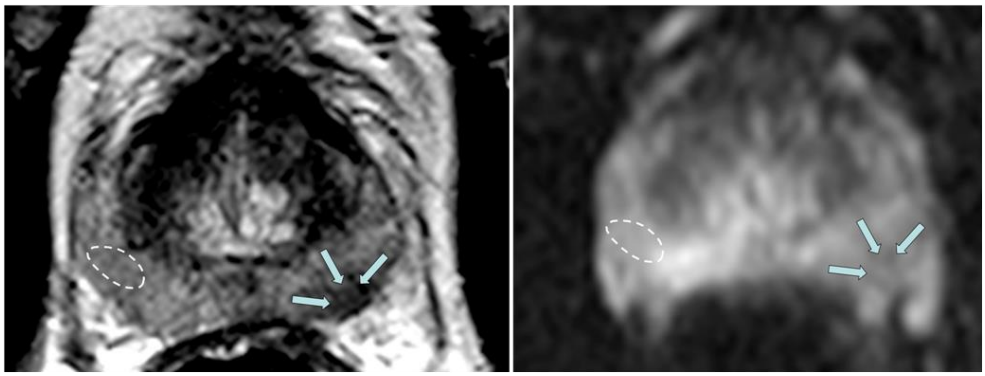

Figure 3.5: Example of patient prostate MR data with delineated regions of interest in T2-MR data (left), and b_0 image (right); the tumour and normal peripheral zone ROIs are indicated by the arrow heads and dotted lines respectively

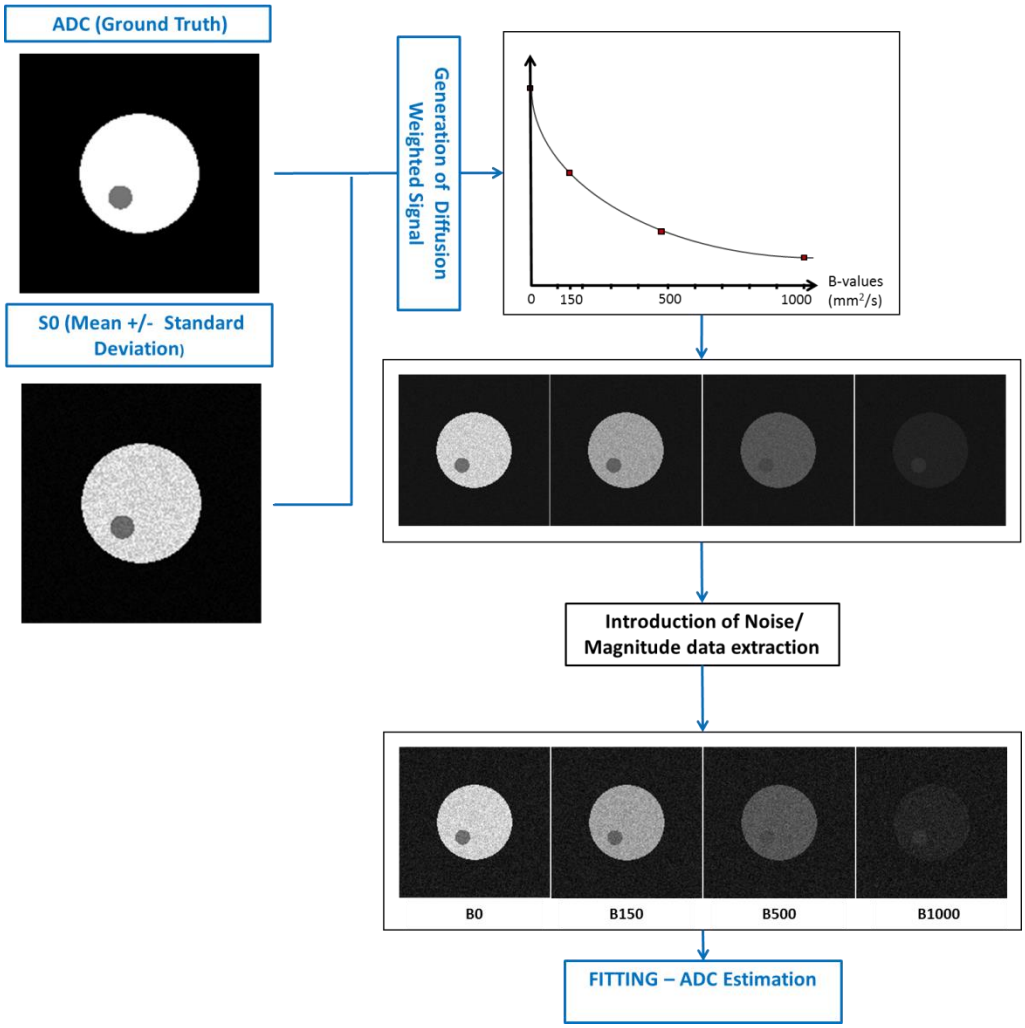

Figure 3.6: Example of creation of phantom data for tumour ROI of 150 mm^2 and Rician noise parameter $\sigma_R = 0.05$. DW signals are generated for each pixel from ground truth ADC and S0. Images are then derived at each selected B-value after addition of noise.

3.3.2.3 Clinical DWI

DW-MR prostate scans of 18 patients were used to compute tumour and normal prostate tissue ADC. For both types of tissue, ADC estimates were assessed as well contrast differences in parametric mapping derived from each method (i.e. LS, ML). Patient studies were retrospectively selected from a database of multi parametric MRI performed for detection of prostate cancer using a standardised imaging protocol of T2, diffusion and dynamic contrast enhanced imaging. The inclusion criterion was based on histopathology confirmation of the presence of cancer from prostatic template mapping biopsy [71]. Of the 18 patients included, nine had a tumour located in the peripheral zone and the other nine had tumour within the transition zone.

All multi-parametric MRI studies were all performed at 1.5T (Magnetom Avanto, Siemens, Erlangen, Germany) scanner using a standard phase array coil. DW-MR images were acquired using a spin echo EPI sequence with 16 averages, an image matrix 172x172 pixels, slice thickness of 5 mm over a field of view of 260x260 mm, with trace images generated at b-values of $[0\ 150\ 500\ 1000]$ (s.mm^{-2}). Further sequence details are presented in Table 3.2.

Sequence type	**Echo Planar (STIR-EPI)**
Repetition Time (ms)	2100
Echo Time (ms)	96
Slice Thickness (mm)	5
Image Matrix (pixel^2)	172x172
Field of View (mm^2)	260x260
Parallel Acquisition (iPAT)	GRAPPA with Adaptive Combine Reconstruction (SMF)
Number of averages	16
b-values (s/mm^2)	0;150;500;1000
Total Acquisition Time (min)	6

Table 3.2: Details of prostate DW-MRI acquisition sequence.

For each patient, the study radiologist aware of both the radiological report and the template-mapping biopsy histopathology report, located and matched tumour on MR

images with the reported histopathology site. Histologically confirmed areas of normal tissue were localised in the same manner. The radiologist carefully contoured a region of interest around the tumour on b_{500} diffusion weighted images. A second ROI was similarly contoured within normal prostatic tissue.

In the work presented in the current section, the imaged field of view was considered small enough to assume that noise non-stationary characteristic, due to parallel imaging, could be neglected.

The noise variance was estimated by manually selecting background regions in b_0 images from the same patients and fitting to a Rayleigh distribution to provide an estimate of Rician noise. The SNR range used for simulation ranged from the lowest SNR to the highest SNR recorded across patients.

3.3.2.3.1 Quantitative analysis

Diffusion weighted images of the slices containing the contoured tumour and normal ROIs were extracted for analysis. Median ADC estimates for pixels within cancer and for normal prostate tissue ROIs were computed using the LS and ML algorithms. Tumour to normal tissue contrast ratio was calculated for each patient for the different ADC estimates. Comparison with simulation data was achieved using tumour and normal tissue SNR estimated for each patient on the b_0 image as described in the previous paragraph.

3.3.2.3.2 Qualitative analysis

Two radiologists blinded for review, independently performed a subjective assessment of tumour obviousness in the two ADC maps for each of the 18 patients in a specifically developed Matlab® (The Mathworks, Natick, MA) graphical user interface. The imaging slice containing the tumour (as used for quantitative analysis) was cropped tight to the prostate in order to mask any potential differences in noise generated within areas of the image outside the body that may bias the radiologists. Each radiologist had access to the T2 weighted image (with tumour ROI indicated) corresponding to the ML and LS estimated ADC images being evaluate. Radiologists were presented matching pairs of unlabelled ML

and LS ADC images in a random order and asked to select the ADC image on which the tumour could be most clearly seen, or indicate if no difference was observable.

3.3.3 Results

3.3.3.1 Monte Carlo Simulation

Across the repeated simulations, the median percentage error of ML and LS ADC estimates (when compared against the “ground truth” ADC) was lower for pixels with higher SNR and for pixels with smaller ground truth ADC values (see Figure 3.7). ML estimates of ADC were closer to the ground truth ADC. In general, for a given “ground truth” ADC, median percentage error of ML ADC estimates was less than 10 % for SNRs greater than 2. For LS estimates the same accuracy was obtained for SNRs greater than 5.

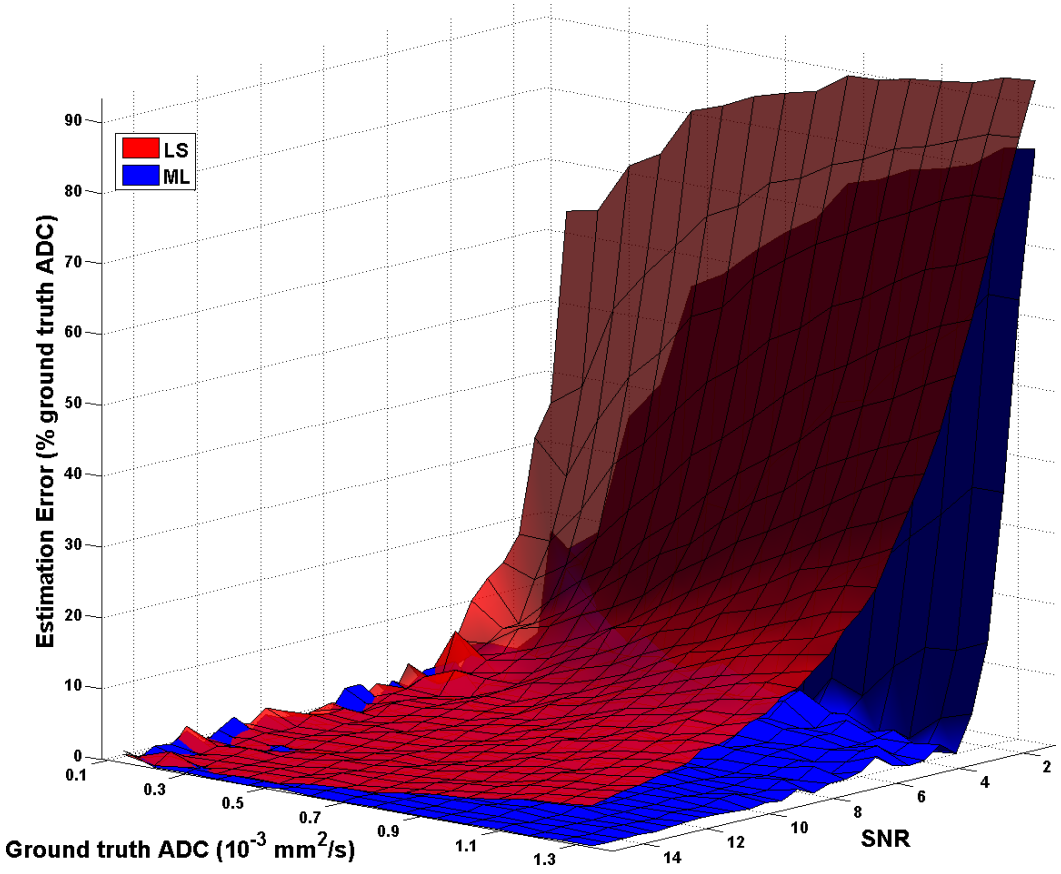

Figure 3.7: Monte Carlo simulations for ADC values from 0.1 to 3.1 10^{-3} mm^2/s and SNR values from 1 to 15. The graph shows 3D surfaces representing the median of absolute error of estimates compared to the ground truth ADC value, obtained with both LS (red) and ML (blue). Results are presented as a percentage of the ground truth ADC.

For SNR values typically observed in DW-MR of the prostate (4 ≤ SNR ≤ 15), median LS estimates consistently underestimated the ground truth ADC; with poorer estimation at lower SNR. Median ML estimates provided an accurate estimate of the ground truth ADC value and were less affected by SNR (see Figure 3.8). An increase of error can be observed with LS for higher value of ADC. This is due to the fact that for the same level of noise, a higher ADC causes lower signal at high b-values which can be interpreted as an indirect decrease of SNR.

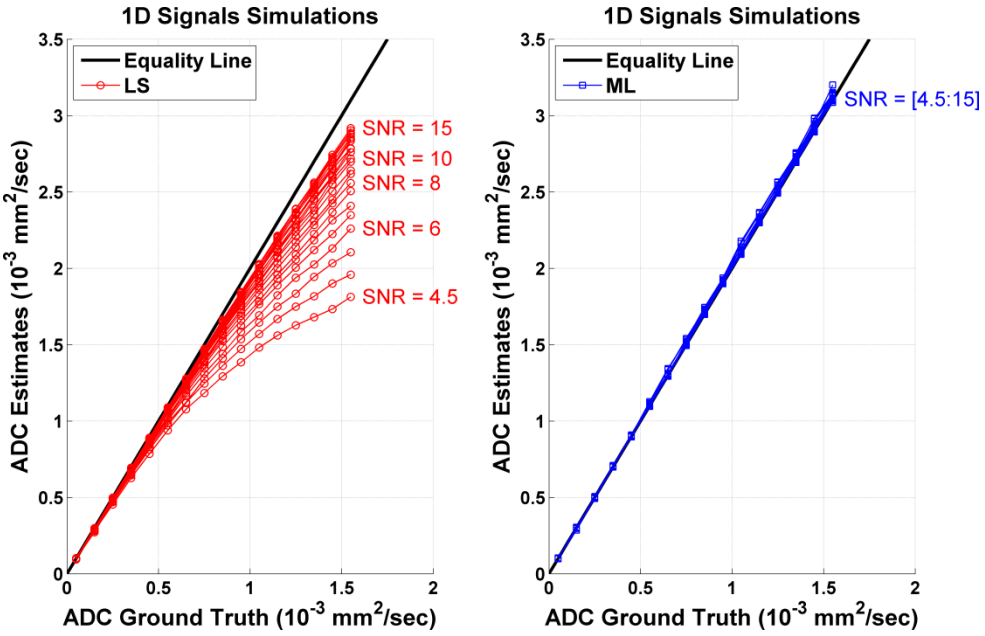

Figure 3.8: Representation of the LS (left) and the ML (right) estimates compared to ground truth ADC values for SNR = [4.5, 15]. ADC range covers values typically observed in tumour areas ([0.6, 1.2] 10^{-3} mm^2/s). The LS underestimation of ADC appears clearly, along with sensitivity to SNR variations. The ML estimates all lie very close to the line of equality: the lines corresponding to different SNRs are practically overlaid. This shows the greater robustness to SNR changes and better accuracy of ML.

However, for typical ground truth ADC for tumour (e.g. 0.9 x 10^{-3} mm^2/s) and normal peripheral zone tissue (e.g. 1.5 x 10^{-3} mm^2/s), the IQR of the repeated simulations was greatest for ML estimates. The IQR of ML estimates was also more greatly affected by reductions in SNR (see Figure 3.9).

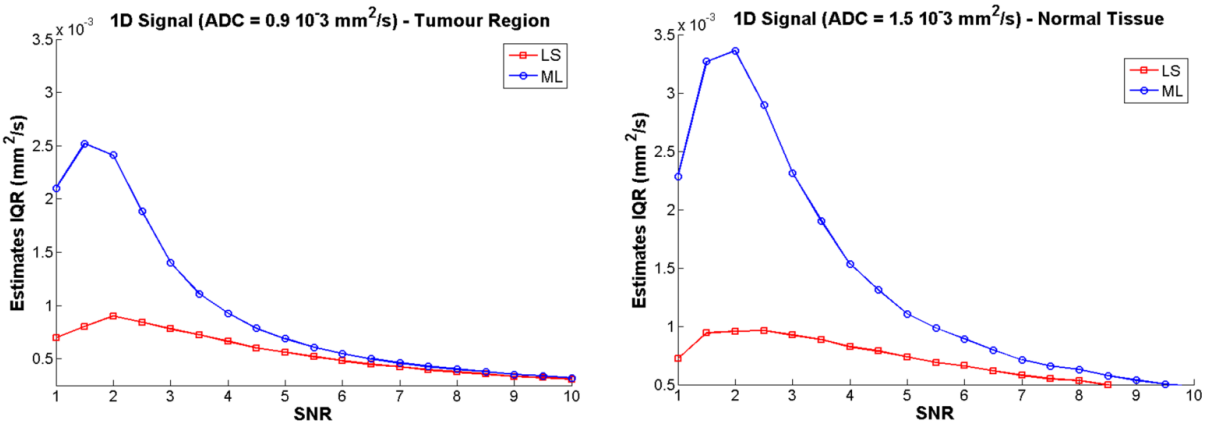

Figure 3.9: Monte Carlo simulations at ADC values of 9x10-4 mm^2/s (left) and 1.5x10-3 mm^2/s (right). These graphs show the inter-quartile ranges as a measure of deviation for the LS (red circles) and the ML (blue squares) obtained for various SNR values.

3.3.3.2 Phantom Simulations

Mean SNR in b_0 images across the 18 patients ranged from 5.11 ± 0.77 for transition zone tumour to 13.6 ± 5.42 for normal peripheral zone tissue (see Table 3.3). These results are based on noise measurements in the background region. The maximum and minimum SNR calculated was 10.45 and 3.78 for tumour, and 23.52 and 5.44 for normal tissue.

	Peripheral zone (PZ)	**Transition zone (TZ)**	**PZ vs. TZ SNR (p-value)**
Mean SNR Cancer ± SD	7.49 ± 2.27	5.11 ± 0.77	0.009 *
Mean SNR Normal ± SD	13.6 ± 5.42	7.46 ± 1.59	0.005 *
Cancer vs. Normal SNR (p-value)	0.002 *	<0.001 *	

Table 3.3: SNR values obtained in 18 patients for cancerous and normal tissue in either peripheral or transition zone based on background noise measurement. A significant difference (indicated by '*') could be observed between the two types of tissue in both areas.

The median percentage error and IQR for repeated estimates for the 1000 calculations of ADC performed at each of the increasing tumour and normal tissue ROI sizes is illustrated for both transition zone and peripheral zone using LS and ML algorithms in Figure 3.10. The median percentage error was consistently higher for LS (up to 9%) compared with ML (range of median error 0% to 3%) estimated ADC values for tumour and normal tissue for all ROI sizes greater than 10 pixels ($p < 0.001$). In addition, there was no statistical

difference between the IQRs obtain for all ROI sizes with LS and ML (p = 0.403). Across all ROI sizes ML were on average 8% lower for tumour and 11.1% lower for normal peripheral zone than LS ADC estimates.

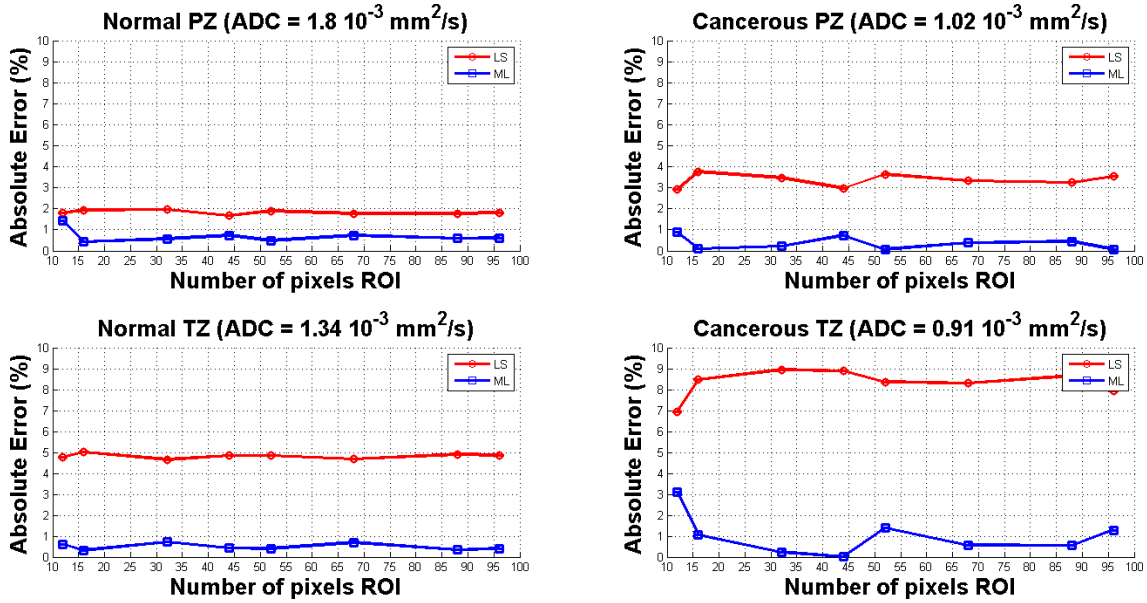

Figure 3.10: Result estimates of phantom experiment. The graph show the median (over the 1000 simulations) of the median estimates for pixels in the normal tissue (left) and tumour ROIs (right) in peripheral zone (top) and transition zone (bottom) obtained with both LS (red) and ML (blue). In all tissue types the ML consistently reduces the estimation error.

3.3.3.3 Clinical Data

Median LS and ML estimates of ADC for normal peripheral and transition zone, and peripheral and transition zone tumour is given in Table 3.4. ML ADC estimates for normal transition zone, peripheral zone tumour and transition zone tumour were significantly greater than LS estimates ($p < 0.001$ to $p = 0.003$). There was no significant difference between ML and LS ADC estimates of normal peripheral zone ($p = 0.674$). Tumour ADC was significantly lower than the respective normal prostate zone whether estimated by ML or LS algorithms ($p < 0.001$ to $p = 0.013$). A slight increase in contrast between tumour and normal tissue was observed for ML estimates (+ 4.27% in peripheral zone and +7.47% in transition zone).

	Peripheral zone (PZ) - Normal	Transition zone (TZ) - Normal	Peripheral zone (PZ) - Cancer	Transition zone (TZ) - Cancer	TZ Normal vs. Cancer (p-value)	PZ Normal vs. Cancer (p-value)
LS median ADC (x10^{-3}mm2/s) ± SD	1.61 ± 0.45	1.22 ± 0.33	0.93 ± 0.34	0.71 ± 0.14	<0.001 *	0.013 *
ML median ADC (x10^{-3}mm2/s) ± SD	1.71 ± 0.40	1.37 ± 0.40	0.99 ± 0.31	0.80 ± 0.16	<0.001 *	<0.001 *
ML vs. LS (p-value)	0.674	0.003 *	0.002 *	<0.001 *		

Table 3.4: Least Squares and Maximum Likelihood estimates of ADC for normal and cancerous tissue in patient peripheral zone and transition zone. No statistical difference could be observed between the two types of estimates in normal peripheral zone, where the SNR is the highest. However LS estimates where statistically lower in the other tissues (indicated by '*').

Visual assessment of the difference between ADC maps obtained with the ML and those obtained with the LS did not reveal significant changes. The two evaluations of the data resulted in the following: Radiologist 1 preferred the ML ADC map in 22% of the cases, the LS ADC map in 22% and did not have a preference in 56% of the cases. In only 1 case the ML map was considered as 'much better' compared to the LS map, in all the other cases where there was a preference it was quantified as 'slightly better'. Radiologist 2 preferred the ML ADC map in 33% of the cases, the LS ADC map in 50% and did not have a preference in 17% of the cases. Here, all the preferences were quantified as 'slightly better'. Figure 3.11 shows examples of the compared ADC maps along with the corresponding T2 images.

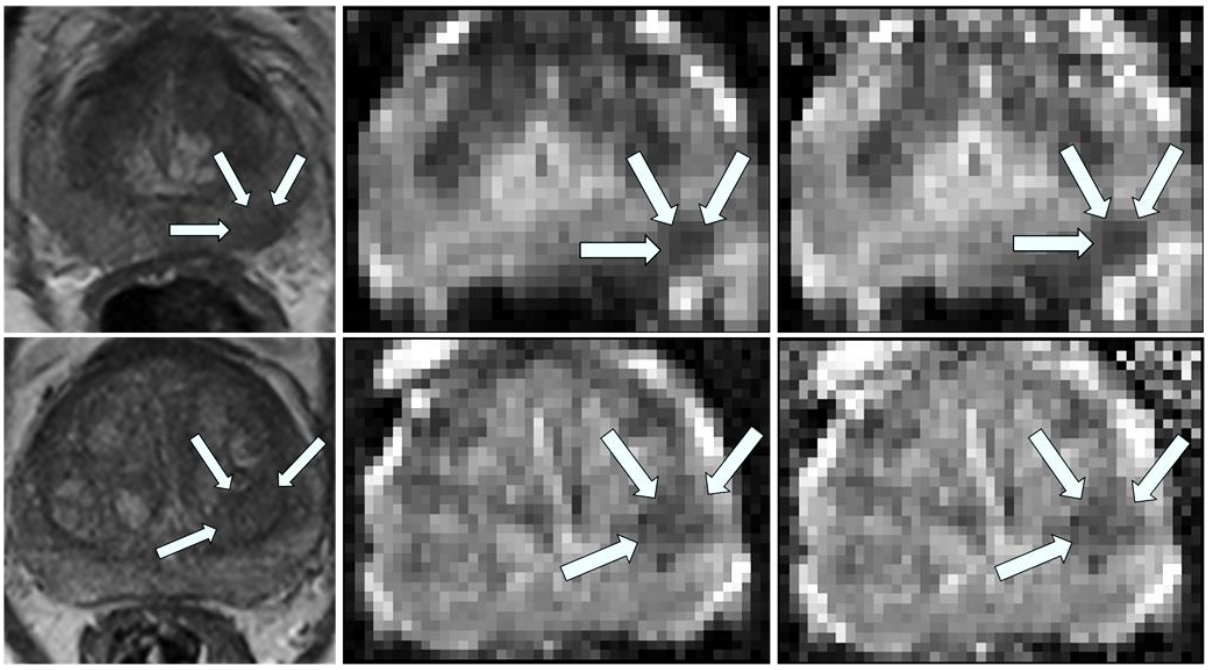

Figure 3.11: Examples of ADC maps generated using the two approaches for two different patients. Each row corresponds to a patient for which the T2 image (left), LS ADC (centre) and ML ADC (right) maps are displayed. All three image type cropped tight to the prostate area. For the first example, the ML map was considered as slightly better by the two radiologists, and for the second example, the ML map was considered as much better by radiologist 1 and slightly better by radiologist 2.

3.3.4 Discussion

A global increase of ADC values could be observed when applying ML estimation to clinical data. The difference in ADC between cancer and normal peripheral zone tissue appeared clearly with both methods and was relatively more important for ML estimates. These findings agreed with results presented in previous preclinical studies on mice [51]. However, this increase in difference did not seem to be sufficient to have a clinical impact given the way ADC maps are currently used. In particular, no significant change in conspicuity of lesions by radiologists could be highlighted between maps resulting from the two types of estimation.

3.4 **Rician Bias Correction**

3.4.1 Theory

This section presents a method for DWI modelling, accounting for parallel imaging induced spatially varying noise, and data averaging. Cardenas-Blanco et al. [67] adapted an iterative method (based on statistical moments) proposed by Koay et al. [64], to derive an analytical expression for the Rician bias correction in the case of non-averaged data. The first and second moments of the distribution of magnitude data M, are given by the following expressions:

$$\langle \mathrm{M} \rangle = \sqrt{\frac{\pi}{2}} \frac{(2\mathrm{N}-1)!!}{2^{\mathrm{N}-1}(\mathrm{N}-1)!} \, {}_1\mathrm{F}_1\left(-\frac{1}{2}, \mathrm{N}, \frac{\mathrm{S}^2}{2\sigma_\mathrm{G}^2}\right)\sigma_\mathrm{G} \tag{3.6}$$

and,

$$\langle \mathrm{M}^2 \rangle = 2\mathrm{N}\sigma_\mathrm{G}^2 + \mathrm{S}^2 \tag{3.7}$$

where N is the number of receiver coils, the operator $(.)!!$ is the odd factorial, σ_G is the standard deviation of the underlying Gaussian distribution, and ${}_1\mathrm{F}_1$ is the confluent hyper-geometric function. Then using (3.6) and (3.7) a proportional relationship between σ_G^2 and the variance of the magnitude signal σ_R^2 can be derived:

$$\sigma_\mathrm{R}^2 = \langle \mathrm{M}^2 \rangle - \langle \mathrm{M} \rangle^2 = \xi(\theta, \mathrm{N})\, \sigma_\mathrm{G}^2 \tag{3.8}$$

where $\theta = S/\sigma_\mathrm{G}$ (i.e. the SNR) and $\xi(\theta)$ is a correction factor defined as:

$$\begin{gathered} \xi(\theta, \mathrm{N}) = 2\mathrm{N} + \theta^2 - \beta_N^2 \left[{}_1\mathrm{F}_1\left(-\frac{1}{2}, \mathrm{N}, \frac{\mathrm{S}^2}{2\sigma_\mathrm{G}^2}\right)\right]^2 \\ \beta_N = \sqrt{\frac{\pi}{2}} \frac{(2\mathrm{N}-1)!!}{2^{\mathrm{N}-1}(\mathrm{N}-1)!} \end{gathered} \tag{3.9}$$

θ can be iteratively estimated using a fixed point formula derived from equations (3.8) and (3.9):

$$\theta = \sqrt{\xi(\theta, \mathrm{N}) \left(1 + \frac{\langle \mathrm{M} \rangle^2}{\sigma_\mathrm{M}^2}\right) - 2\mathrm{N}} \tag{3.10}$$

Provided that a prior estimate of σ_R is available, equation (3.10) provides an estimate for both the standard deviation σ_G and the correction factor ξ. Finally, using the latter in association with the binomial expansion of the square root, one can retrieve an unbiased estimate of S:

$$S^2 = \langle M \rangle^2 - q^2\sigma_G^2 \tag{3.11}$$

$$q^2 = \left(2 - \xi(\theta)\right) \tag{3.12}$$

$$S = M - \langle M \rangle \left[\frac{1}{2}\left(\frac{q\sigma_G}{\langle M \rangle}\right)^2 + \frac{1}{8}\left(\frac{q\sigma_G}{\langle M \rangle}\right)^4 + \cdots\right] \tag{3.13}$$

Olariu et al. extended the application of such a bias correction scheme to averaged DW-MR data [68]. As illustrated in Figure 3.2 bias correction is necessary in averaged data in particular when the SNR is poor (i.e. when the Rician bias is particularly important). Once the bias correction has been carried out, there is no need to account for the noise distribution in the fitting process and the LS estimation should provide accurate estimates of the ADC.

3.4.1.1 Noise parameter estimation

As noise is considered as non-stationary, σ_R ideally should not be directly estimated from a background region. Instead we chose a method [55] based on the work published by Coupé et al. [65], adapting a median absolute deviation (MAD) technique to averaged Rice distributed data. The 2D magnitude DW images are decomposed (Haar wavelet decomposition) into four sub-bands (LL, HL, LH, HH, L = low, and H = high frequencies). The lowest sub-band (LL) mainly corresponds to the object, and thus can be used as a mask for the object region. Having segmented the object, the underlying Gaussian noise standard deviation σ_G is estimated from the wavelet coefficients (y_i) corresponding to its HH sub-band [55].

$$\sigma_G = \frac{\text{Median}(|y_i|)}{0.6745} \tag{3.14}$$

3.4.2 Data and Experiments

The same clinical data as described in 3.3.2.2 were used, as well as the methods used to assess the accuracy of ADC estimation. This paragraph only describes simulation based experiments. As robustness to non-stationary (i.e. spatially varying) noise was assessed, image based simulation were used in all cases.

3.4.2.1 Monte Carlo Simulation

Similar to paragraph 3.3.2.1, a Monte Carlo simulation was run to assess the effect of Rician bias correction (RBC) on LS estimates of ADC. For SNR values in the interval $[1 - 15]$ sets of DW-MR images were generated using a simulator of noisy GRAPPA acquisition data developed by Aja-Fernandez et al. [60], [63] which had been modified to incorporate SMF reconstruction. Images were created at b-values of $[0\ 150\ 500\ 1000]$ (s.mm^{-2}) with the same S_0 and ADC values as in paragraph 3.3.2.2, using 2 receiver coils, an acceleration factor of 2, and assuming no correlation between the coils. For each ADC and SNR, multiple data sets were created providing measurements for averaging using 1 and 16 averages. Each attempt was based on 5×10^4 samples (i.e. averaged pixels). This is summarized in Figure 3.12. According to Dietrich et al. [58] images obtained with GRAPPA/SMF are expected to be Rician distributed. Therefore in each scenario (b-value, SNR, ADC, number of averages) RBC was applied. Data distribution before and after RBC were compared using the ground truth signal value as reference.

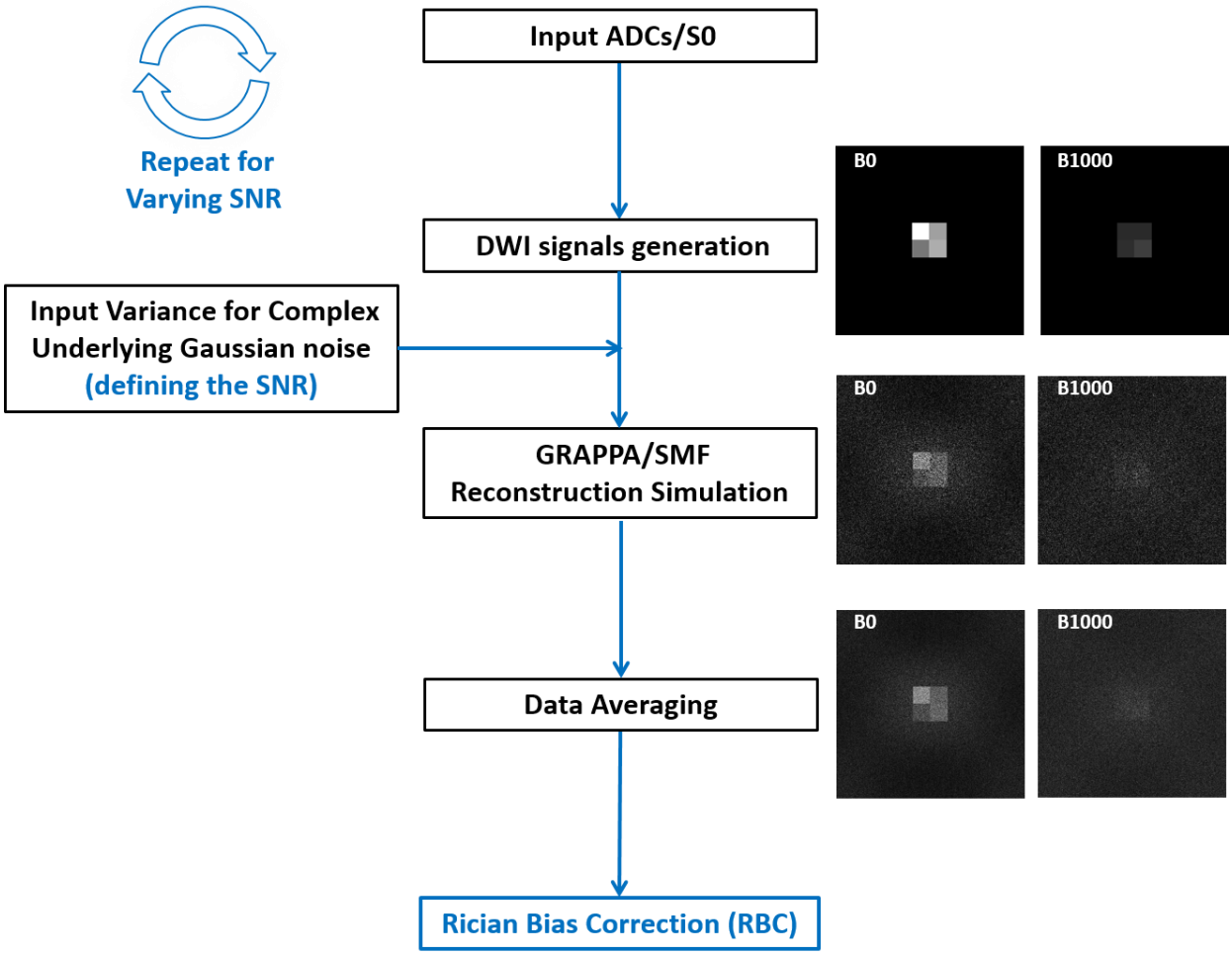

Figure 3.12: Flow chart of Parallel imaging simulation. Data are created based on a given set ADC values and a B_0 image, then Rician noise is introduced using GRAPPA/SMF simulation with the specified SNR and the resulting images are averaged

3.4.2.2 Phantom based simulations

Similar to paragraph 3.3.2.2, phantom simulations were run to assess the effect of RBC on ROI based LS estimates of ADC. Data were generated the same way as shown in Figure 3.6, but using GRAPPA/SMF reconstruction simulation and multiple averaging. The experiment was repeated for 1 and 16 averages.

3.4.3 Results

3.4.3.1 Monte Carlo Simulation

Applying RBC to noisy averaged signals showed an important reduction of the Rician bias. The effect was variable depending on the initial SNR (in the b_0 image before averaging) and

the number of averages used. However RBC always reduces the observed bias (see example Figure 3.13). In particular, it was observed as expected that the lower the SNR, the bigger the bias. Also the number of averages only affects the standard deviation and the shape of the distribution. Although there is an important reduction of the noise induced shifting, a residual bias remains after correction as expected. It should be noticed that the given SNR values is for the non-averaged b_0 data.

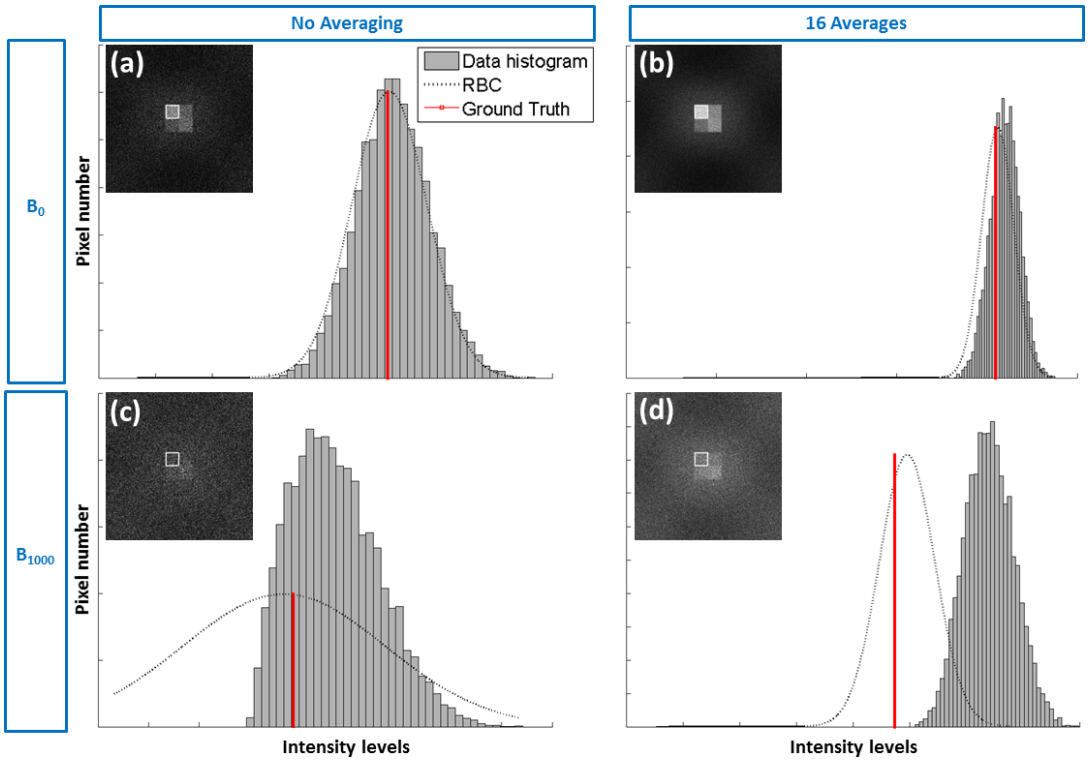

Figure 3.13: Effect of Bias Corrections on pixel intensities distribution for SNR_0 = 4. Examples at b_0 for no averaging (a) and 16 averages (b), and at b_{1000} for no averaging (c) and 16 averages (d). RBC always reduces the bias due to Rician distribution (for low SNR in b_{1000} images). In each case the image data is shown with the area analysed contoured in white.

For both non-averaged and averaged data, estimates of ADC obtained after applying RBC were closer to the "ground truth" ADC (see Figure 3.14). The improvement in median percentage error with RBC was always higher than 5 % compared to LS alone, and up to 70% for higher ADCs at low SNR. It was also observed that the effect of LS was very similar with either 1 or 16 averages. The SNR values presented here correspond to non-averaged data. These values were kept for better clarity when comparing the different graphs. However in the presence of averaging the actual SNR is increased.

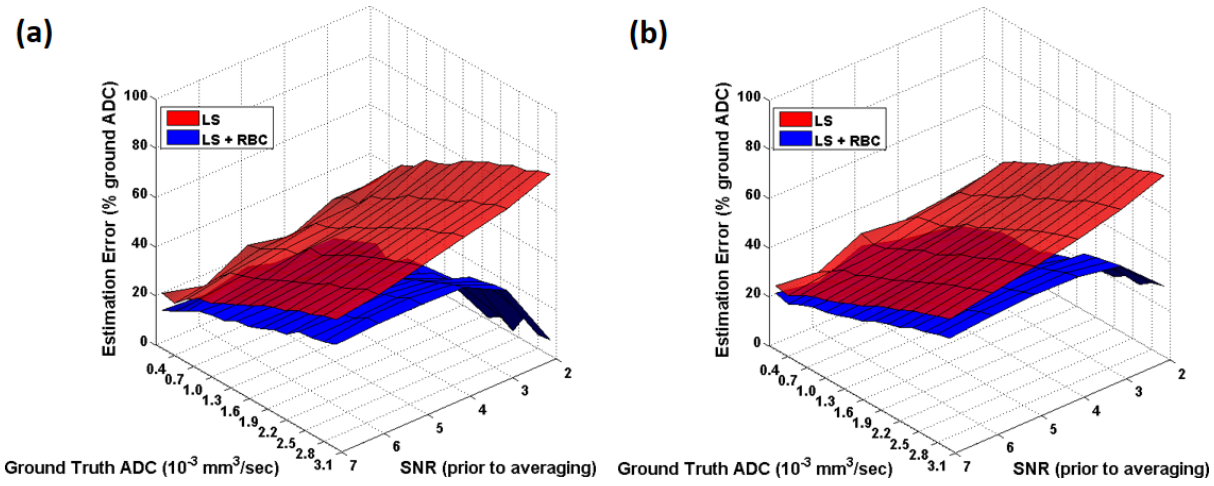

Figure 3.14: Monte Carlo simulations for ADC values from 0.1 to 3.1 10^{-3} mm^2/s and SNR values from 2 to 7 for non-averaged data (a), and averaged data using 16 averages (b). The graphs show 3D surfaces representing the median of absolute error of estimates compared to the ground truth ADC value, obtained with LS alone (red) and with LS+RBC (blue). Results are presented as a percentage of the ground truth ADC.

Similar to 3.3.3.1, the IQR obtained for typical ground truth ADC values for tumour (e.g. 0.9 x 10^{-3} mm^2/s) and normal peripheral zone tissue (e.g. 1.5 x 10^{-3} mm^2/s) was higher for estimates from RBC data. However this IQR difference between the two methods was only observed at low SNR and in the absence of averaging (see Figure 3.15). This can be explained from observations from Figure 3.13, at low SNR without averaging, RBC increases the spread of the strongly skewed distribution to get back to a Gaussian.

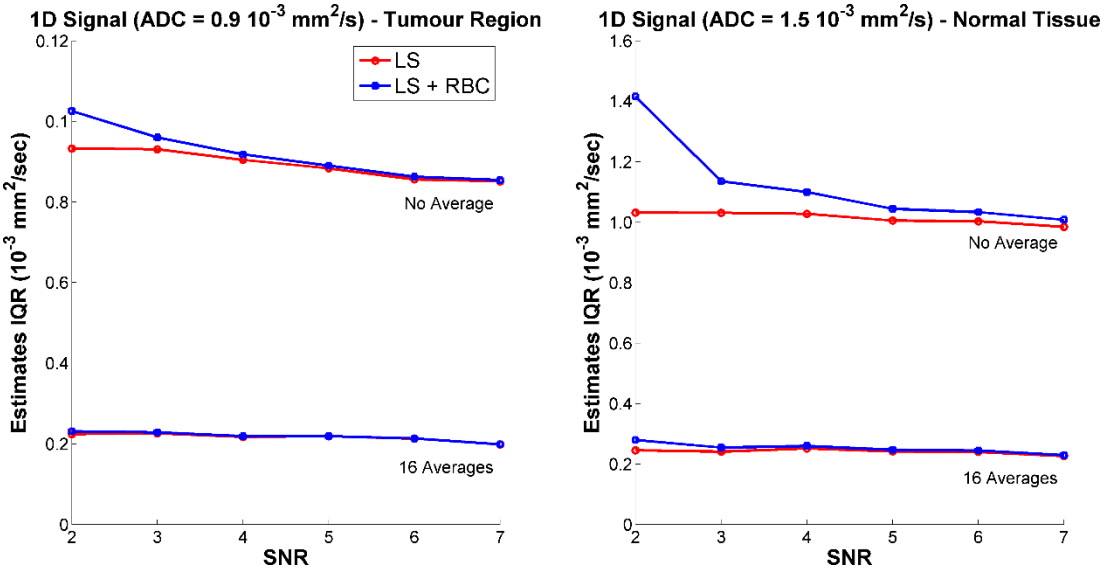

Figure 3.15: Monte Carlo simulations at ADC values of 9x10-4 mm2/s (left) and 1.5x10-3 mm2/s (right). These graphs show the inter-quartile ranges as a measure of deviation for the LS alone (red circles) and the LS+RBC (blue squares) obtained for various SNR values.

3.4.3.2 Phantom Simulations

The median percentage error and IQR for repeated estimates of ADC performed at each of the increasing tumour and normal tissue ROI sizes is illustrated for both transition zone and peripheral zone using LS and LS with RBC in Figure 3.16 and Figure 3.17. Median percentage error was consistently higher for LS alone (up to 20%) compared with RBC for tumour and normal tissue for ROI sizes greater than 10 pixels for non-averaged data. However, there was no obvious difference between the two methods in the case of averaged data.

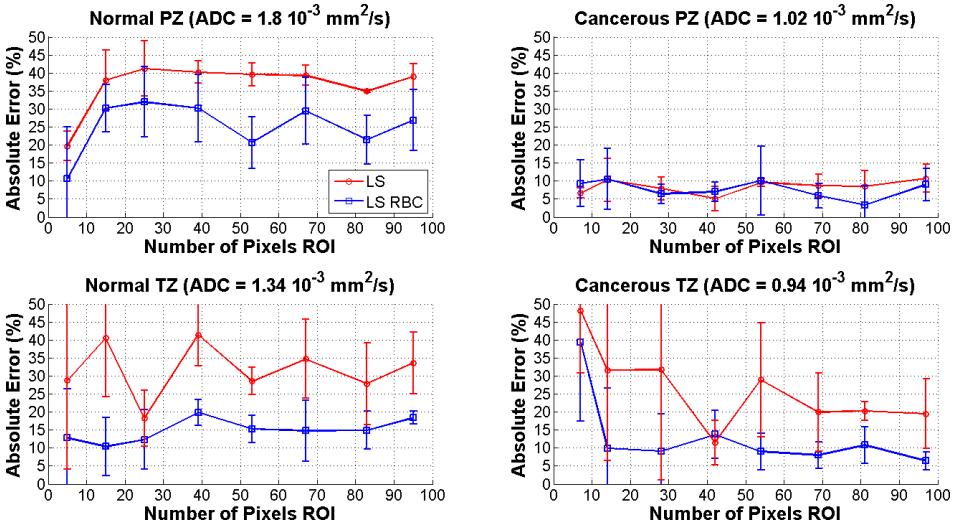

Figure 3.16: Result estimates of phantom experiment with no averaging. The graph show the median estimates for pixels in the normal tissue (left) and tumour ROIs (right) in peripheral zone (top) and transition zone (bottom) obtained with LS alone (red) and with LS+RBC (blue).

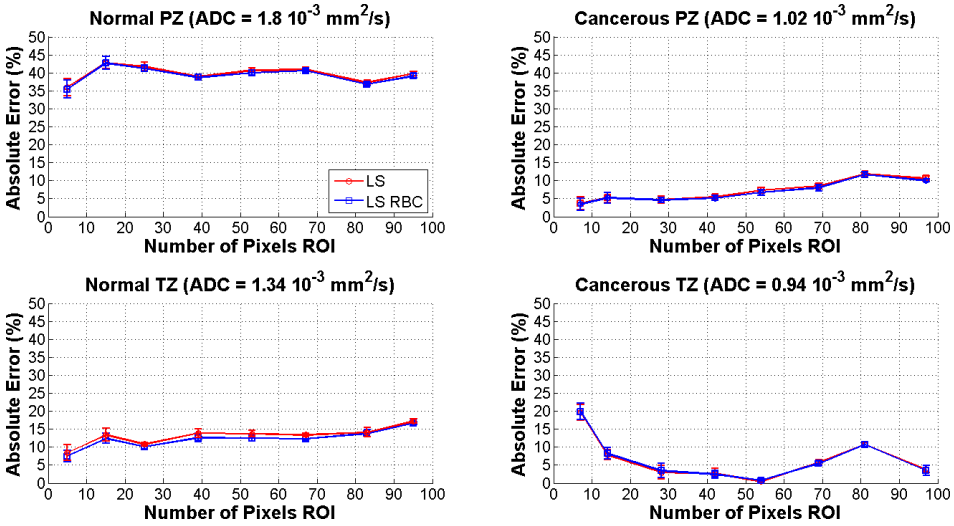

Figure 3.17: Result estimates of phantom experiment with 16 averages. The graph show the median estimates for pixels in the normal tissue (left) and tumour ROIs (right) in peripheral zone (top) and transition zone (bottom) obtained with LS alone (red) and with LS+RBC (blue).

3.4.3.3 Clinical Data

Table 3.5 shows the SNR measurement in b_0 images across the 18 patients using Koay's method. It yielded different results compared to those based on background regions. The maximum and minimum SNR calculated was 15.52 and 5.1 for tumour in the transition and peripheral zone respectively, and 24.9 and 5.57 for normal tissue. These results are based on noise measurements in the object region in averaged data. Since data were acquired using 16 signal averages the values given in Table 3.5 must be rescaled to obtain an estimation of the SNR before averaging [55].

	Peripheral zone (PZ)	**Transition zone (TZ)**	**PZ vs. TZ SNR (p-value)**
Mean SNR Cancer ± SD	11.31 ± 3.37	10.29 ± 3.68	0.52
Mean SNR Normal ± SD	16.19 ± 6.58	12.97 ± 5.48	0.27
Cancer vs. Normal SNR (p-value)	0.08	0.33	

Table 3.5: SNR values obtained in 18 patients for cancerous and normal tissue in either peripheral or transition zone based noise measurement in the object region. No significant difference could be observed between the two types of tissue in both areas

Median ADC estimates for LS with and without RBC in normal peripheral and transition zone, and peripheral and transition zone tumour is given in Table 3.6. No significant difference could be observed in the different types of tissues. This is consistent with simulation based results given the computed SNR levels.

Due to the limited difference in ADC estimates obtained with the two methods, no visual assessment of ADC maps was performed in this part of the study.

	Peripheral zone (PZ) – Normal	Transition zone (TZ) - Normal	Peripheral zone (PZ) - Cancer	Transition zone (TZ) - Cancer	TZ Normal vs. Cancer (p-value)	PZ Normal vs. Cancer (p-value)
LS median ADC ($x10^{-3}$ mm^2/s) ± SD	1.7 +/- .30	1.2 +/- .40	0.91 +/- .46	0.96 +/- .70	0.34	0.00021
LS+RBC median ADC ($x10^{-3} mm^2/s$) ± SD	1.8 +/- .30	1.3 +/- .40	0.94 +/- .46	0.98 +/- .71	0.32	0.00018
LS vs. LS +RBC (p-value)	0.75	0.85	0.91	0.95		

Table 3.6: Least Squares ADC estimates with and without RBC for normal and cancerous tissue in patient peripheral zone and transition zone. No statistical difference could be observed between the two types of estimates in the different type of tissue

3.4.4 Discussion

As observed with ML a global increase of ADC values was obtained when applying RBC to clinical data. Despite the specificity of RBC to account for a more realistic type of noise distribution, there was no significant difference with LS estimates. Here again, the changes obtained in ADC estimates did not seem to be sufficient to have a clinical impact given the way ADC maps are currently used. However, simulations showed a possible benefit of using RBC at low SNR.

3.5 Analytic Formulation of the Averaged PDF with Maximum Probability Estimation

This last section describes the work published in Dikaios et al. [55] to which the author contributed. A summary of this work is presented here. The application is focused on head and neck tumours. Contrary to prostate cancer, head and neck tumours present a decreased cellularity compared to surrounding normal tissue, resulting in an increase of ADC [55].

3.5.1 Theory

This section introduces an analytic approach to account for the effect of averaging on the statistical distribution of DWI magnitude data. Assuming Rice distributed data in each of the $\mathrm{N_{avg}}$ measurements used for averaging, the global PDF of the resulting averaged data is given by the convolution of each Rician PDF:

$$\mathrm{p_{avg}} = \mathrm{p_1} \otimes \mathrm{p_2} \otimes \ldots \otimes \mathrm{p_{N_{avg}}} \tag{3.15}$$

However the Rician distribution is expected to be the same in each measurement, hence (3.15) is equivalent to:

$$\begin{gathered}\mathrm{p_{avg}} = \mathrm{FT^{-1}}(\mathrm{FT}(\mathrm{p_{Rice}})^{\mathrm{N_{avg}}}) \\ \mathrm{p_{Rice}} \approx \mathrm{p_1} \approx \mathrm{p_2} \approx \cdots \approx \mathrm{p_{N_{avg}}}\end{gathered} \tag{3.16}$$

where FT is the Fourier Transform operator. Given the expression in equation (3.2), the averaged PDF in noisy DW-MRI can finally be modelled using the following approximation:

$$\begin{gathered}\mathrm{p}(\mathrm{M}|\mathrm{S},\sigma_\mathrm{R}) = \\ \frac{\mathrm{c_2 M}}{\sigma_\mathrm{R}^2} \times \left(-\frac{\mathrm{c_2 M}}{\mathrm{c_1 S}}\right)^{\mathrm{N_{avg}}} \exp - \left(\frac{\mathrm{c_2 M} + \mathrm{c_1 S}}{\sigma_\mathrm{R}^2}\right) \mathrm{I}_{\mathrm{N}_{avg}-1}\left(\frac{\mathrm{c_2 M} + \mathrm{c_1 S}}{\sigma_\mathrm{R}^2}\right)\end{gathered} \tag{3.17}$$

where c_1 and c_2 are constant that can be optimized by fitting the model in (3.17) to the convolution of the Rician PDFs in equation (3.15) [61]. An estimate of the noise parameter σ_R was computed using the MAD technique described in 3.4.1.1, combined with equation (3.8).

3.5.1.1 Curve Fitting

The model fitting was achieved using a maximum probability (MP) approach proposed by Kristoffersen et al. [61] to provide unbiased ADC estimates. Instead of applying LS fitting based on the difference between the measured signal and the model directly, one can use the difference between measurements and MP of the expected distribution for each b-value.

The MP of the PDF can be numerically computed respectively from equations (3.18).

$$\left.\frac{\partial p(M_i|S(b_i),\sigma_R)}{\partial M_i}\right|_{M_i=MP} = 0 \tag{3.18}$$

These two approaches were used in [55], within non-linear regression based on the L_1-norm (i.e. the sum of absolute values) for increased robustness to outliers.

$$L_{MP} = \sum_{i=0}^{N} |M_i - MP_i| \tag{3.19}$$

3.5.2 Data and Experiments

This study was focused on the application of DWI imaging of head and neck cancer, which differs from the previous sections.

3.5.2.1 Simulation

Simulated datasets for both non-averaged and averaged DWI were firstly generated to evaluate the accuracy of noise estimation. Noise-free DWI containing both normal tissue and tumour ROIs were created using signal values from an example clinical dataset. In this case six b-values were utilized: $[0\ 50\ 100\ 300\ 600\ 1000]$ (s.mm^{-2}). Just like in paragraph 3.4.2.2, noise-free data were corrupted with noise and averaged four times. The SNR in the averaged data was chosen so that values varied between 3 and 8 in the b_{1000} image, which differs from the previous sections. These data were used to assess the ability of the MAD technique combined with the mono-exponential MP fitting to correct for the Rician bias. In the following paragraphs, such a technique is referred to as MP for clarity.

3.5.2.2 Clinical Data

A set of 24 clinical DWI scans from patients with confirmed head and neck squamous cell carcinoma, was used for this study. 16 healthy subject DWI were used as controls. Trace DW images of the head and neck were acquired at 1.5T (Magnetom Avanto, Siemens, Erlangen, Germany) with two receiver coils using GRAPPA. Data reconstruction was carried out using SMF denoted as adaptive combine by the manufacturer. Again, as predicted by Dietrich et al. [58] data resulting from such an acquisition scheme are expected to be Rician distributed. Images were averaged four times for improved SNR.

Diffusion gradients were applied in 3 orthogonal directions at each of 6 b-values $[0\ 50\ 100\ 300\ 600\ 1000]$ (s.mm^{-2}). Further details on data acquisition are provided in Table 3.7. In each dataset, cancerous or normal cervical nodes ROIs were contoured by a radiologist.

Sequence type	Echo Planar (STIR-EPI)
Repetition Time (ms)	8700
Echo Time (ms)	88
Slice Thickness (mm)	4
Image Matrix (pixel^2)	128x128
Field of View (mm^2)	260x260
Parallel Acquisition (iPAT)	GRAPPA with Adaptive Combine Reconstruction (SMF)
Number of averages	4
b-values (s/mm^2)	0;50;100;300;600;1000
Total Acquisition Time (min:s)	6:10

Table 3.7: Details of head & neck DW-MRI acquisition sequence.

ADC maps were generated using the MP estimation scheme. Results were compared to a modified version of the LS algorithm, replacing the squared difference in equation (3.3) by the L_1-norm of the difference.

3.5.3 Results

3.5.3.1 Simulation

Table 3.8 illustrates the performance of MP fitting compared to LS applied to simulated data. Compensating for the Rician bias is advantageous in case of low SNR. However the difference between MP and LS estimates decreases for increasing SNR values.

	SNR = 3	SNR = 5	SNR = 8
Ground Truth ADC (mm^2/s)	1.31	1.31	1.31
LS estimate (mm^2/s)	0.91	1.18	1.26
MP estimate (mm^2/s)	1.24	1.3	1.3

Table 3.8: ADC estimates in simulated data using MP fitting with the analytical formulation for the averaged noise distribution. Results are for the tumour ROI in the simulated field of view.

3.5.3.2 Clinical Data

Across all b-values, the SNR in the contoured ROIs were always higher than 9.4 in cancer nodes and higher than 6.4 in normal nodes. Table 3.9 presents the median and IQR of ADC estimates across all patients for both normal tissue and tumour ROIs. No significant difference was observed between the two types of estimates ($p = 0.06$ in terms of the Mann-Whitney U-test). Although there was a significant difference between the estimated ADC from different types of tissue with both LS ($p = 0.01$) and MP ($p < 0.01$), no method was preferred.

	Normal tissue		**Tumour**	
	Median	IQR	Median	IQR
LS estimate (mm^2/s)	1.14	0.26	1.02	0.17
MP estimate (mm^2/s)	1.21	0.29	1.02	0.18

Table 3.9: ADC estimates (Median and IQR) in clinical head and neck DWI. Results are taken across all patients for both normal and tumour ROIs.

3.5.4 Discussion

Simulation based experiments demonstrated the benefit of using an analytical formulation of the averaged distribution at low SNR. However, in a clinical context, no advantage was found in using such a model within the MP scheme compared to LS due to the high SNR observed in both normal and cancer nodes.

3.6 **Discussion and Conclusion**

Diffusion weighted imaging is increasingly used for assessing prostate cancer [72]–[74]. The recent European Society of Uro-Radiology guidelines on prostate MRI includes the routine use of an ADC image for evaluation of prostate tumours [75]. Beyond visual assessment alone, there is significant interest in using quantitative ADC values to aid detection [71], treatment monitoring [76], active surveillance and even Gleason grading [48] of tumours. Likewise, DWI is of interest in the characterization of several types of head and neck tumours [45], [50], [77], [78].

Establishing a standardised ADC assessment methodology remains a challenge given the variety of scanning options and differences between MR hardware manufacturers [63]. Whilst there has been a focus on homogenising the acquisition of diffusion weighted images to improve reproducibility, the extent and impact of errors resulting from assumptions made in calculating ADC values has not been investigated as much.

3.6.1 Validity of noise model

A good understanding and appropriate modelling of noise is essential for relevant analysis of DW-MR data, and more generally for the analysis of any type of quantitative MR data. In this study, clinical DW-MR data were acquired using parallel imaging with 2 receiver coils and multiple averages. Considering this, several hypotheses were made, all assuming Rice distributed data. In the first instance, the imaged field of view was considered small enough to assume that the non-stationary characteristics of noise could be neglected. Also if a Gaussian is considered as a particular case of Rician distribution, then the ML technique is still valid for ADC estimation at high SNR or in averaged data. In a second step, non-stationary noise in the presence of averaging was taken into account in the model leading to data pre-processing using RBC. Finally the effect of averaging was included in the noise model to provide a fully analytical approach, MP, for bias correction.

Each approach has limitations. The use of ML relies on possible over simplification of the nature of noise and both RBC and MP require a series of complex processing which may increase the risk of error propagation.

3.6.2 Clinical Impact

DW-MRI, more particularly ADC mapping, in association with other MR imaging schemes is of interest for cancer diagnosis and grading. Thus, obtaining accurate and reliable values of ADC in tumour areas is crucial. This study addresses the estimation of ADC from DW-MR data in the case of human prostate, and head and neck cancer.

Results obtained from simulations showed an increase in accuracy with all the investigated methods (i.e. maximum likelihood estimation, rician bias correction, maximum probability) when compared to LS estimation. Phantom based simulation allowed the assessment of estimates accuracy in ROIs with varying sizes for both prostate peripheral and transition zone. Such an approach was closer to real data analysis than using 1-dimensional signals. Realistic S_0 values were also incorporated to the data in these experiments.

Improving the reproducibility of ADC values is critical if they are to be adopted into routine clinical decision-making processes. The first step is to understand the causes, magnitude and clinical effects of errors in ADC. Our results highlight the importance of the image-processing step and indicate that alternative methods to estimate ADC could provide values more accurately reflecting tissue characteristics. The results also highlight the significance of maintaining an adequate SNR of DW-MR images. Whilst our work has been focused on specific application (i.e. prostate or head and neck cancer) it has equal implication for many other body site where ADC estimates are being clinically considered (e.g. brain, liver, breast) [45]. With regard to prostate cancer imaging, improving the reliability and reproducibility of ADC estimates will further improve threshold based tumour detection strategies; could provide a means of active surveillance [79] of patients where changes in ADC may precede changes in tumour size; or improve estimation of tumour Gleason grade from ADC values [48].

3.6.3 Data Acquisition

Simulations results suggest that the robustness of the described methods at low SNR could alleviate the need for higher number of measurements (e.g. 16) leading to shorter acquisition times and avoiding errors due to patient motion between measurements. Higher spatial resolution might also be possible.

3.6.4 Conclusion

It was found that accounting for noise in the analysis of DW-MRI improves the accuracy of ADC estimates of cancerous and normal tissue (e.g. by 4-20% in the cases of prostate transition zone tumours). An increase of the difference between tumour and healthy tissue ADCs can also be observed in some cases of prostate imaging. However, these changes were not significant enough to have an impact on current clinical use of DW-MRI.

This work highlighted the necessity to use accurate noise modelling in clinical DWI and the important influence of acquisition strategies on the expected nature of the noise distribution. Results based on simulations indicate that the use of the described methods for image analysis in clinical routine might allow changes in data acquisition such as reducing the number of averages.

Some of the work presented in this chapter (section 3.5) will be used for the derivation of ADC in the study described in chapter 6.

4 Robust Data Decomposition Registration – respiratory motion correction in DCE-MRI

4.1 Introduction

In this chapter we address the challenge of respiratory motion correction in DCE-MRI. Following a description of what image registration is and a presentation of the existing methods to register DCE-MR data, we introduce our method named Robust Data Decomposition Registration (RDDR). The validation and discussion of such a technique are finally presented. The work presented in this chapter led to conference publications describing the concept of RDDR at ISMRM 2012 [80] and its application at ISMRM 2013 [81]. The complete version of this work was published in Medical Image Analysis journal [82].

4.2 Motion correction in DCE-MRI

In order to monitor contrast agent uptake and washout in DCE-MRI, acquisition times of the order of minutes are required. Hence patient motion (e.g. breathing, heartbeat and bowel peristalsis) during the acquisition can cause inter-frame misalignments. In extreme cases, the magnitude of motion due to breathing can be as large as 80 mm [83] along the superior-inferior axis in organs close to the diaphragm. These misalignments have a strong impact on the analysis of DCE-MRI since apparent intensity changes will be related to a mixture of motion and contrast agent changes, potentially corrupting the derived enhancement parameters and yielding incorrect information on tissue properties; in particular, motion during the contrast agent arrival phase can bias the estimation of pharmacokinetic parameters used to assess local tissue perfusion. Thus, correcting for motion is essential to get relevant information from the data. Several techniques have been developed to account for it during data acquisition directly. For example, the generalized reconstruction by inversion of coupled systems [41], which uses extra physiological measurements (e.g. pneumatic respiratory belts) as a model and compensates motion in

raw dynamic MR data. A modified version of this method using a contrast enhancement model has been applied to DCE-MRI [84]. Alternatively image registration [38] can be applied to achieve retrospective motion correction. In this work we chose to focus on this type of technique.

4.2.1 Registration

Image registration consists of aligning the same features in two different images (the source and the target) by establishing spatial correspondences. An example is shown Figure 4.1. There are two main class of registration algorithm: intensity based and feature based registration.

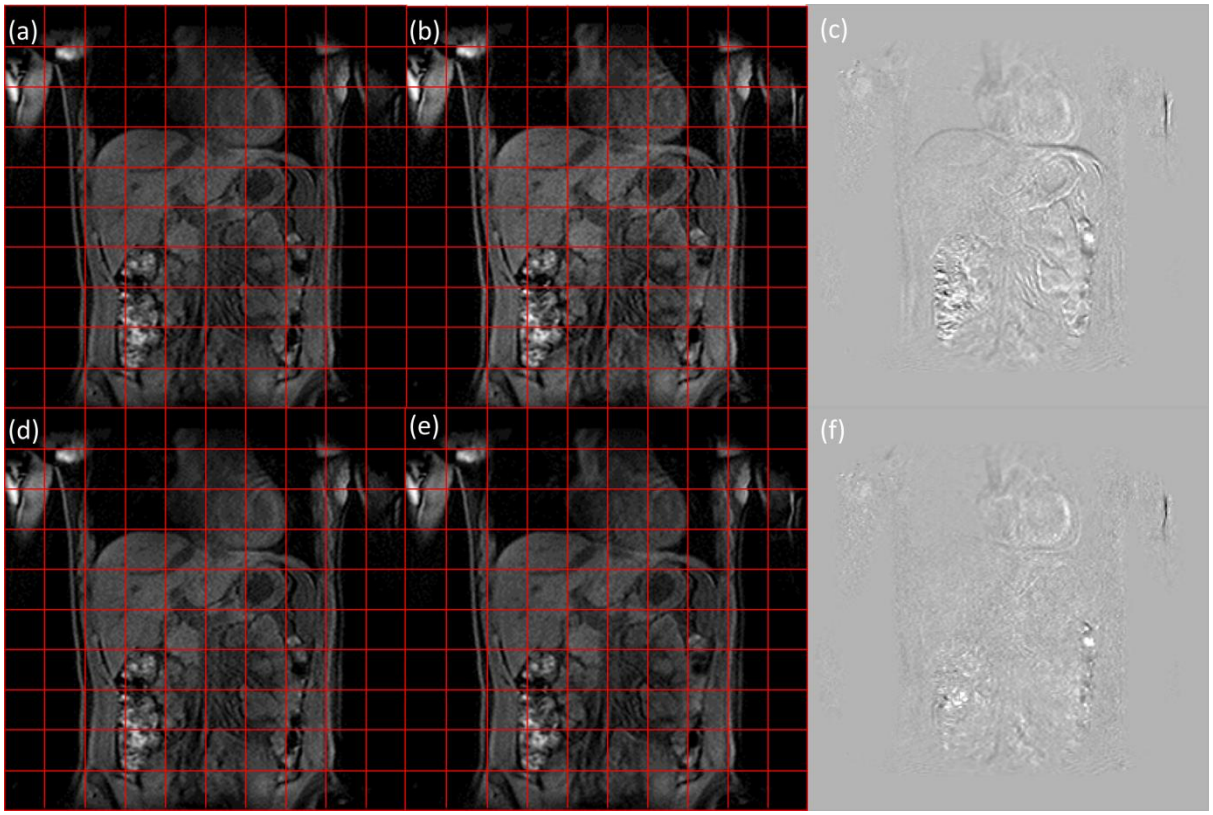

Figure 4.1: Example of image registration. A grid is overlaid on the target image (a, d), the source image (b) and the registered source image (e) to highlight the geometrical differences. Difference image before (c) and after registration (f) show the effect of feature realignment. Remaining elements in (f) are essentially noise and intensity variations between the two images.

Intensity based registration algorithms typically contain three elements: the similarity measure, the transformation model, and the optimization scheme. The similarity measure

compares the two images and measures how much different these are. It is embedded within an objective function which, when minimized (or maximized in some cases), stops the algorithm. Common similarity measures (summarized in Table 4.1) such as sum of squared difference (SSD) and correlation coefficients (CC) are based on intensity only. Others such as mutual information (MI) and normalized mutual information (NMI) are based on image entropy. Image entropy is a measure of information that uses the probability, p, of values occurring in image pixel [85]. Given that definition, MI can be seen as how well one image predicts the other, the better the features' alignment the better the prediction. NMI is similar to MI in terms of meaning but presents an increased robustness with respect to limited overlap between images [85].

Similarity measure	Expression	Possible values	Optimal value
SSD	$\frac{1}{N}\sum_{x\in I\cap J}\|I(x)-J(x)\|^2$	≥ 0	0
CC	$\frac{\sum_{x\in I\cap J}(I(x)-\bar{I})(J(x)-\bar{J})}{\left(\sum_{x\in I\cap J}(I(x)-\bar{I})^2\cdot\sum_{x\in I\cap J}(J(x)-J)^2\right)^{1/2}}$ where $\bar{I}$ and $\bar{J}$ are the mean value of the images	$[-1,1]$	1
MI	$H(I)+H(J)-H(I,J)$ where $H(I)=-\sum_{x\in I}p_I(x)\log(p_I(x))$ and $H(I,J)=-\sum_{x\in I}\sum_{y\in J}p_{IJ}(x,y)\log\left(p_{IJ}(x,y)\right)$	≥ 0	Depends on $H(I)$
NMI	$\frac{H(I)+H(J)}{H(I,J)}$	$[1,2]$	2

Table 4.1: Common similarity measures for image comparison based on intensity or entropy. Expressions are given for two images I and J to register, containing N pixels, indexed by x, each [38].

The transformation model computes a displacement vector for each pixel in the source images, resulting in a displacement field. Such a displacement field can be set to produce a rigid (i.e. only involving translation and rotation), affine (i.e. rigid plus sheering and scaling), or non-rigid (i.e. any deformation possible) transformation. In the particular case of a non-rigid transformation the deformation field can be computed for all pixels or for a limited set of control points and then extended to the entire image using interpolation. Limited control points can be useful to reduce the computational required time to complete registration. Note that specific constraints on the transformation can be incorporated through

regularisation terms in the objective function. Finally the optimization scheme makes the link between similarity and transformation. It aims at minimizing the similarity function by acting on the applied transformation. After each update of the transformation, the image similarity is computed (along with possible regularization parameters [86]). This process is iterated to find the best match between the two images. Common registration techniques use optimisation schemes such as: gradient descent, conjugate gradient, Gauss-Newton optimisation.

In feature based registration, a number of pre-defined pairs of landmarks in the two images are used to guide the transformation model. In some case the spatial correspondences between the landmarks can be available which alleviates the need for an optimization process. This type of registration is very intuitive. However it does require additional pre-processing to define the landmarks. All techniques mentioned in the following are intensity based.

In cases such as DCE-MRI where not only two images but multiple frames from a time series must be registered, several choices can be made depending on the data. A single frame (e.g. the first one) can be chosen as a target and all the others can be registered to that one. If changes are expected in a relatively long time period but limited changes occur between two consecutive frames, the series can be registered sequentially: the second frame is registered to the first one, the third frame is then registered to the (previously registered) second and so on. Finally a groupwise approach [87] can be utilized: the mean of all the frames is taken to produce the target image.

4.2.2 Existing methods

Several image registration methods have been developed to overcome the effect of motion and provide well aligned features across the time series. Nevertheless developing an (intensity based) registration scheme specific to DCE-MRI data is challenging since changes due to motion and those corresponding to contrast enhancement must be

differentiated. Conventional registration algorithms are likely to fail with DCE-MRI data as important local intensity changes across the different time-points can be interpreted as motion and produce a non-realistic expansion or contraction of the volume [86], [88].

The possibility of avoiding unphysical volume changes caused by local intensity variations due to contrast enhancement has been investigated in several studies. The multi-resolution fast free-form deformation (FFD) based on b-splines with NMI as a similarity measure by Rueckert et al. [89] has been used as a basis to address the problem of misalignments in DCE-MR time-series. In many cases a specific regularization term was introduced to limit non-realistic deformations [86], [88], [90]. Zheng et.al [91] developed a new method based on FFD in order to register breast images. In this approach a Lorentzian estimator is used as a similarity measure, combined with a reformulation of the energy function minimization using linear programming. Li et al. [92] recently registered high temporal resolution free-breathing contrast enhanced images of the bowel. In this method a retrospective respiratory gating is applied to the data and the remaining images are sequentially registered using a transformation model based on a combination of discrete cosine transformation basis functions [93].

Another class of methods dedicated to the problem of DCE-MRI registration are those that use a pharmacokinetic model to drive the registration processes. Hayton et al. developed a registration scheme that incorporates such a model and applied it to the analysis of breast images [94]. This relies on the assumption that the better the alignment between images in the time-series, the lower the residual difference between the model fit and the actual data. Therefore model fitting results can be used as a cost function for registration. Xiaohua et al. [95] proposed simultaneous segmentation and registration using Markov random fields combined with a similar model. Buonaccorsi et al. [96] introduced a method based on the modified Tofts model [11], [22]. By iteratively fitting such a model to the unregistered data, a motion-free synthetic time-series based on the resulting pharmacokinetic parameters map can be created and used as a reference for rigid registration. More recently Bhushan

et al. proposed a joint estimation of the deformation and contrast enhancement based on a Bayesian framework [97].

A further approach is to separate motion from contrast enhancement before registration. Melbourne at al. introduced an algorithm named progressive principal component registration (PPCR) that gradually removes misalignments [98], [99]. The method is based on the iterative use of principal component analysis (PCA) combined with a standard registration algorithm such as multi-resolution FFD [100]. In PCA, contrast changes are assumed to appear in the more significant principal components and motion in the less significant. This is used to create a synthetic motion-free set of target images using a limited number of principal components that correspond to contrast enhancement. It has been utilized to register both liver and breast data acquired using repeat breath-hold protocols [98], [99]. However the ability of PCA to disentangle motion from contrast enhancement depends on the nature of motion: for instance, the periodic motion of free breathing can appear in the more significant principal components along with contrast changes. More recently Wollny et al. investigated the use of independent component analysis to decompose data prior to registration in free breathing cardiac MRI [101]. In this case too, the objective is to remove motion elements to form a synthetic target time-series.

4.2.3 Proposed method

In this chapter we introduce a novel registration approach specifically designed to address the problem of misalignments in DCE-MR time-series. Similar to [98], [101] , our method is based on the assumption that motion can be separated from contrast enhancement, but here we chose robust principal component analysis (RPCA) for data decomposition [102]. RPCA reformulates decomposition as an optimization problem to recover the sparse and low rank components of the input data. Our hypothesis is that RPCA coupled with a registration algorithm based on residual complexity minimization [103] provides accurate registration of DCE time series in a broad range of organs and for various breathing

protocols. Given the explicit separation of a sparse term, RPCA should allow more flexibility and a greater degree of robustness than regular PCA, and can potentially benefit DCE-MRI registration. Importantly, it is expected to have a particular impact at critical times such as the arrival of contrast agent bolus.

4.3 Robust Data Decomposition Registration (RDDR)

4.3.1 Robust Principal Component Analysis (RPCA)

A common tool used in data processing and analysis is PCA. Given high dimensional input data, it uses singular value decomposition (SVD) to find a linear subspace with lower dimensionality that is the best adapted to the data. In that case the principal components correspond to the data projections on each axis of the estimated subspace. A limitation of PCA is its sensitivity to grossly corrupted inputs [102]. RPCA proposes a non-linear approach. Instead of a series of principal components that describe the data within a multidimensional space, only two components are computed: the low rank component representing the uncorrupted data and the sparse component corresponding to the perturbation, with no limitation in terms of magnitude (see Figure 4.2). Several studies investigating the feasibility and applications of RPCA have emerged recently [102], [104]–[106]. Let M be a Casorati matrix with each column being formed from all the pixels of a 2D time-frame. RPCA splits such a matrix into a low rank matrix L and a sparse matrix S. This is achieved under the constraint that the sum of L and S must correspond exactly to the initial dataset M. It was shown that such a decomposition can be formulated as an optimization problem [102]:

$$\begin{aligned} &\text{minimize } \|\mathrm{L}\|_* + \lambda\|\mathrm{S}\|_1 \\ &\text{subject to } \mathrm{L} + \mathrm{S} = \mathrm{M} \end{aligned} \tag{4.1}$$

where $||.||_*$ and $||.||_1$ respectively represent the nuclear norm (i.e. the sum of the matrix singular values) and the l_1-norm (i.e. the sum of the absolute values of the matrix

elements). The parameter λ appearing in equation (4.1) is a trade-off parameter controlling the weighting of the perturbation in the observed corrupted data. In practice it acts as a trade-off between the two components: for high values all the information will appear in L while S will be empty, and for low values L will contain the mean image through time while S will include all the variations with respect to the mean.

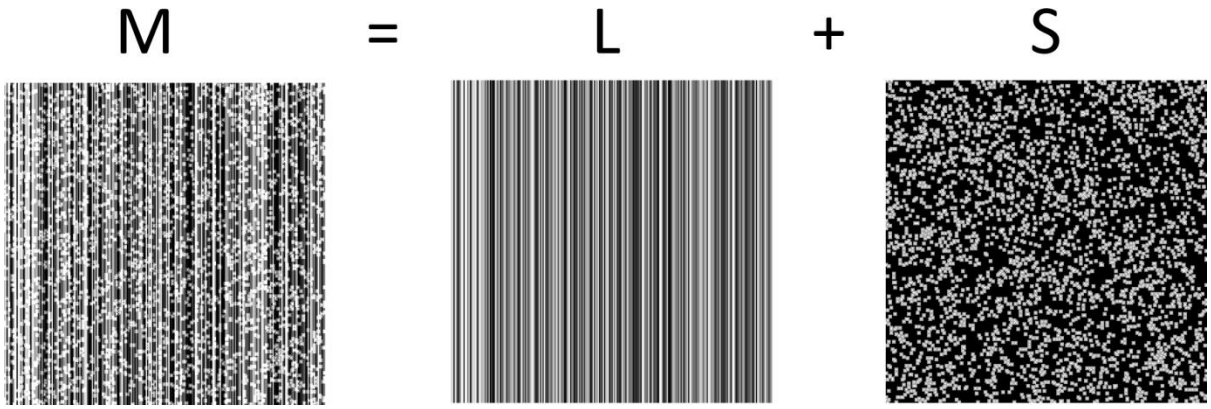

Figure 4.2: Example of image decomposition using RPCA. The observed matrix M is decomposed into the low rank component L and the sparse component S.

4.3.1.1 Augmented Lagrangian Multiplier

We chose the (inexact) augmented lagrangian multiplier (IALM) algorithm to solve the problem in (4.1) due to its speed and improved accuracy compared to other techniques [106]. This paragraph describes the different steps of such minimization. In the first instance the following notation are defined:

Let A and B be two matrices,

- $\|A\|_2$ is the square root of the sum of the squared elements of A
- $\|A\|_\infty$ is the maximum element of A in absolute value
- $\|A\|_F = \sqrt{\mathrm{tr}(A^* A)}$
- $J(A) = \max\left(\|A\|_2, {}^1\!/_\lambda \|A\|_\infty\right)$
- $\psi_\varepsilon(A)$ is a threshold on the elements of A. For any a in A:

$$\psi_\varepsilon(a) = \begin{cases} a - \varepsilon & \text{if } a > \varepsilon \\ a + \varepsilon & \text{if } a < -\varepsilon \\ 0 & \text{otherwise} \end{cases}$$

For an input matrix M, trade off parameter λ, and a tolerance t for the convergence (set to 10^{-7} in practice), the IALM is given by:

$$\begin{cases} \textbf{Initialization}: Y_0 = {}^{M}/_{J(M)}, L_0 = S_0 = [0], \mu_0 > 0, \rho > 1, k = 0 \\ \textbf{While } {}^{\|M\|_F}/_{\|M - L_k - S_k\|_F} > t \\ \text{Update L: } (\mathcal{U}, \mathcal{S}, \mathcal{V}) = SVD\left(M - S_k + {}^{1}/_{\mu_k} Y_k\right) \\ \qquad L_{k+1} = \mathcal{U}\, \psi_{1/\mu_k}(\mathcal{S}) \mathcal{V}^T \\ \text{Update S: } S_{k+1} = \psi_{\lambda/\mu_k}\left(M - L_{k+1} + {}^{1}/_{\mu_k} Y_k\right) \\ \text{Update Y: } Y_{k+1} = Y_k + \mu_k (M - L_{k+1} - S_{k+1}) \\ \textbf{End while loop}: k = k + 1 \\ \textbf{Return}: L_{k+1} \text{and } S_{k+1} \end{cases} \quad (4.2)$$

The additional parameter Y in (4.2) is the Lagrange multiplier used to account for the equality constrain in (4.1) in the optimization of L and S. An important feature of the IALM is that because of the threshold applied to the singular value matrix when updating L and S, only a limited number of singular values (and the corresponding singular vectors) need to be computed [106]. This alleviates the computational load in the algorithm. Partial SVD can be used to compute only the largest singular values [107].

4.3.1.2 Choosing λ in RPCA

The optimal setting of λ may depend on the application and the nature of the data. However Candès et al. suggested a value, independent of any prior knowledge on the data, that guarantees accurate recovery of the low rank component provided that it has been corrupted with randomly distributed perturbation [102]:

$$\lambda_0 = 1/\sqrt{\max(N_p, N_t)} \quad (4.3)$$

where N_p and N_t respectively represent the number of pixels in each frame and the number of time-frames in M. For practical images, this means:

$$\lambda_0 = 1/\sqrt{N_p} \quad (4.4)$$

4.3.1.3 Applications

RPCA is well suited to process video data where multiple time frames are strongly correlated. Applications include background modelling in video surveillance. In such a case RPCA treats smooth variations (e.g. related to illumination changes) as low rank while removing foreground moving objects that will occupy a fraction of the field of view in a limited number of frames and consequently appear in the sparse component (Figure 4.3). Peng et al. also proposed a modified version of RPCA incorporating an affine transformation model within IAML to remove image misalignments and further reduce the rank of the computed low rank component [108]. In terms of medical imaging, RPCA can be used to reconstruct under-sampled data sensing in order to accelerate dynamic MR data acquisition [109], [110].

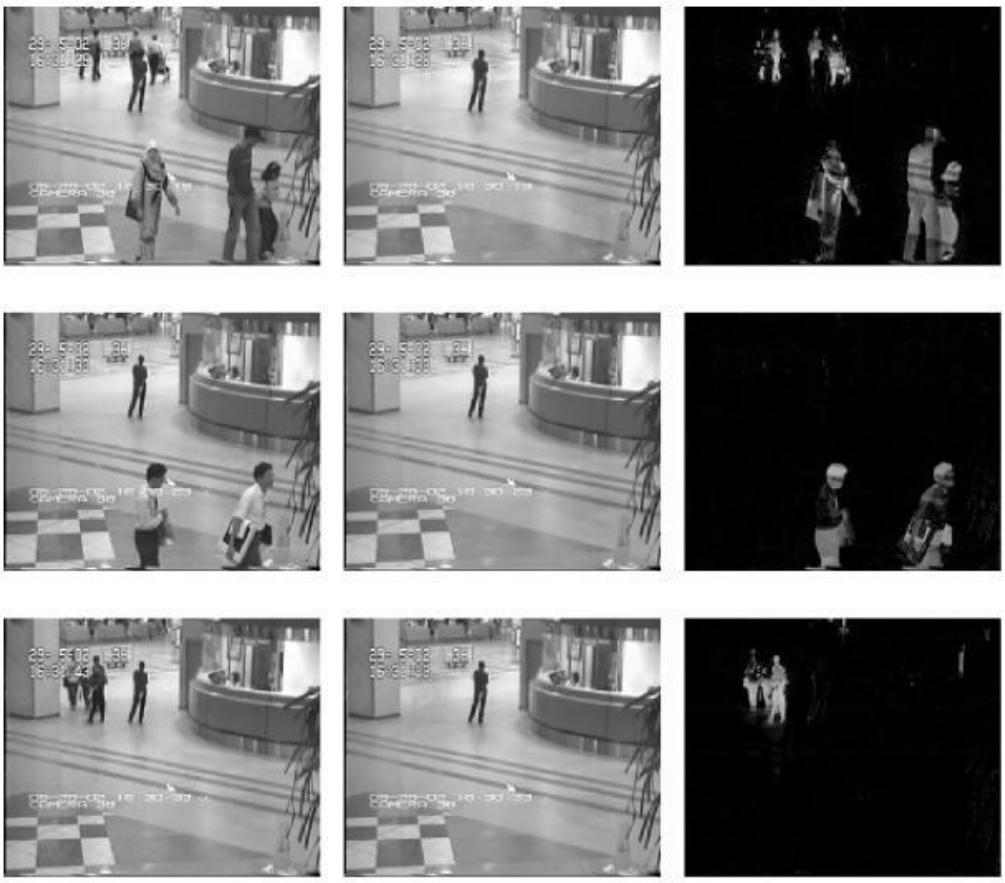

Figure 4.3: Application of RPCA to background modelling in video surveillance data (images taken from [102]).

Our application of RPCA aims to decompose a cine series into a low rank component (e.g. smooth and slowly varying changes affecting most of the field of view) and a sparse

component (e.g. rapid and local intensity changes). For DCE-MRI, we attribute the sparse component to local contrast changes and motion to the low rank. It should be noticed that due to the non-random nature of contrast enhancement, a different tuning of λ (compared to section 4.3.1.2) was required.

4.3.2 Principle of RDDR

The information in DCE-MR time-series can be regarded as a combination of motion related changes, and local changes caused by contrast enhancement. We hypothesize that RPCA makes it possible to correct for low rank motion elements via registration without confounds from contrast agent induced changes of intensity as shown in Figure 4.4.

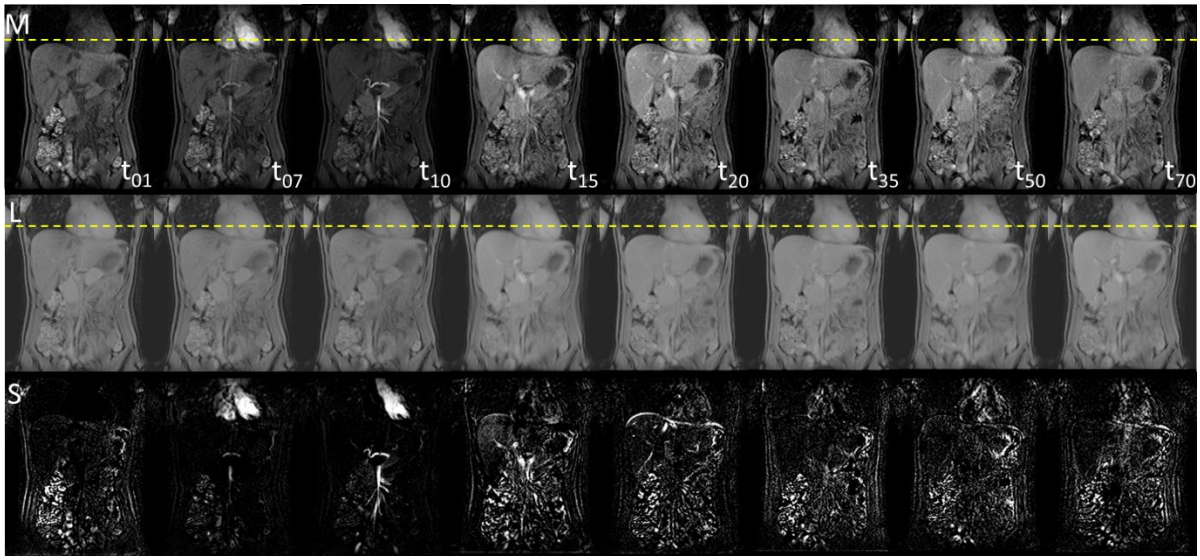

Figure 4.4: Decomposition of a DCE-MR time-series (multiple breath-holds) with RPCA for various time points. From top to bottom: original time-series (M) with frame indices; low rank component (L); sparse component (S). Changes due to contrast enhancement largely appear in S. Comparing the diaphragm position to the yellow dashed line indicates the motion present in L.

We consequently introduce a novel algorithm for DCE-MRI registration named Robust Data Decomposition Registration (RDDR) [82]. The process of RDDR can be described as follows: a given DCE time-series is reshaped as a (N_p by N_t) Casorati matrix and decomposed using RPCA with a starting value λ_{init} set to that given in (4.4) for the trade-off parameter. The time-frames from the resulting low-rank component are then registered, and the resulting deformation fields are applied to the original time-series so that a part of

the motion can be removed. The process is repeated for increasing values of the trade-off parameter over a fixed number of iterations, independent of the number of time-points in the dataset. This process is summarized in Figure 4.5. One should notice that deformation fields generated at each registration stage are not directly applied to images but added to a single global deformation field so that loss of information caused by multiple resampling is avoided. Since motion components and contrast changes cannot be perfectly separated with RPCA, an iterative approach is used. By using gradually increasing values of the trade-off parameter, it is possible to control the amount of motion included in the low-rank matrix.

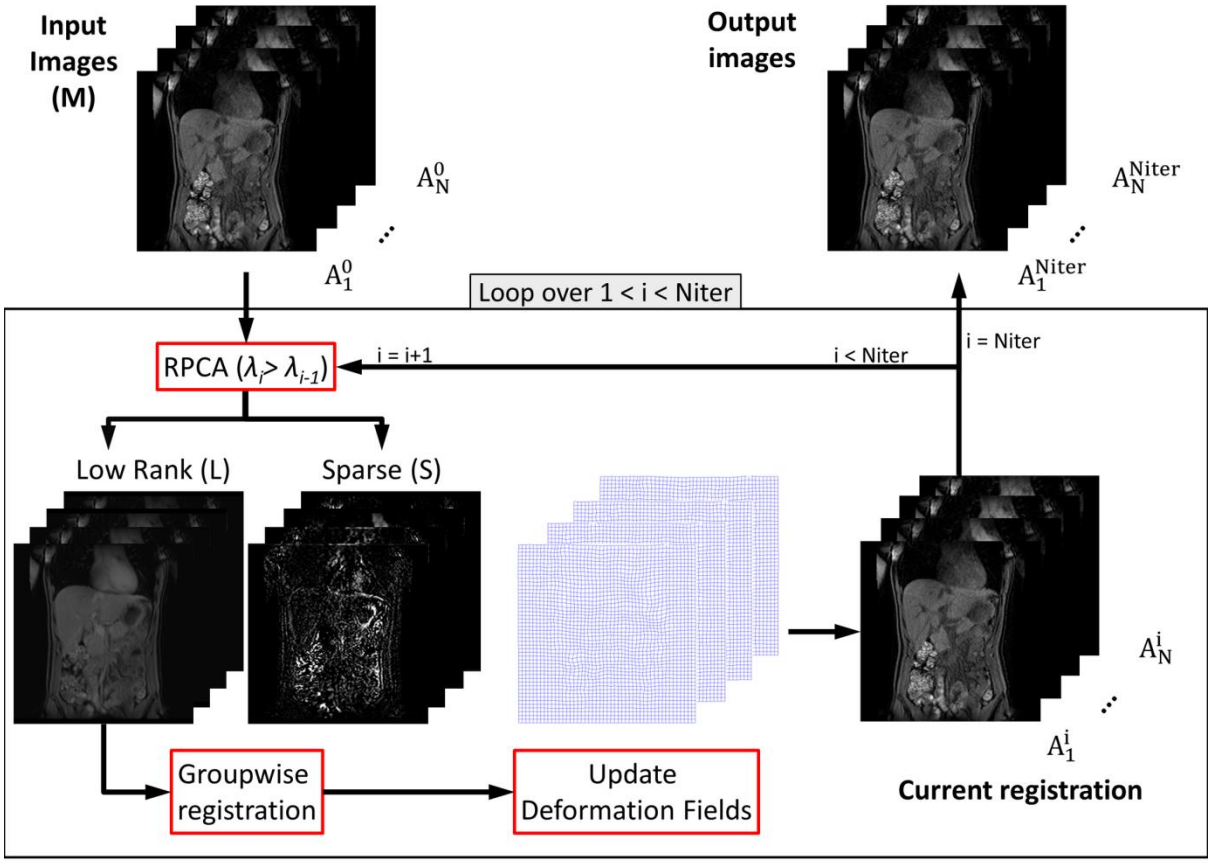

Figure 4.5: Diagram illustrating the process of RDDR (The parameter λ is gradually increased to let more information appear in the Low rank component over iterations).

4.3.3 Registration algorithm

In principle, any non-rigid registration technique could be used to register the low-rank frames and update the deformation field in Figure 4.5. However, the separation between

motion and contrast is not perfect in the decomposition and part of the changes due to contrast are likely to remain in the low rank matrix (e.g. slow washout process in healthy tissue) especially for higher values of λ. To account for such effects we chose a registration algorithm that is robust to intensity changes [103]. The similarity metric it utilizes, named residual complexity (RC), incorporates an intensity correction field that brings the source and the target images into agreement in the intensity space. RC favours the transformation that leads to the minimum complexity of the residual difference image. This is achieved by measuring the sparseness of the residual in terms of the discrete cosine transform (DCT) basis functions. The transformation model used is the b-spline based FFD [89] with a gradient descent optimization scheme.

Considering two (low-rank) time-frames L_{target} and L_{source} to be registered with the unknown transformation T_{FFD}, given the intensity correction field I_{corr} and the noise component η (both unknown). The following relationship can be written:

$$\mathrm{I_{target}} = \mathrm{I_{source}}(\mathrm{T_{FFD}}) + \mathrm{I_{corr}} + \eta \tag{4.5}$$

Registration can be achieved by minimizing the following objective function, E:

$$\mathrm{E}(\mathrm{I_{corr}}, \mathrm{T_{FFD}}) = \left\|\mathrm{I_{target}} - \mathrm{I_{source}}(\mathrm{T_{FFD}}) - \mathrm{I_{corr}}\right\|^2 + \beta\|\mathrm{PI_{corr}}\|^2 \tag{4.6}$$

The operator $||.||$ represents the Euclidean norm, and P and β respectively are the regularization operator and the regularization parameter. The form of P is chosen as the first order derivative regularizer. I_{corr} can be analytically solved by equating the derivative of the objective function to zero. If the identity matrix is denoted by Id and the residual image by r:

$$\begin{aligned} \mathrm{I_{corr}} &= (\mathrm{Id} + \beta\mathrm{P^TP})^{-1}\mathrm{r} \\ \mathrm{r} &= \mathrm{I_{target}} - \mathrm{I_{source}}(\mathrm{T_{FFD}}) \end{aligned} \tag{4.7}$$

By substituting this new expression in (4.6) and applying eigen-decomposition to P^TP, it yields:

$$\mathrm{E}(\mathrm{T_{FFD}}) = \mathrm{r^T}(\mathrm{Id} - (\mathrm{Id} + \beta\mathrm{P^TP})^{-1})\mathrm{r} \tag{4.8}$$

$$E(T_{FFD}) = r^T Q\, d\left(1 - \frac{1}{1+\beta\delta_i}\right) Q^T r = r^T Q\, \Delta Q^T r \quad (4.9)$$

$$E(\Delta, T_{FFD}) = (Q^T r)^T \Delta\, Q^T r \quad (4.10)$$

d() denotes a diagonal matrix and the δ_i's and Q respectively are the eigenvalues and the eigenvector matrix of P^TP. The objective function minimization is made possible by choosing a particular form for the eigenvectors Q and solving for the (diagonal) matrix Δ within the regularization.

An additional regularization term on Δ, R, is added to E to enforce the closeness of the source to the target image. A Kullback-Leibler based regularisation is chosen to favour a measure of information rather than a distance measure (associated with some function space) [35]. A trade-off parameter α is used to tune this additional regularization:

$$E(\Delta, T_{FFD}) = (Q^T r)^T \Delta\, Q^T r + \alpha R(\Delta) \quad (4.11)$$

By equating the derivative of (4.9) to zero it is possible to analytically solve for the elements of Δ and obtain the final expression for E after substitution:

$$E(T_{FFD}) = \sum_i \log(\,(q_i^T r)^2/\alpha + 1\,) \quad (4.12)$$

Given (4.10) the discrete cosine transform (DCT) basis function is chosen for the element of the eigenvector basis (i.e. the q_i's). Low complexity expressed in the DCT basis corresponds to a small number of non-zero coefficients representing r. The lower the number of non-zero elements the lower the complexity. RC is minimized when the residual image can be represented using the smallest possible number of function basis, corresponding to alignment of the input images.

4.3.4 Implementation details

The RPCA trade-off parameter λ affects the amount of information in the L and S components; Figure 4.6 shows the variation of the rank of L with λ for a small bowel DCE-MRI dataset with no registration applied. At each iteration of the RDDR algorithm, λ is increased from a starting value chosen to yield a rank of L equal to the number of frames

divided by four (with a tolerance of ± 10%). This starting value was chosen empirically as a value that provides some motion information in L, but keeps much of the contrast change in S. The maximum value of λ was selected based on 5 datasets, in such a way that the quantity of non-zero pixels in the RPCA sparse component remains above a threshold of 5%. This was found to be 2.5 times the starting value. Due to the approximately exponential curve shape seen in Figure 4.6, we increment λ logarithmically. We choose a number of iterations limited to 10 for the entire process. The same scheme for setting λ was used for all datasets presented in this chapter.

At each iteration, a groupwise multi-resolution registration is used. The target image is the mean of all the low-rank frames at the current resolution stage. This target is then updated using the current deformation when moving to a finer resolution. The FFD control point spacing was set to 4 pixels, 2 resolution levels (1/2 and 1) were used and the bending used as a regularizer of the deformation field energy [86] . As shown in Figure 4.6 some features present fuzzy contours for lower λ values, we consequently chose to use a high weight on the regularization (similar to [101]).

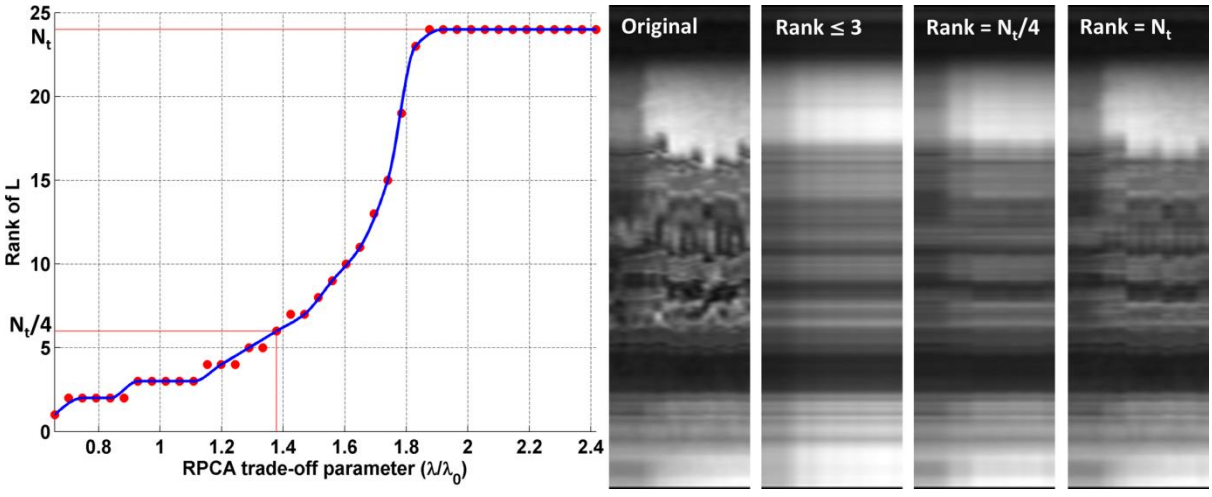

Figure 4.6: Rank of L as a function of the trade-off parameter for a small-bowel DCE-MRI data set (left). Temporal profiles (time cuts) of a single column of L through time for selected values of the rank to indicate the amount of information contained in L (right). λ_0 corresponds to the value in equation (4.4).

4.4 **Registration of DCE-MRI using RDDR**

4.4.1 Simulated data

The performance of RDDR was assessed using two types of simulations. In each case a ground truth motion was derived from volunteer scans and contrast enhancement simulated using literature pharmacokinetic parameters. In the first case, a gradient echo T1-weighted DCE protocol was used to acquire liver time series data during repeat breath-holds but without the injection of contrast (3s temporal resolution, coronal plane, 155s acquisition, 1.9x1.9x5 mm^3 voxels). In the second case, a balanced gradient echo series of the small bowel was acquired during free breathing in the coronal plane through the abdomen (1s temporal resolution, coronal plane, 52s acquisition, 1x1x5 mm^3 voxels). The frames were sequentially registered using FFD non-rigid registration with NMI as a similarity measure, a control point spacing of two pixels and three subdivision levels, to provide realistic deformations. In both cases, a single time-frame was extracted and manually segmented into: liver, bowel, right and left heart, aorta, portal vein. This segmentation was used as a map to simulate contrast enhancement using the modified Tofts model [22] and a population arterial input function [111]. T1 values were taken from [1] and pharmacokinetic parameters for each organ were chosen in agreement with a previous study [112]. The inverse ground truth transformation (computed by taking the opposite of each displacement vector) was then applied to the motion-free contrast enhanced time-series. Gaussian noise ($\sigma = 0.05$) and a local motion blurring (e.g. respiratory induced blurring, through plane motion) were added using image filtering to improve the realism of the data. Motion blurring was introduced by creating local point spread function filters convolved with some time frames. The entire process is summarized in Figure 4.7.

Registration of these simulations was performed using FFD registration (based on both NMI and RC similarity measures), PPCR and RDDR. The performance of each method

was assessed by computing the root mean squared error on the resulting displacement field.

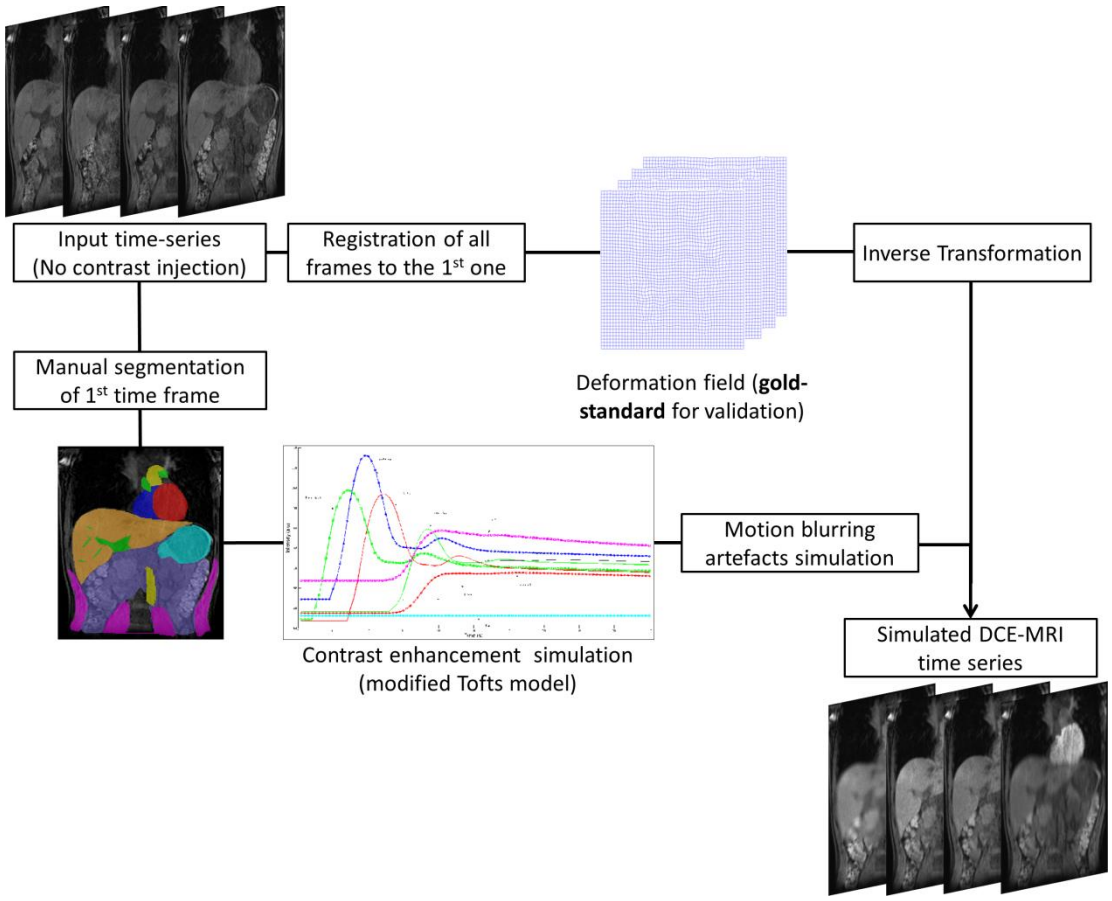

Figure 4.7: Different steps of the creation of a simulated DCE-MRI time series.

4.4.2 Clinical Data

Several kinds of DCE-MR datasets were acquired covering various temporal resolutions, breathing protocols and imaged organs. In total 7 liver time-series from both healthy volunteers and patients, 20 prostate time-series from patients diagnosed with cancer, 11 high temporal resolution and 19 lower resolution small bowel time-series from patients with Crohn's disease were registered. Details are summarised in Table 4.2. In all cases the acquisition started slightly before contrast agent injection. Subjects were imaged using T1-weighted gradient echo pulse sequences.

Breathing protocols were divided into three classes. First and most common is multiple breath-holds where subjects held their breath for a certain time then took a deep breath

and held again. Second is acquisition with a single breath-hold followed by shallow breathing where subjects initially held their breath for a comfortable period and could then breathe gently. Finally, free breathing acquisitions were also performed.

Acquisition Parameters/Data characteristics	Liver (breath-holds /shallow breathing)	Prostate (peristalsis)	Small Bowel (free breathing)	Small Bowel (breath-holds)
No. of time-frames	80 to 100	35	200	24
No. of slices	60	26	26	80
Field strength (T)	3	1.5	3	1.5
Repetition time (ms)	2.319	5.61	2.857	2.73
Echo time (ms)	1.058	2.5	1.8	0.9
Matrix	200 x 200	192 x 192	132 x 134	256 x 88
Slice thickness (mm)	5	3	5	3.5
Pixel spacing (mm)	1.87\1.87	0.67\0.67	1.78\1.78	1.95\1.95
Slice gap (mm)	2.5	0.4	2.5	0.4
Flip angle (deg)	10	15	15	15
Acquisition length (sec)	244.5	984.5	319	297.8
Imaging plane	coronal	axial	coronal	coronal
No of Subjects \ ROIs	7 \ 18	20 \ 26	11 \ 12	19 \ 25

Table 4.2: Details of dynamic MR data acquisition parameters and other characteristics

4.4.3 Evaluation of registration performance

For each dataset, registration was carried out using RDDR. For comparison, we chose a b-spline based FFD [89], and the PPCR algorithm as described in [99]. Sequential registration was chosen with FFD to minimize the effects of contrast changes. For improved clarity, only NMI was used as a similarity measure. This is because it is widely used in multi-modal registration and more generally accepted (compared to residual complexity). The assessment of registration accuracy was performed using three techniques:

- Qualitative assessment by generating time-cut images representing the temporal evolution of a pixel-wide line across all time-frames.
- Quantitative assessment based on manually adjusted ROIs corresponding to clinically relevant features (disease and normal tissue). These were contoured by radiologists or clinical experts on a single slice and then propagated across all the time frames using

the inverse deformation fields from registration. A pseudo ground truth (GT) was obtained by manually adjusting the position of the ROIs in every time frame to best follow the feature of interest. Time-intensity curves (TIC) were generated and the accuracy of registration was evaluated by computing the root-mean-squared error (RMSE) between TICs and corresponding GT TICs.

- Additionally, area under the time-intensity curves (AUC_{60}) for the first 60 seconds after the start of tissue enhancement were computed for each ROI. This commonly used semi-quantitative pharmacokinetic measurement [113] is used here to assess the early enhancement period when intensity changes are the most rapid. This has the advantage of avoiding any bias due to registration of washout frames which is less challenging.

FFD registration was carried out using a highly optimised C++ implementation [100] which was also use for the underlying registration within PPCR. Registration with RDDR was run using Matlab® (The Mathworks, Natick, MA). FFD registration was used with the same tuning as described in 4.3.4 with the bending energy regularization weight set to 0.01. The implementation of PPCR was the same as in [99]. Student's t-tests (using 10% significance level) were performed to compare the error distributions for unregistered and registered data.

4.4.4 Registration results

Overall registration showed an improved alignment with both PPCR and RDDR. For clinical data, results are presented separately for each type of imaged organ. For the different TIC examples, a heuristic model fit – based on a simple sigmoid function to mimic an uptake and a washout phase – [99] was used for visualization only. Error measurements were all computed using registered and GT normalized intensities. Normalization was carried out for the entire time-series so that all errors were scaled the same way.

4.4.4.1 Simulation

The results obtained after registration of the simulated DCE time-series are illustrated in Figure 4.8. Registration with FFD (using either NMI or RC as similarity measure) tends to incorrectly deform enhancing features such as the heart and aorta. Both PPCR and RDDR show a greater robustness to contrast changes. Figure 4.9 presents the RMSE obtain after registration of the different simulations. In all cases, both PPCR and RDDR lead to a significant reduction of error ($p < 0.01$). In the first type of simulation (liver, breath holds), the error after applying RDDR was significantly lower than after PPCR ($p < 0.001$). However, there was no significant difference between the performance of both techniques in the second type of simulation (small bowel, free breathing) ($p = 0.096$).

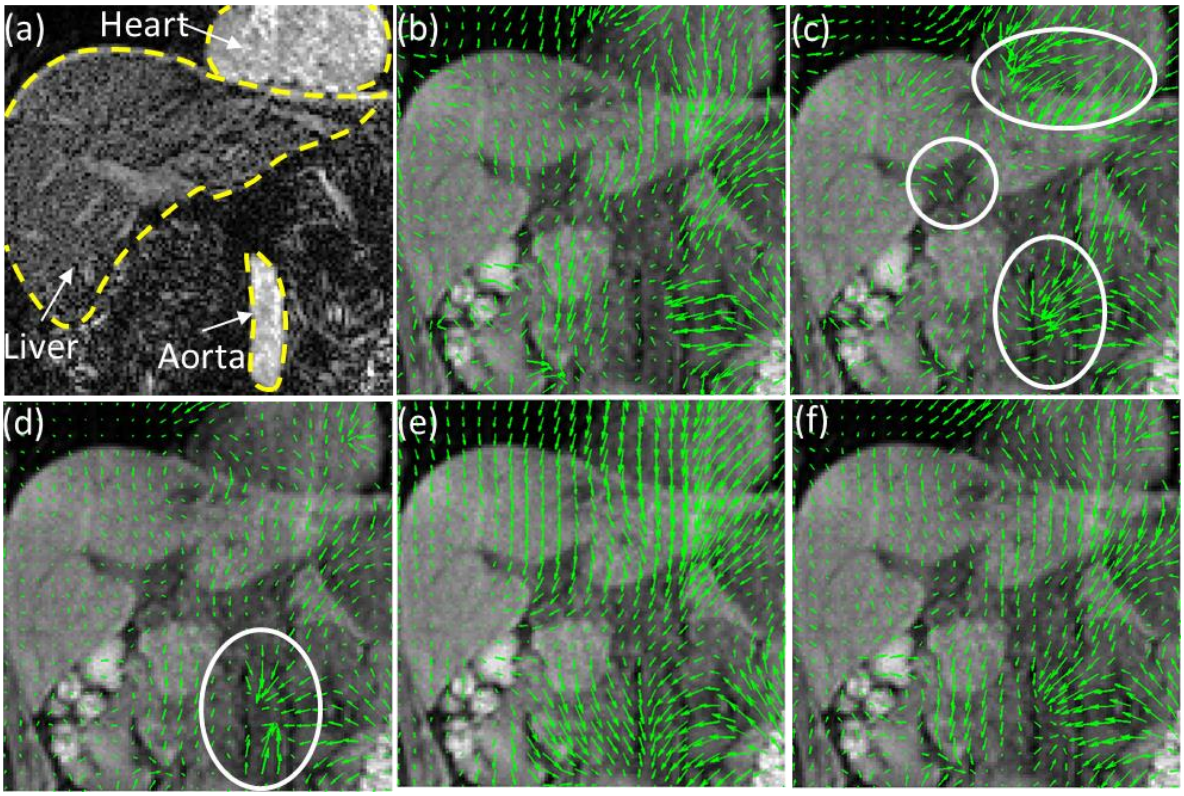

Figure 4.8: Simulation-based deformation analysis for a post-enhancement time-frame in the first simulated data set. The absolute difference image between the target and the current frame (a), and the ground truth deformation field overlaid on the target frame (b), show that changes are due to a mixture of motion and contrast enhancement. FFD registration based on NMI (c) and RC (d) present additional unphysical deformations (contoured in white) whereas PPCR (e) and RDDR (f) yield more realistic transformations.

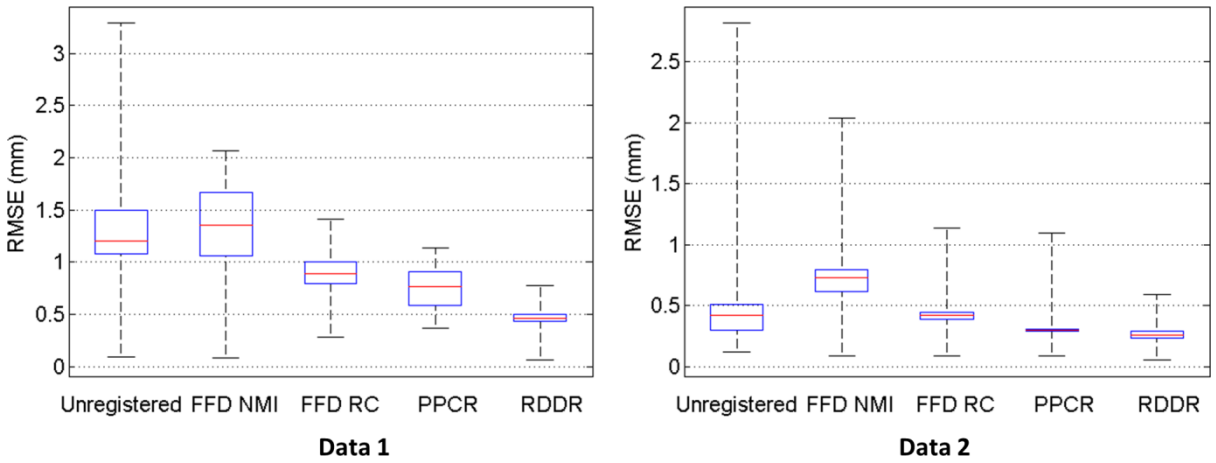

Figure 4.9: Registration error in the two types of simulation: liver imaging during multiple breath-holds (Data 1) and bowel imaging during free breathing (Data 2). Each plot shows: the median error (red line), the 25th and 75th percentile (blue box), and the full data extent (black dashed line).

4.4.4.2 Clinical Data

4.4.4.2.1 Liver

Liver DCE time-series were acquired using a multiple breath-hold protocol except one dataset for which a single breath-hold plus shallow breathing strategy was chosen. Misalignments in the covered fields of view were mainly caused by breathing. In some cases the diaphragm displacement amplitude was up to 75 mm in deep breathing between consecutive breath-holds.

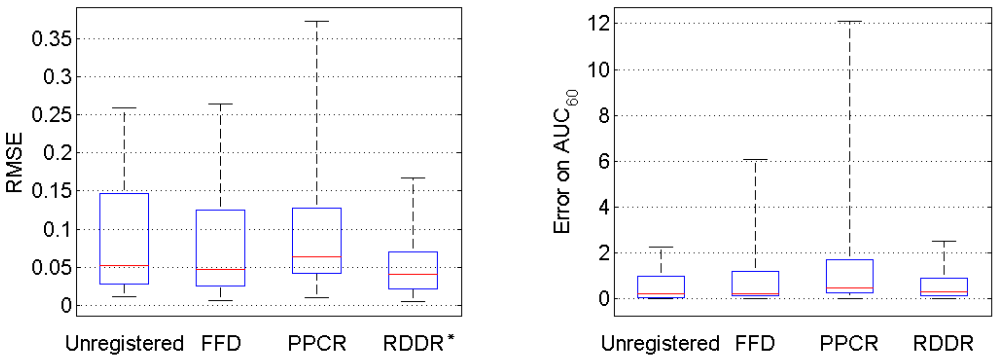

Figure 4.10: Registration results in liver data: RMSE in TICs (Left) and Error on AUC_{60} (right). Each plot shows: the median error (red line), the 25th and 75th percentile (blue box), and the full data extent (black dashed line). Significant difference compared to the unregistered case is indicated by '*'.

Three classes of ROIs were obtained for liver time-series: liver parenchyma, hepatic artery and portal vein. The performances of the different methods across all ROIs (21 in total)

regardless of the type of tissue are presented in Figure 4.10. Figure 4.11 shows an example of registration in a healthy volunteer. Misalignments were reduced by the three techniques. However residual displacements appear at early enhancement, and between breath-holds, after registration with FFD and PPCR. For the latter, such residual displacements appeared in two cases where magnitude of the motion between consecutive breath holds was particularly important.

RMSE with respect to the ground truth for each type of tissue are presented in Table 4.3. Registration with FFD resulted in an increase of error in some cases where important displacement occurred during breathing between breath holds. PPCR reduced the error in most cases. However in smaller ROIs (e.g. vessels) the improvement was limited compared to RDDR. Figure 4.11 (b, c, d, e) shows the comparison of the effect of the three techniques for an example hepatic artery ROI.

Despite the error decrease in TICs, the impact on the AUC_{60} error appeared to be limited in these data. However, RDDR lead to a decrease of the interquartile range compared to no registration. This effect was particularly strong for ROIs placed within hepatic arteries as these present a higher maximum enhancement.

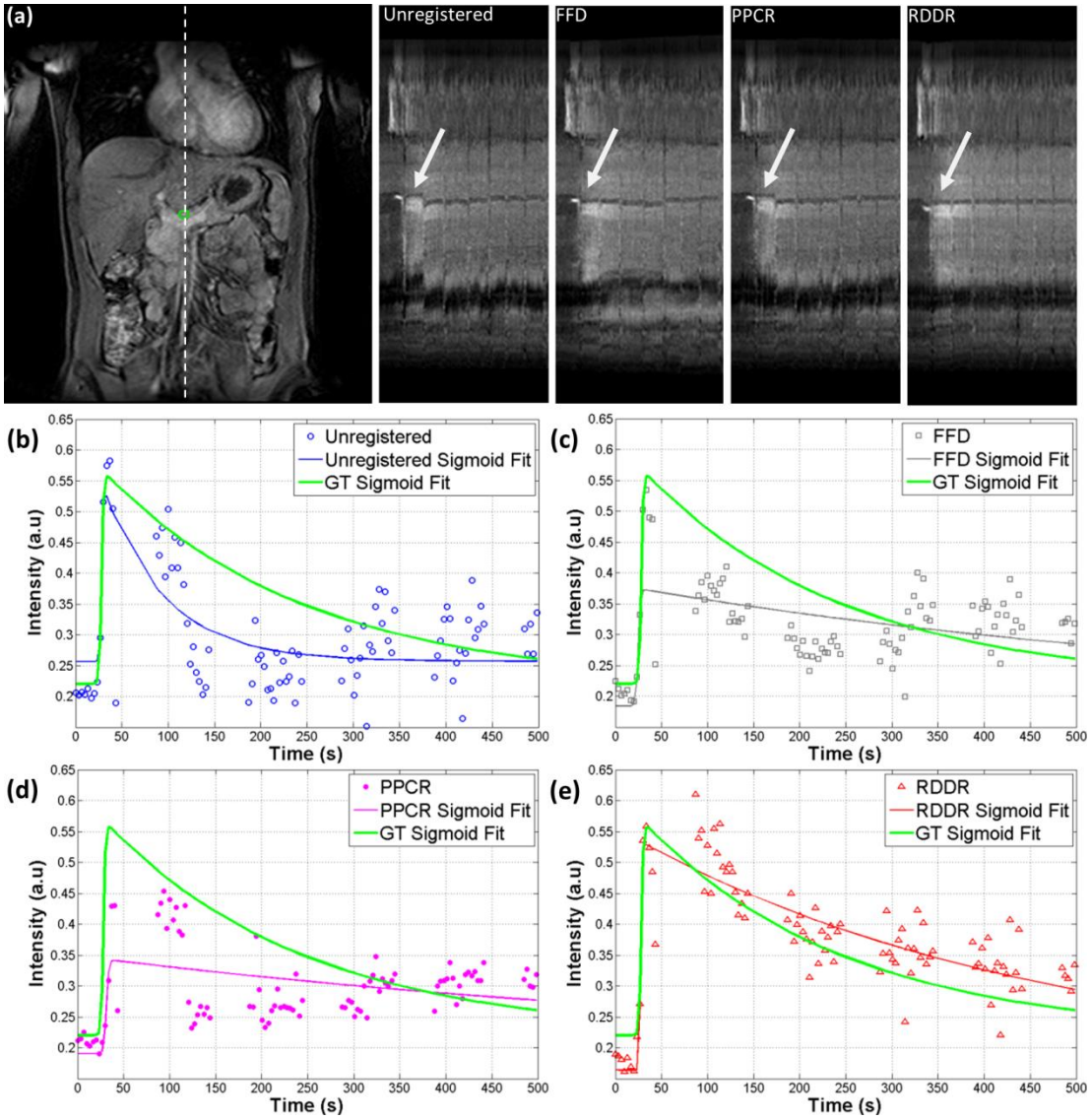

Figure 4.11: Effects of registration in a liver DCE time-series of a healthy volunteer, (a) coronal view for anatomical reference with the hepatic artery contoured in green, a dashed line indicates the location of the time-cuts for unregistered, FFD, PPCR and RDDR. Arrows indicate the location of the ROI. TICs for unregistered (b), FFD (c), PPCR (d) and RDDR (e) are also presented. The same sigmoid fit to the ground truth (GT) data is presented on all graphs for visualization purposes only. Here RMSE were (0.21/0.25/0.36/0.14) and AUC60 errors were (2.5/6.1/12.1/2.4) for Unregistered/FFD/PPCR/RDDR respectively.

4.4.4.2.2 Small bowel DCE (free breathing)

Free breathing small bowel DCE time-series were acquired after injection of butylscopolamine (Buscopan, Boehringer, Germany) to slow down peristalsis. The remaining motion was mainly due to breathing and displacements of the bowel walls were found to be as large as 17.8 mm. The wall of the small bowel is thin and such displacement amplitudes are likely to yield large errors in the monitoring of contrast enhancement.

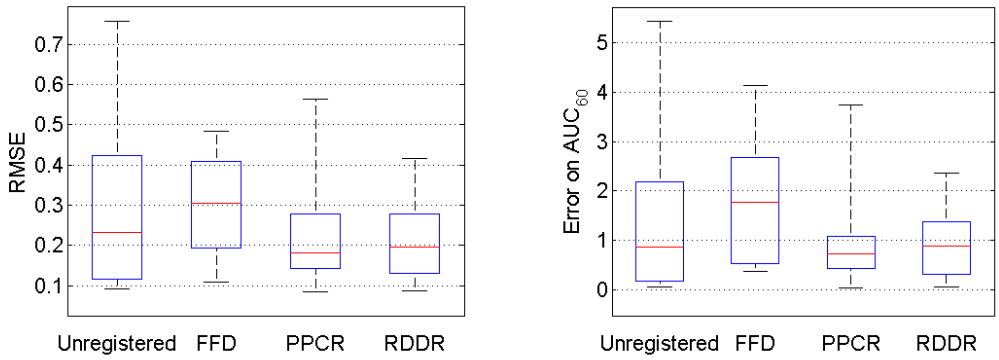

Figure 4.12: Registration results in free breathing bowel data: RMSE in TICs (Left) and Error on AUC60 (right). Each plot shows: the median error (red line), the 25th and 75th percentile (blue box), and the full data extent (black dashed line). Significant difference compared to the unregistered case is indicated by '*'.

In some cases FFD introduced additional unlikely deformations (see Figure 4.12 and Figure 4.13). Misalignments due to breathing were reduced by both PPCR and RDDR.

The action of butylscopolamine was found to be limited in 4 of the 11 datasets. In these cases residual through plane motion caused the ROIs (especially normal tissue) not to appear in some time-points making the assessment of registration accuracy difficult. Thus these cases were excluded from validation. Analysis of the remaining 12 ROIs showed a reduction of error in registered time-series for both PPCR and RDDR (see Figure 4.12). ROIs were small and located within bowel walls thus slight misalignments could cause large changes in RMSE. Two types of ROI corresponding to normal tissue and disease were contoured in these time series. The interquartile range was lower with PPCR in the disease ROI (see Table 4.3), although median errors were similar for PPCR and RDDR

Similarly, the AUC_{60} errors were generally lower after PPCR compared to RDDR results (see Figure 4.12).

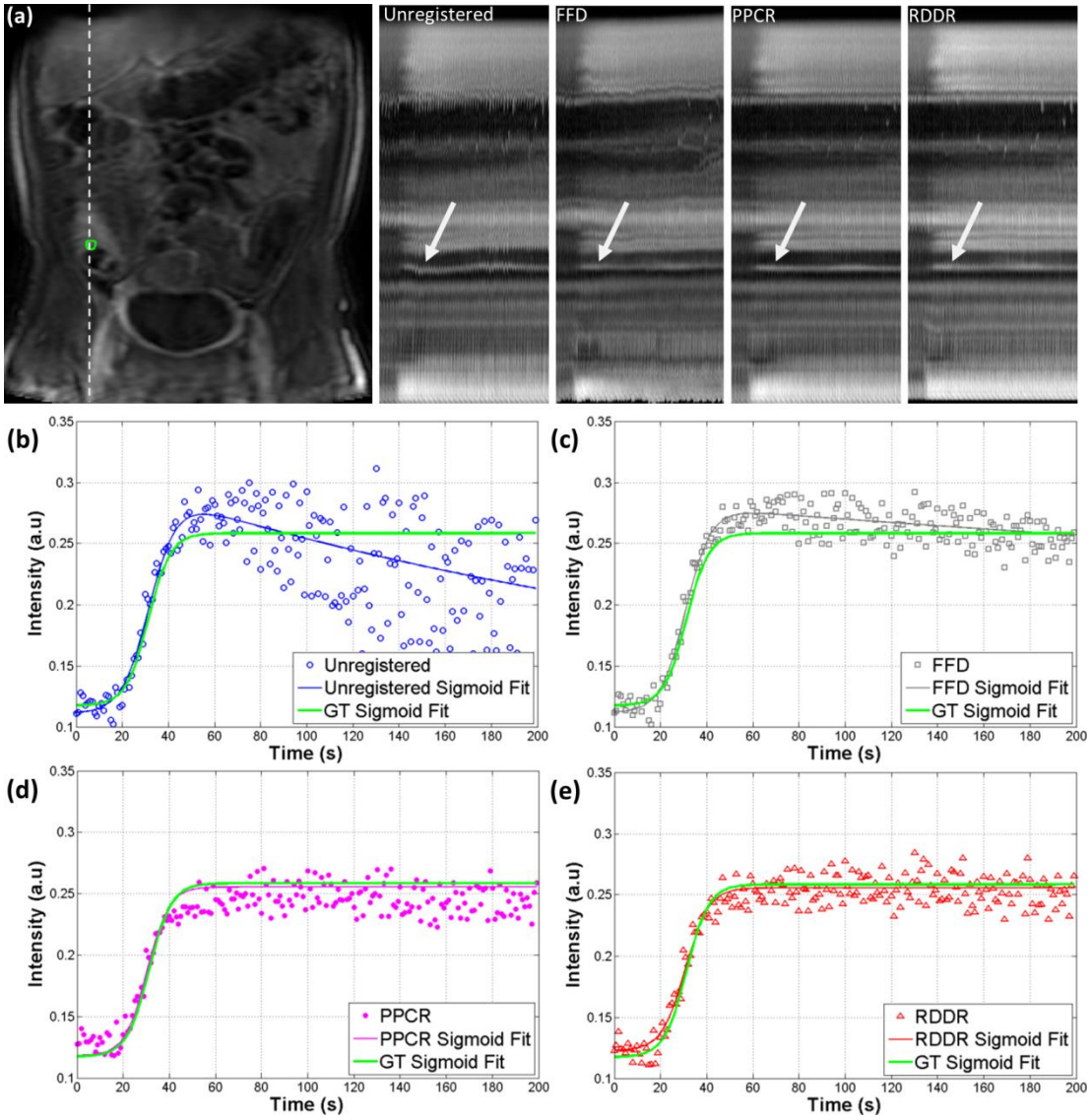

Figure 4.13: Effect of registration in a free breathing small bowel DCE time-series of a patient with Crohn's disease, (a) coronal view for anatomical reference along with time-cuts for unregistered, FFD, PPCR and RDDR. A disease ROI is contoured in green and a dashed line indicates the location of the time-cuts. Arrows indicate the location of the ROI. TICs for unregistered (b), FFD (c), PPCR (d) and RDDR (e) − The GT sigmoid fit is for visualization purposes only. Here RMSE were (0.46/0.40/0.20/0.28) and AUC_{60} errors were (2.4/2.8/0.22/1.5) for Unregistered/FFD/PPCR/RDDR respectively.

4.4.4.2.3 Small Bowel DCE (Multiple Breath-holds)

Butylscopolamine was also injected in these patients before acquisition of a repeat breath-hold small bowel DCE time series. The misalignments of time frames were caused by breathing and the non-repeatability of breath-holds and were found to be as large as 23.4 mm in the studied area. As previously, two of the 19 datasets were excluded from the ROI analysis due to anatomy moving out of slice.

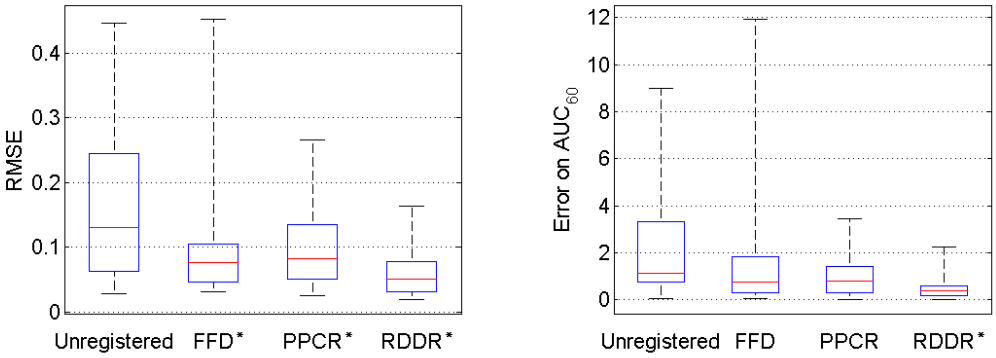

Figure 4.14: Registration results in multiple breath holds bowel data: RMSE in TICs (Left) and Error on AUC_{60} (right). Each plot shows: the median error (red line), the 25th and 75th percentile (blue box), and the full data extent (black dashed line). Significant difference compared to the unregistered case is indicated by '*'.

Analysis of the 28 available ROIs showed a decrease of RMSE with respect to GT with the three techniques (see Figure 4.14). However FFD increased the error in one case. ROI types corresponded to normal tissue and disease: across all datasets RDDR presented the best improvement for both types of tissue (see Table 4.3). The effect on the error in AUC_{60} was similar. Figure 4.15 illustrates the effect of registration in these time-series.

4.4.4.2.4 Prostate

The nature of motion in prostate DCE time-series was very different compared to the other types of data used in this study. Across the 20 available datasets, 11 presented misalignments due to the presence of gas in the rectum or contraction of surrounding muscles. Although the amplitude of motion was limited, it was found to be as large 12.4 mm for the prostate apex in some cases. ROIs in prostate tumours are small and even limited motion can cause important changes in TICs (see Figure 4.16) hence the potential importance of registration in such data.

TIC shapes after registration were in improved agreement with GT with the three techniques (see Figure 4.17). ROIs in the prostate were divided into two classes: tumour and normal tissue. Although both PPCR and RDDR performed equally in tumours, PPCR increased the error in some normal ROIs. Figure 4.17 shows an example of motion in the prostate and the effects of registration in a cancer ROI. Across all ROIs, the error in AUC_{60} was increased by PPCR whilst FFD and RDDR generally decreased the error.

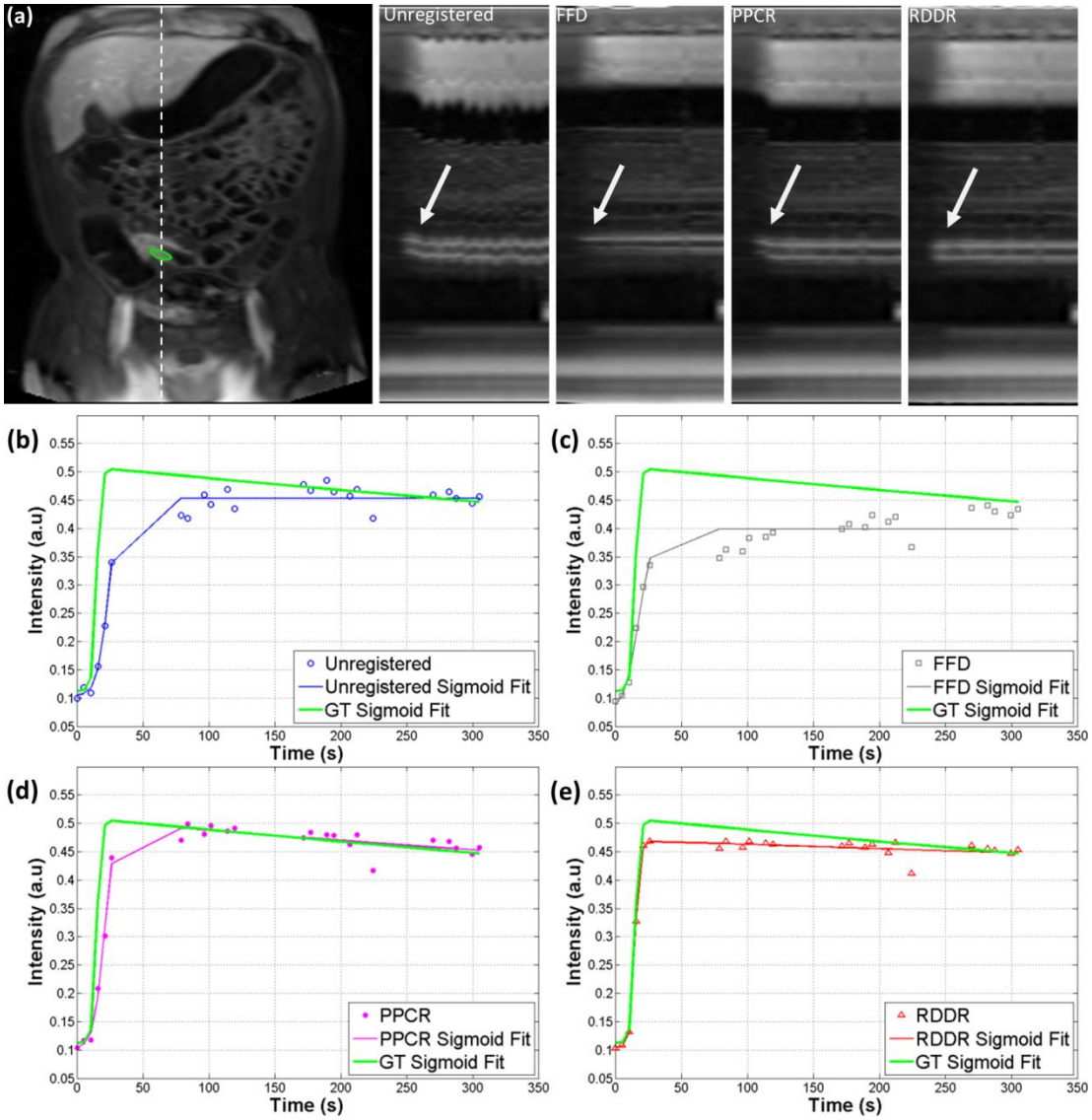

Figure 4.15: Effect of registration in a small bowel DCE time-series (multiple breath-holds) of a patient with Crohn's disease, (a) coronal view for anatomical reference with a disease ROI contoured in green, a dashed line indicates the location of the time-cuts for unregistered, FFD, PPCR and RDDR. Arrows indicate the location of the ROI. TICs for unregistered (b), FFD (c), PPCR (d) and RDDR (e) − The GT sigmoid fit is for visualization purposes only. Here RMSE were (0.40/0.45/0.26/0.1) and AUC_{60} errors were (9.0/10.7/3.9/2.0) for Unregistered/FFD/PPCR/RDDR respectively.

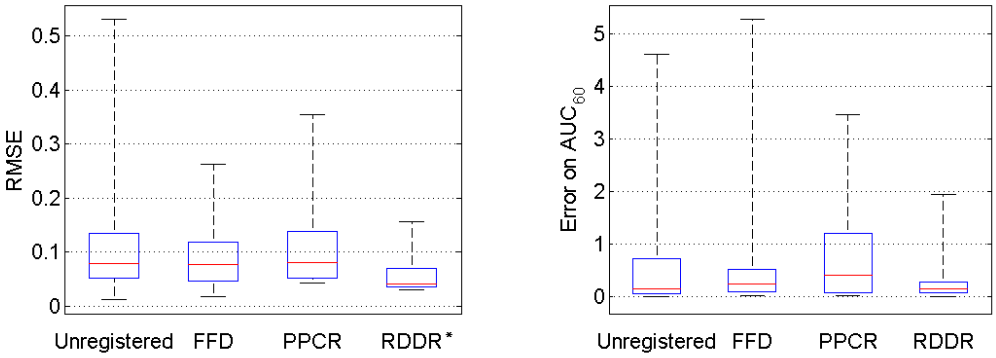

Figure 4.16: Effect. Registration results in prostate data: RMSE in TICs (Left) and Error on AUC_{60} (right). Each plot shows: the median error (red line), the 25th and 75th percentile (blue box), and the full data extent (black dashed line). Significant difference compared to the unregistered case is indicated by '*'.

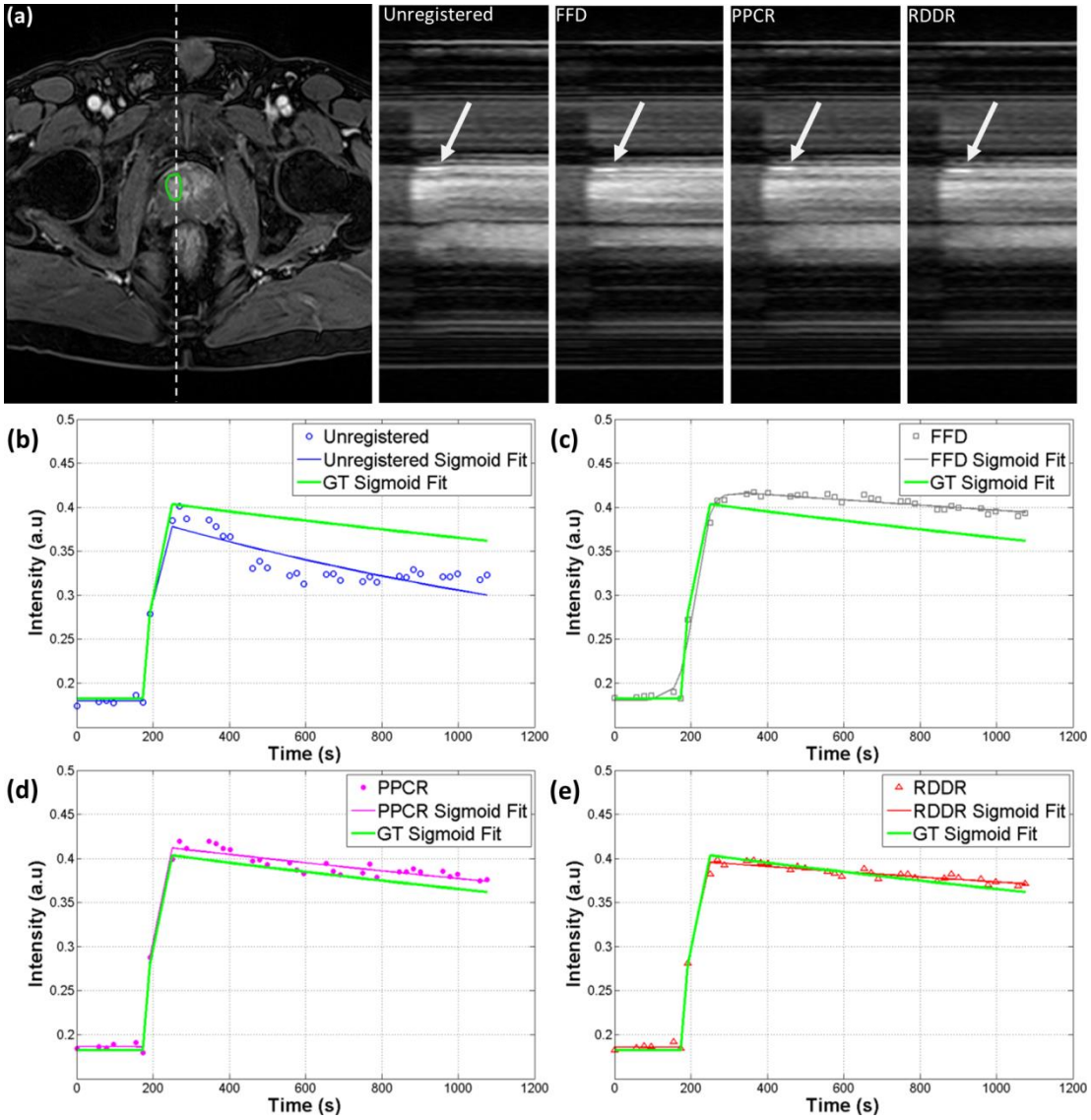

Figure 4.17: Effects of registration in a prostate DCE time-series of a patient with cancer, (a) axial view for anatomical reference with a cancer ROI contoured in green, a dashed line indicates the location of the time-cuts for unregistered, FFD, PPCR and RDDR. Arrows indicate the location of the ROI. TICs for unregistered (b), FFD (c), PPCR (d) and RDDR (e) − GT sigmoid fit is for visualization purposes only. Here RMSE were (0.25/0.13/0.06/0.04) and AUC_{60} errors were (0.21/0.52/0.56/0.16) for Unregistered/FFD/PPCR/RDDR respectively.

Imaged organ	Registration	Error with respect to GT (RMSE on intensities)		
Liver	ROI type	Hepatic Artery	Portal Vein	Liver Parenchyma
	Unregistered	0.18 (0.079)	0.05 (**0.032**)	0.28 (0.401)
	FFD	0.19 (0.180)	0.07 (0.058)	0.25 (0.221)
	PPCR	0.10 (0.109)	0.09 (0.122)	0.23 (0.276)
	RDDR	**0.09 (0.079)**	**0.04** (0.034)	**0.23 (0.085)**
Small Bowel (Free Breathing)	ROI type	Disease ROI		Normal ROI
	Unregistered	**0.11** (0.186)		0.28 (0.313)
	FFD	0.25 (0.186)		0.31 (0.276)
	PPCR	0.14 (**0.075**)		0.26 (0.198)
	RDDR	0.14 (0.146)		**0.23 (0.085)**
Small Bowel (Breath holds)	ROI type	Disease ROI		Normal ROI
	Unregistered	0.16 (0.283)		0.10 (0.124)
	FFD	0.09 (0.084)		0.05 (0.059)
	PPCR	0.10 (0.073)		0.06 (0.082)
	RDDR	**0.06 (0.063)**		**0.04 (0.022)**
Prostate	ROI type	Cancer		Normal ROI
	Unregistered	0.08 (0.056)		0.08 (0.106)
	FFD	0.08 (0.039)		0.05(0.091)
	PPCR	0.07 (0.039)		0.13 (0.123)
	RDDR	**0.04 (0.031)**		**0.04 (0.035)**

Table 4.3: Registration performance assessment: RMSE with respect to the ground truth for all tissue types in various clinical data sets. Results are presented as *median value (interquartile range)*. The best value is shown in bold for each type of ROI. Over all RDDR produces the lowest errors.

4.5 Discussion

This chapter presents a new iterative registration approach and its use to address the challenge of DCE-MRI registration. The iterative data decomposition within RDDR gives better control on the computation of the deformation field compared to a more direct registration scheme (e.g. single target, sequential registration). RDDR performance was compared to that of a popular NMI based FFD registration and to PPCR [98]. An alternative Independent components analysis based registration [101] has been applied to myocardial perfusion data acquired during free breathing, further work would be necessary to compare it to RDDR in a wider selection of anatomical features. Both methods use data decomposition to limit the effect of contrast enhancement on the modelling of deformations. However, independent component analysis necessitates suitable component identification while RPCA provides a general model for data decomposition.

RDDR uses an iterative approach to gradually correct for motion elements. In that sense it has similarities with PPCR where the amount of information used to generate a set of synthetic target images is progressively increased at every iteration [98]. However important methodical differences between the two techniques lie in the fact that the decomposition output of RPCA is not used as a target but registered in a group wise manner in RDDR. Also PPCR is based on principal component analysis which is a general model for variance separable data without the explicit identification of a sparse component. This is different from RPCA and can produce very different decomposition depending on the nature of the data (e.g. type of breathing).

In this work we kept the control point spacing and transformation model the same for all methods. However the techniques inherently use different approaches to choose the target image (e.g. groupwise, sequential, synthetic target generation). The relative benefits of each approach could be the subject of further investigation.

Results from simulated DCE-MRI data registration show that RDDR can compensate for important misalignments due to multiple breath-holds, as well as pseudo periodic motion due to free breathing, without impacting enhancing regions.

Registration with RDDR is more accurate in most cases where there was a preference (see Figures 4.10, 4.14 and 4.16). Moreover the reduced error with respect to the ground truth time intensity profiles suggests that RDDR could allow a better discrimination between different types of tissue (e.g. normal, disease, arteries and veins). In particular the assessment of registration accuracy for early tissue enhancement (AUC_{60}) showed that RDDR provides a robust correction in the presence of rapid and intense contrast changes. Such a measurement is particularly useful as it provides information on the accuracy of registration at early enhancement when contrast changes are the most important. This can be of particular interest when modelling the rapid contrast arrival of the arterial arrival phase to extract pharmacokinetic parameters describing the rate of contrast agent exchange, linked to tissue permeability. This period is important for distinguishing malignancy [113]. Most registration techniques are likely to produce accurate correction

during the washout phase since contrast agent is now dispersed and the contrast change is slowly varying. However, unrealistic deformations can appear in time-points corresponding to maximum enhancement when intensity changes are rapid. This was observed in the simulated data with FFD based on residual complexity minimization. In this context, RDDR features a degree of robustness to various shape of enhancement: for peaky TICs, rapid changes will be treated as part of the sparse component and will not hinder registration. On the contrary, slow uptakes that might be put in the low rank component should not cause unrealistic distortion due to the use of registration based on RC minimization.

Interestingly, PPCR performed well in small bowel data acquired during free breathing which differs from findings in simulation. This might be explained by the long acquisition time with a high temporal resolution that can catch irregularities in breathing and thus cyclic respiratory motion does not appear in the first PCA components. Also fairly slow and limited contrast changes in the field of view (e.g. no major arteries, heart etc.) might increase their appearance in the first principal components

One should note that AUC_{60} is usually measured on contrast agent concentration curves in DCE-MRI analysis [113]. Here measurements were performed directly on the pixels' TIC. The relationship between intensity and contrast agent concentration is not linear (see section 2.4.2.2), although it can be approximated as such over a narrow range of tissue T1 values. However it seems reasonable to expect that a more accurate TIC after registration would result in an improved monitoring of the concentration for a given pixel.

The work presented here focussed on the effects of registration upon the time intensity curves. More accurate curves produced by successful image registration should lead to more accurate contrast agent concentration estimation over time.

Additionally no fitting error was used to assess the performance of the different algorithms. This is because such a measurement might be misleading outside of its context: a very low fitting error does not necessarily correspond to an improvement if the shape of the curve is significantly different from that of the ground truth (see Figure 4.11 c and d), since it incorporates measurement of the model fit bias [114].

The work presented in this chapter deals only with 2D image series, but a 3D version of RDDR has also been developed. The extension is indeed relatively straightforward: in the data reshaping prior to RPCA, each 3D volume converted into a single column. Also, 3D FFD registration is available.

In terms of computational time, 256x256x20 pixels time-points datasets could be registered in less than 10 minutes on an Intel Xeon CPU 3GHz Windows machine with 32 GB RAM.

4.5.1 RPCA Parameterization

Candès et al. [102] provided a model-free value for the trade-off parameter in RPCA. The scheme proposed in this study to adjust this trade-off parameter was set experimentally so that enough motion is incorporated into the low rank component when initiating the registration process, whilst little contrast change appears. Future work might include investigation of an optimal value for DCE-MR time-series decompositions, or the inclusion of prior knowledge of contrast changes (e.g. general curve shapes) as a constraint in RPCA in addition to that on the rank of L and the sparsity of S. Additionally model selection theory could be applied to investigate a better tuning for data decomposition.

4.5.2 Breathing Protocols

The choice of breathing strategy has a major influence on the efficiency of motion correction in DCE-MRI. Multiple breath-holds during continuous acquisition result in “gasp” images when the subject takes a breath [101]. Gasps contain blurring artefacts that may complicate registration. The robustness of RDDR in such cases stems from the gasps appearing in the sparse component.

Free-breathing acquisition allows more continuous monitoring of tissue enhancement but is also subject to intra-frame blurring artefacts [1]. Moreover if high temporal resolution is favoured over spatial resolution, features can be less well defined. However, the periodic and continuous changes related to breathing tend to reinforce the low rank characteristics

of motion, leading to a robust separation from the contrast changes in the sparse component of RPCA.

A single breath-hold followed by shallow free breathing is adopted in some protocols. Early time-frames present limited misalignments which reduces the risk of error in the important uptake phase.

4.5.3 Motion separation

RDDR uses a separation of data into low-rank and sparse components. In some DCE cases, bowel peristaltic motion not stopped by butylscopolamine was observed in the sparse component and was thus not removed by the registration steps. Whilst undesirable for DCE analysis, this limitation can be exploited in non-contrast enhanced studies of small bowel motility where a separation of bowel motility from respiration is desirable (see chapter 5).

More generally, the hypothesis that all motion should appear in RPCA low rank component may be limiting, in particular when some motion elements occur locally over a short period of time such as in peristalsis. Importantly, this is violated if respiration is quick and erratic while contrast enhancement comes fast and is followed by very slow washout. This was observed when applying RDDR to cardiac perfusion imaging data.

The way the information is processed in RDDR can be seen as a multi-scale registration in terms of motion: the higher the value of the trade-off parameter the bigger the amount of motion appearing in the low-rank component. In other words RDDR can correct different components of motion along an iterative process.

4.6 **Conclusion**

The introduced method allows improved registration of multiple breath-hold and free breathing DCE-MR time-series. It relies on robust decomposition of input data that separates motion from contrast enhancement and is therefore termed robust data

decomposition registration (RDDR). It has been successfully applied to images of multiple organs (liver, small bowel and prostate) affected by different types of motion and compares favourably to existing state-of-the-art techniques. The novelty of RDDR resides in its robustness to contrast enhancement in tissue, particularly during initial tissue uptake.

This technique is not limited to registration of DCE-MRI and could also be applied to other imaging technique based on MRI such as DSC-MRI and ASL, or to other modalities such as Positron Emission Tomography or contrast enhanced CT

5 Application of RDDR to Dynamic Imaging of the Small Bowel

5.1 Introduction

This chapter describes an alternative application of RDDR to respiratory motion correction in the context of bowel motility quantification in data acquired during free breathing. The first section introduces the challenges related to MRI based bowel motility analysis and existing quantification techniques. This is followed by the description of RDDR developments in order to adapt it to the present case and its application to a cohort of 20 healthy subjects.

An early version of this work, introducing the principle of the new application has been published in Lecture Notes in Computer Science (proceedings of the MICCAI conference 2013) [115]. The complete version of the study has been submitted to Physics in Medicine and Biology, this also includes the successful processing of colon images from 6 subjects with no further modifications of the algorithm or additional tuning. This method has also been accepted for presentations at ISMRM 2014, including description of its application to small bowel [116] and colon [117] imaging.

5.2 Dynamic imaging of the small bowel

5.2.1 Small bowel motility

As introduced in section 2.5. motion in the bowel can be represented as the association of complex mechanisms including slow waves along the gastro intestinal tract, referred to as peristalsis, and radial contractions [33], [34]. Repeat 2D imaging of the bowel region using high temporal resolution makes the analysis of peristalsis possible.

5.2.2 Motility quantification

Motility measurements can be carried out using subjective qualitative assessment based on visual inspection by reporting radiologists [35], [118]. Alternatively it can be quantified automatically using generalized optical flow registration (OF) [34]. This technique uses a joint non-rigid transformation (multi-resolution) and modelling of intensity changes within a time-series. An additional intensity correction map is included in the algorithm's cost function to account for intensity changes related to through-plane motion and flow of intra luminal content. The cost function is formulated as follows:

$$\mathrm{C}(\mathrm{u_x}, \mathrm{u_y}, \mathrm{I_{map}}) = \left\| \mathrm{I_{src}}\left(\mathrm{T_{u_x,u_y}}\right) + \mathrm{I_{map}} - \mathrm{I_{trg}} \right\|^2 + \mathrm{R}(\mathrm{u_x}, \mathrm{u_y}, \mathrm{I_{map}}) \tag{5.1}$$

$\mathrm{I_{src}}$ and $\mathrm{I_{trg}}$ respectively denote the reference and the source images for registration, $\mathrm{I_{map}}$ is the intensity correction field and $\mathrm{T_{u_x,u_y}}$ is the displacement field in the two directions of the 2D image space represented by the vectors $\mathrm{u_x}$and $\mathrm{u_y}$. An additional regularization parameter R is added to enforce spatial smoothness on $\mathrm{u_x}$ and $\mathrm{u_y}$ based on their second order derivatives. Gauss-Newton optimisation is chosen to iteratively minimize the cost function. A dense representation of the 2D deformations (i.e. a displacement field at the pixel resolution) is computed to account for local motion. This model has a higher spatial resolution than control point grid based deformation and can capture local deformations caused by peristalsis although it is computationally more complex.

Quantitative assessment of motility can be computed from the Jacobian determinants of the displacement fields obtained after registration with OF. This metric provides information on local expansion or compression of features. It is defined by:

$$\mathrm{J}(\mathrm{x}, \mathrm{y}, \mathrm{t}) = \left| \det \begin{pmatrix} \frac{\partial \varphi_\mathrm{x}}{\partial \mathrm{x}}(\mathrm{x}, \mathrm{y}, \mathrm{t}) & \frac{\partial \varphi_\mathrm{x}}{\partial \mathrm{y}}(\mathrm{x}, \mathrm{y}, \mathrm{t}) \\ \frac{\partial \varphi_\mathrm{y}}{\partial \mathrm{x}}(\mathrm{x}, \mathrm{y}, \mathrm{t}) & \frac{\partial \varphi_\mathrm{y}}{\partial \mathrm{y}}(\mathrm{x}, \mathrm{y}, \mathrm{t}) \end{pmatrix} \right| \tag{5.2}$$

where,

$$\varphi_x(x, y, t) = x + u_x(x, y, t)$$
$$\varphi_y(x, y, t) = y + u_y(x, y, t) \quad (5.3)$$

φ_x and φ_y define the spatial transformation and a given time t. For a time series containing N frames, the standard deviation of the Jacobian determinant through time provides a measure of variation of local bowel contraction and expansion at each pixel:

$$\sigma_J(x, y) = \sigma(\{J(x, y, t)\}_{t=[0,N]}) \quad (5.4)$$

Such a measure is insensitive to rigid transformations (e.g. translation) [34]. However the non-rigid deformations related to respiration, if not corrected for, have an effect on the measurements. Thus the principal limitation for this technique is the requirement to remove or reduce respiratory motion by using breath-hold acquisition protocols. This limits the utility for important groups of pathological conditions where aberrant small bowel motility patterns take place over time periods greater than a breath-hold duration.

5.2.3 Extension to free breathing

The purpose of this study is to apply RDDR to filter out respiratory motion from a free breathing dataset, allowing subsequent quantification of small bowel motility with OF. Similar to DCE-MRI registration, the idea is to use RDDR to gradually correct for respiratory motion without affecting useful information on motility. An ability to accurately quantify bowel motility continuously over several minutes without the interruption caused by repeated breath holds would be a significant advance and open the technique to a broader range of diseases of the small bowel and colon [119]–[122]. The novel post-processing pathway introduced in this chapter to correct respiratory motion and then quantify bowel motility in free-breathing cine MRI data sets is referred to as dual registration of abdominal motion (DRAM).

5.3 **Dual Registration of Abdominal Motion**

5.3.1 RDDR modifications

The Application of RDDR to dynamic images of the bowel consists of separating respiratory motion effects from peristaltic motion. This is quite different from the initial application to DCE-MRI data. Thus, an adjustment is required. In particular, as the two elements are motion mechanisms, care must be taken not to remove any information on bowel motility. This can be done by preventing peristalsis from appearing in RPCA low rank component. To this end a new stopping criterion was set up based on an example subject for whom both free breathing and breath hold data were available. The same acquisition length was used to acquire both datasets.

A threshold on the sparsity of the RPCA sparse component was used to end the iterations. Given the pseudo-periodical characteristic of respiratory motion and peristalsis, the optimum threshold for the trade-off parameter, λ (see section 4.3.4) was chosen using an analysis of test data in the frequency domain, similar to Sprengers et al. [123]. The frequency of peristalsis is expected to be the same in both breath hold and free breathing. Thus the difference between breath hold and free breathing in the Fourier domain should show only the contribution of respiratory motion. We use such a difference as an indicator of the effect of each iteration in RDDR.

Spectral powers were computed by summing the Fourier transform of every pixel signal through time over the entire field of view (see example Figure 5.1). Figure 5.2 presents the evolution of the spectral power difference with respect to the sparsity of RPCA sparse component. A minimum difference appears clearly when the degree of sparsity is equal to 20%. The degree of sparsity is defined by the ratio of non-zero elements divided by the total number of elements in the sparse component. The new stopping criterion for RDDR is thus chosen when the degree of sparsity of S falls below a threshold of 20%.

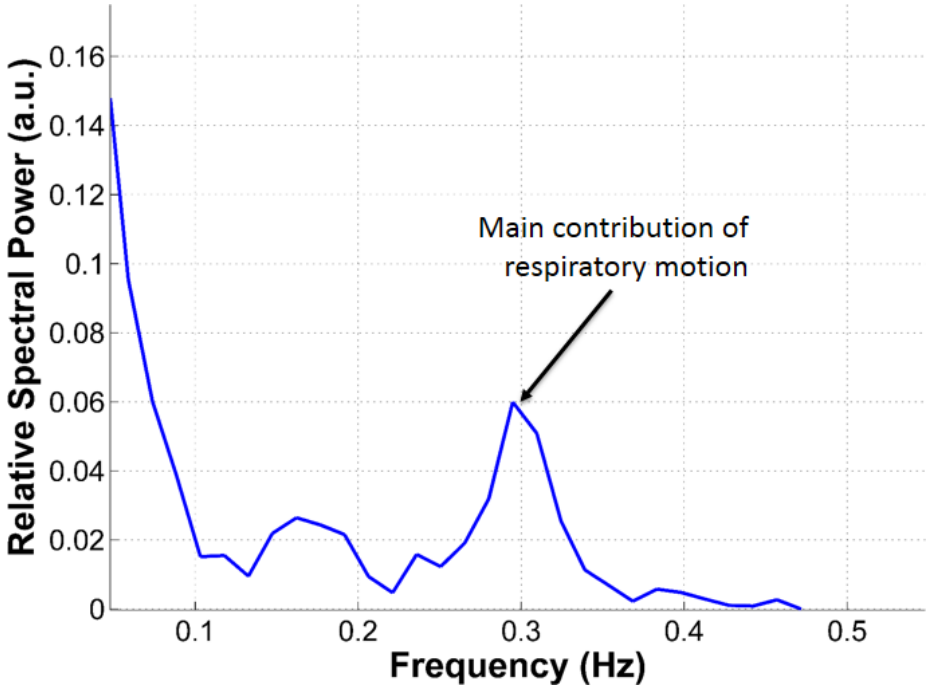

Figure 5.1: Example of spectrum obtained for a free breathing time-series. A peak corresponding to the main contribution of breathing motion appears at 0.3 Hz. Using comparison of such a spectrum with that of breath-hold data can highlight the contribution of breathing and other cyclic mechanisms such as peristalsis.

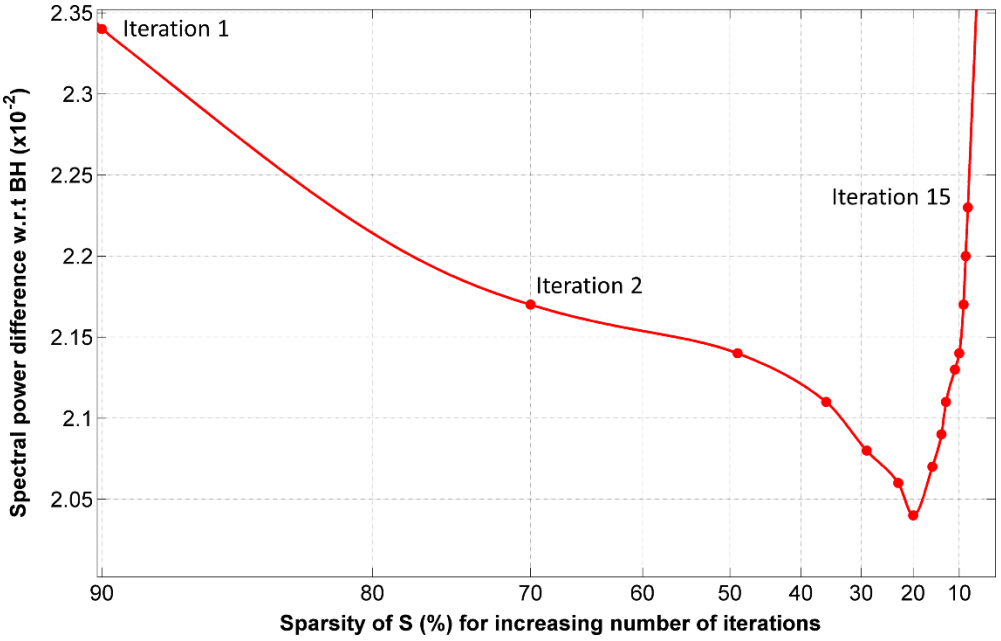

Figure 5.2: Spectral analysis of a subject for tuning of RDDR stopping criterion. Spectral Differences between gradually corrected data and breath-hold is progressively reduced until a minimum is reached. The sparsity of S at that minimum value is chosen as lower threshold to stop the iterative registration.

5.3.2 Combination with Optical Flow registration

Following registration using RDDR to produce respiratory motion free data, bowel motility can be quantified using OF. DRAM corresponds to the combination of the two techniques and is summarized in Figure 5.3.

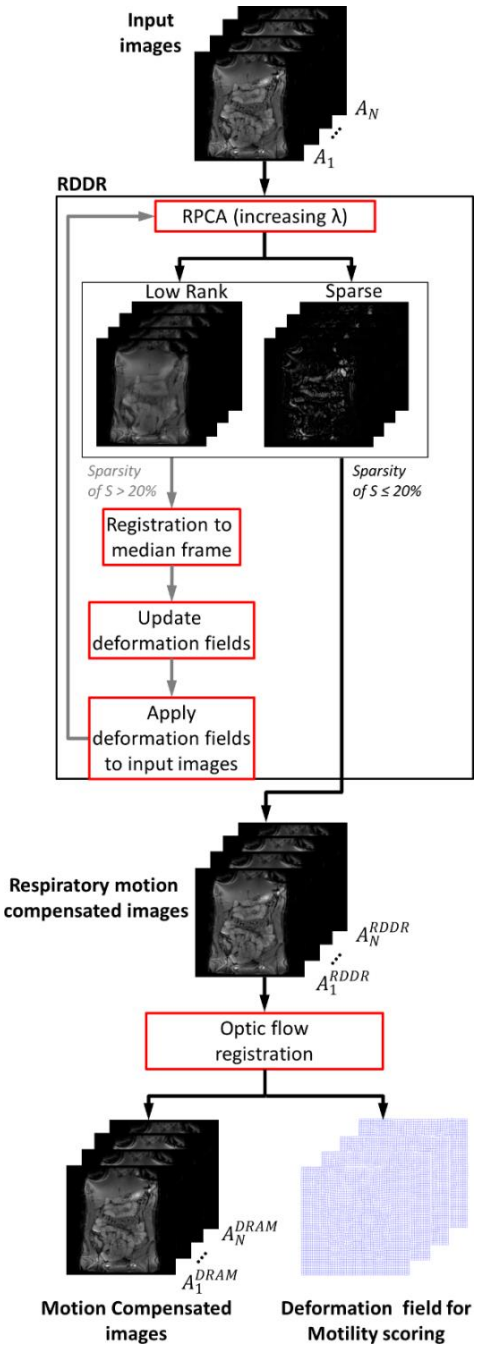

Figure 5.3: Flow chart illustrating the process of DRAM. The parameter λ is gradually increased in RDDR to let more information appear in the Low rank component over iterations.

5.4 **Material and methods**

5.4.1 Data

20 small bowel subjects were scanned. Volunteers fasted for 4h prior to ingesting a contrast solution (1L of 2.5% Mannitol solution) over the 50 minutes prior to the MRI scan. Subjects lay in the prone position and were scanned using a Philips Achieva 3T Multi-transmit MRI scanner (Philips Healthcare, Netherlands) using the manufacturer's torso coil (XL-TORSO). Each subject underwent planning sequences followed by a balanced turbo field echo (BTFE) motility sequence (coronal, 2.5x2.5x5mm voxel size, FOV 420x420x30mm, FA 20 degrees, TE=1.85ms, TR=3.7ms dual channel RF transmit with adaptive RF shimming). A total of 6 slices per volume were acquired using no slice gap and temporal resolution of 1 volume per second. A total of 20 time frames were first acquired in the coronal plane during inspiration breath-hold. Following a 10s recovery period, series of 60 images were acquired in the same anatomical plane during gentle breathing.

5.4.2 Assessment of motion correction accuracy

Each free-breathing data set was registered using OF alone, and DRAM. The results were compared to that of OF applied to data acquired during breath-hold which was used as gold standard for this study. The ability of a pre-processing registration step RDDR to correct free breathing motion before OF was evaluated using quantitative and qualitative analysis.
Time cut representations of the data were also used to provide qualitative information on respiratory motion correction directly after pre-processing with RDDR. One gastroenterology research fellow and one research scientist identified, in consensus, a small bowel loop in the upper left quadrant of each subject, which remained visible through the time series (i.e. did not move out of plane) and drew line ROIs along the bowel cross-section. These ROIs were manually adjusted independently by the two experts in each time point to provide a pseudo ground truth. ROIs were also automatically propagated through

both OF alone and DRAM corrected time-series. Comparison with the ground truth was used to assess the ability of the two techniques to faithfully propagate a linear ROI through small bowel time series data using the average of two independent manually propagated ROIs as a reference. Note that OF deformation fields were used for the propagation of ROIs through the different time frames. Comparison was carried out by computing the changes in line length over time between the manually corrected and automatically propagated ROIs using Bland-Altman (BA) limits of agreement (LoA) and intra class correlation (ICC). Changes in ROIs position were also evaluated by computing the target registration error (TRE) i.e. the distance between each line end-point of the manually corrected and automatically propagated ROIs. A threshold for TREs was set to $1e^{-3}$ mm. Errors below this value were considered as zero.

Parametric motility maps in free breathing small bowel data sets registered with OF and DRAM were computed, using breath hold OF corrected data as a gold standard. Parametric mapping was achieved using the standard deviation of the Jacobian determinant at each pixel σ_J. A motility score was estimated for each subject, by taking the mean σ_J over the bowel region.

5.5 **Results**

Example images of time cuts obtained after registration are shown in Figure 5.4. The time cut representation shows correction of breathing motion after RDDR with little apparent effect on peristaltic motion.

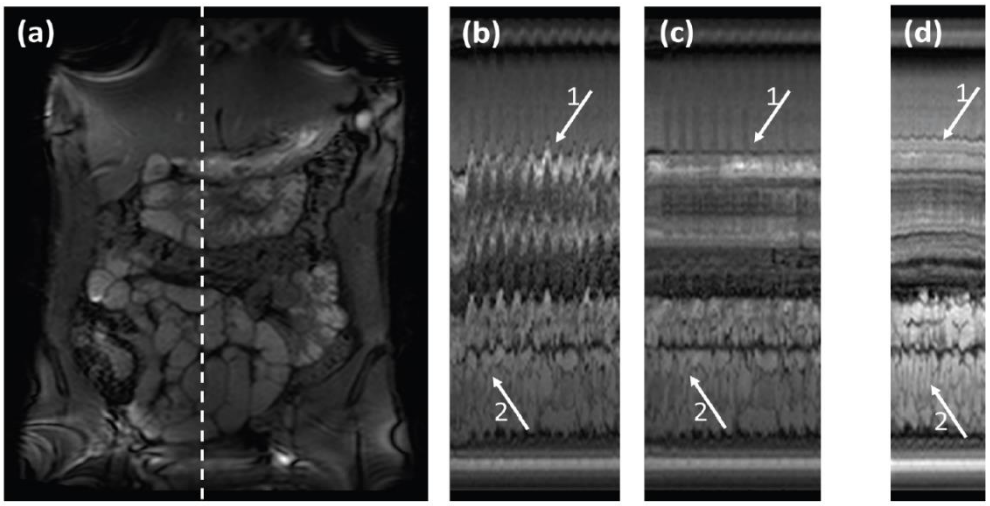

Figure 5.4: Time cut representation of dynamic time-series of the small bowel in a healthy volunteer: the location of the time cuts is indicated by a white dashed line in (a), time cuts before (b) and after registration with RDDR (c) are presented. Breath-hold data is shown as reference (d). Important displacements due to respiratory motion (arrow 1) are accurately corrected by RDDR while preserving bowel motility information (arrow 2).

Inter-reader variability was assessed through BA. For manually corrected OF data, mean difference between readers was 0.41mm LoA ±7.3mm. ICC was 0.85. For the manually corrected DRAM data the mean difference between readers was 0.54mm, LoA ±3.4mm. ICC was 0.96. The BA analysis of line length ROIs in data registered using OF and DRAM with the manual measurements (mean of two observers) is shown in Figure 5.5 a and b. For the data registered using OF alone, the mean difference between the manually corrected and automatically propagated ROIs was -2.0mm (95% LoA ±9mm). For the images processed with DRAM, the mean difference was -0.48mm (95% LoA ±4.15mm).

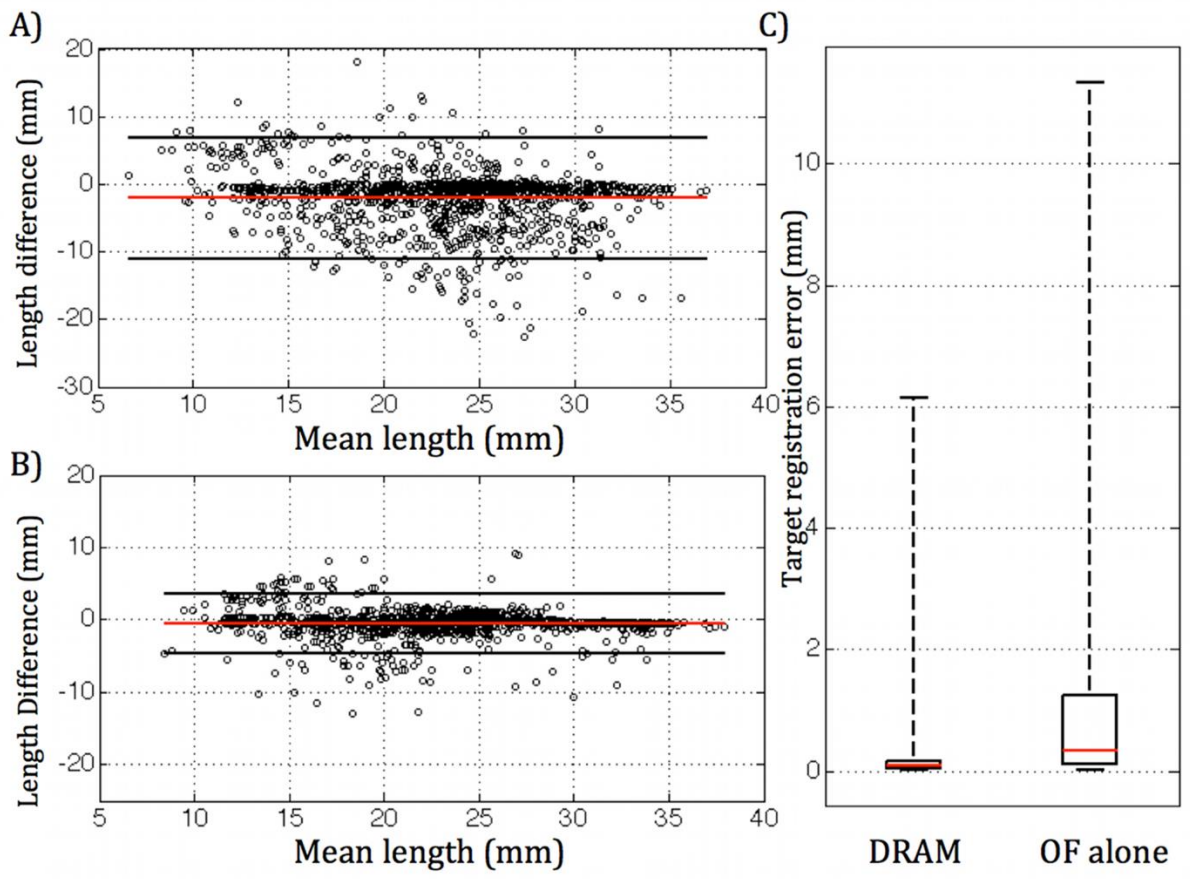

Figure 5.5: Bland Altman limits of agreement for line length ROI small bowel data registered using OF against manually corrected ground truth (a) and data registered using DRAM against manually corrected ground truth (b). Target registration error in DRAM and OF alone (c).

Target registration errors were below the threshold in 49% of the cases with OF only and in 70% of the cases after pre-processing with RDDR. Boxplots for nonzero TREs are shown Figure 5.5c, OF alone yielded a median error of 0.5 mm (IQR 2.27 mm) and DRAM yielded a median error of 0.05 mm (IQR 0.1 mm).

Mean global motility score within the manually placed ROIs for the breath-hold data sets across the cohort was 0.340 (range 0.181 to 0.422). Mean global motility score for DRAM registered data was 0.335 (range 0.189 to 0.430) and OF alone free-breathing data sets was 0.365 (range 0.268 to 0.458). Subjective visualisation of motility colormaps is shown in Figure 5.6 and boxplots for motility scoring are presented in Figure 5.7.

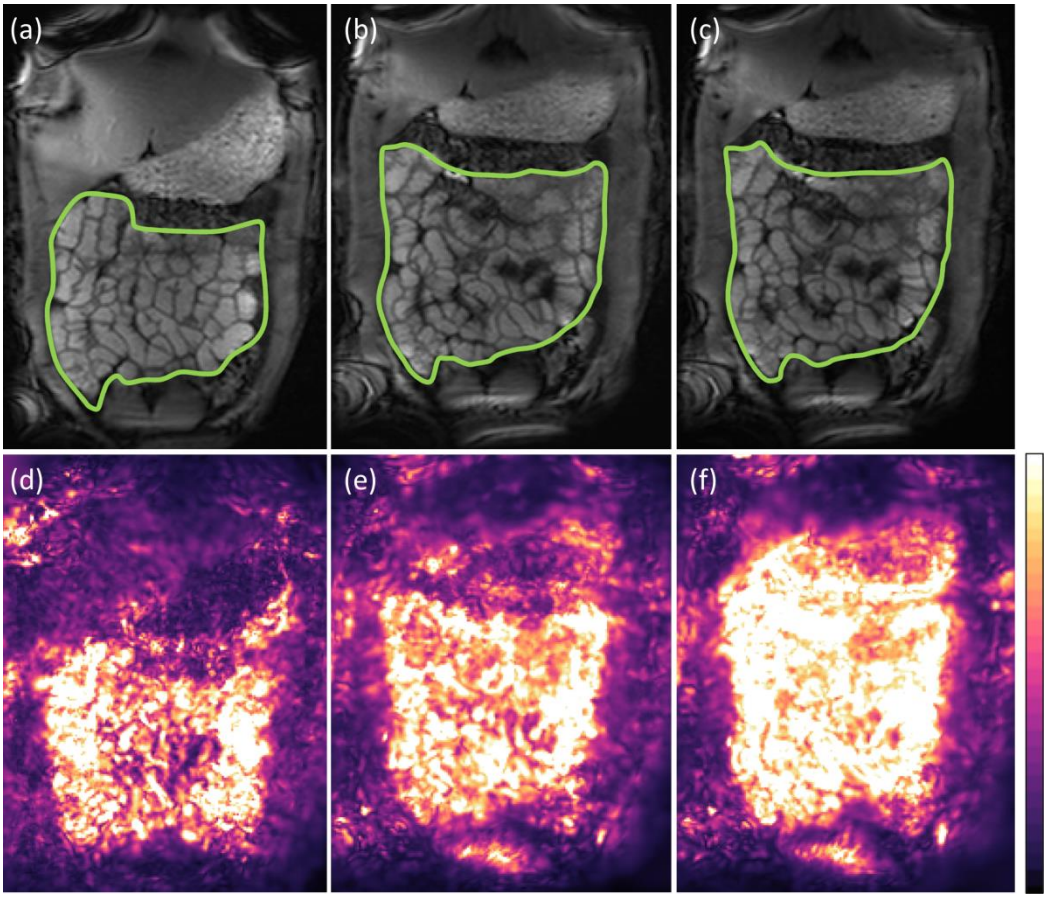

Figure 5.6: Example data with small bowel ROIs and motility maps for breath-hold ground truth (a, d), DRAM (b, e) and OF alone registration alone (c, f) respectively. Respiratory motion compensation is visible in the transverse colon closest to the diaphragm and systemically over the small bowel. The effect of RDDR is less apparent in the lower bowel further from the diaphragm where the effects of free breathing are less pronounced. Motility map shows black as lower motility and white as higher.

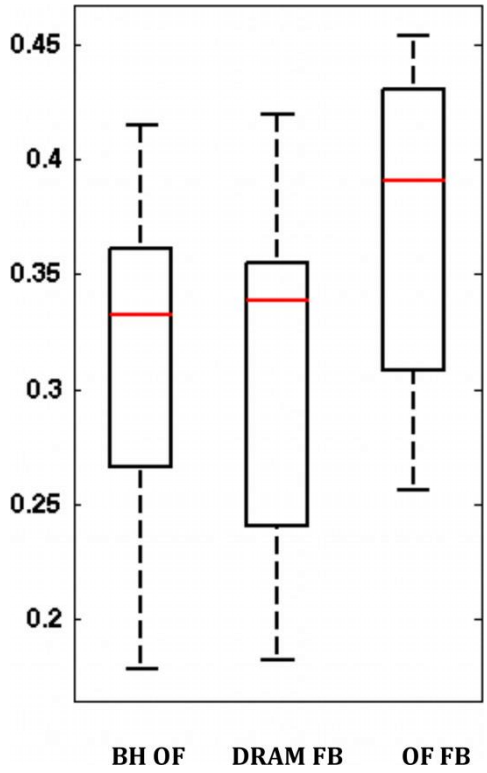

Figure 5.7: Box plots for motility scores derived from OF registration in the 20 subjects with range (dotted line), interquartile range (box) and median (red horizontal line) for breath hold data registered with OF (BH OF), and free breathing data registered with DRAM (DRAM FB) and OF alone (OF FB).

5.6 Discussion

This chapter presented an alternative application of RDDR to correct for respiratory motion before applying an existing OF method to register local deformation generated due to peristalsis. Such an approach could allow rapid and robust data analysis from longer datasets acquired in free breathing. Within DRAM, some of RDDR settings were empirically modified to adapt it to small bowel data. Imposing a stopping criterion on the algorithm allows avoiding loss of information of interest by preventing peristalsis from being seen by registration in RDDR.

Comparable results were obtained for free breathing data corrected using DRAM and the pseudo-ground truth of the breath-hold. Specifically the registration of breath-hold series using OF gave comparable global scores to DRAM whereas a positive bias was observed in global motility scores in free breathing datasets registered with OF alone. This supports the fact that DRAM removes respiratory motion whilst leaving peristaltic motion largely

intact. The breath-hold data was not a perfect ground truth as the data was temporally separated from the subsequent free breathing data collection. However the 30s time difference from the commencement of the breath-hold to the commencement of the free-breathing series is unlikely to impact significantly on bowel motion especially when assessed in a global manner.

The accuracy of the registration technique was assessed by comparing algorithm propagated ROIs and comparing their size and position to a manually adjusted ground truth. The assessment of the data processed with DRAM demonstrated greater registration accuracy with a mean error comparable to previous values in breath-hold studies [34], [124]. Correction using DRAM did however show a slightly larger variance in the BA LoA when compared to the original breath-hold data in [34]. This is likely due to several factors, principally the choice of ROI position which in the current study was the upper left quadrant (i.e. proximal bowel close to the diaphragm) with the specific intention of challenging the capabilities of the respective algorithms with the effects of respiration. Displacement distance of the adjusted ROIs was also assessed. This is a relevant test for registration as it is based directly on displacements reflecting registration accuracy. On average less manual correction was necessary after using DRAM and where ROIs were adjusted, the median distance and variance was several times lower than that without RDDR pre-processing. By collectively assessing these two components of registration fidelity in a challenging region of bowel, both DRAM and OF were subjected to a robust test and in both cases DRAM was found to perform better in comparison to the ground truth and yielded comparable values to existing published studies.

5.7 **Conclusion**

This chapter is about the validation RDDR as a pre-processing technique prior to extracting quantitative metrics to assess small bowel motility in data acquired during free breathing. The work described demonstrates the improvement obtained both in segmental and global

analyses when using DRAM that will likely be of use in clinical studies investigating the bowel motility.

6 Local arterial input function based on DW-MRI – Application to pharmacokinetic modelling in DCE-MRI

6.1 Introduction

This chapter describes recent work on possible extension to DCE-MRI modelling through the creation of a specific arterial input function (AIF) using information from DWI. The aim of this study was to investigate the possible benefit of using a region-specific model for tissue perfusion. Following a description of the state of the art and the proposed extension, we describe the application of the method to a set of clinical data from patients with head and neck tumour who underwent multi-parametric MRI.

This last study represents a combination of the work undertaken on both DWI and DCE-MRI presented in the previous chapters, with a focus on DCE-MRI modelling. An earlier version, based on a smaller number of subjects, has been published in the proceedings of SPIE 2014 [125].

6.2 Arterial Input Function in Pharmacokinetic modelling

In DCE-MRI, the parameters extracted from pharmacokinetic modelling of tissue response to the passage of contrast agents are used to provide a quantitative description of the response to therapy or changes to the tumour region [8], [22], [126]. Thus, accurate model fitting and precise reproducibility of parameter values are essential in clinical studies for diagnosis, prognosis and therapeutic assessment. In order to achieve accurate and reproducible modelling, information on tissue perfusion as well as prior knowledge of contrast agent concentration in blood are required. Models are often dependent on an accurate representation of the AIF, describing the arrival and transit of the bolus through the local arteries and arterioles network. A number of methods for accurate AIF estimation have been developed. It may be estimated at a global level directly from a population specific function [111] or via local fitting of an expected shape to a purely vascular region of interest [43], [127] provided that a suitable artery appears in the imaging field of view

(FOV). Several techniques for automatic detection of the AIF via image segmentation have also been proposed [25], [128]–[130].

It should be noted that methods based on blind estimation of the AIF through the incorporation of a specific model within tissue pharmacokinetic modelling have also been investigated [131]. Although this type of approach alleviates the need for an artery within the FOV, it is limited by high sensitivity to noise and an increased number of degrees of freedom [130], [132].

6.3 Local Region Specific Arterial input Function

Using an accurate AIF is critical for accurate estimation of tissue properties. As described by Calamante et al. [28] in the case of DSC imaging, the same tissue concentration over time can be obtained in different scenarii. This is illustrated in Figure 6.1 where a fast and narrow bolus delivered to tissue with lower perfusion and higher permeability results in the same enhancement profile as a slower and spread bolus delivered to highly perfused tissue with lower permeability.

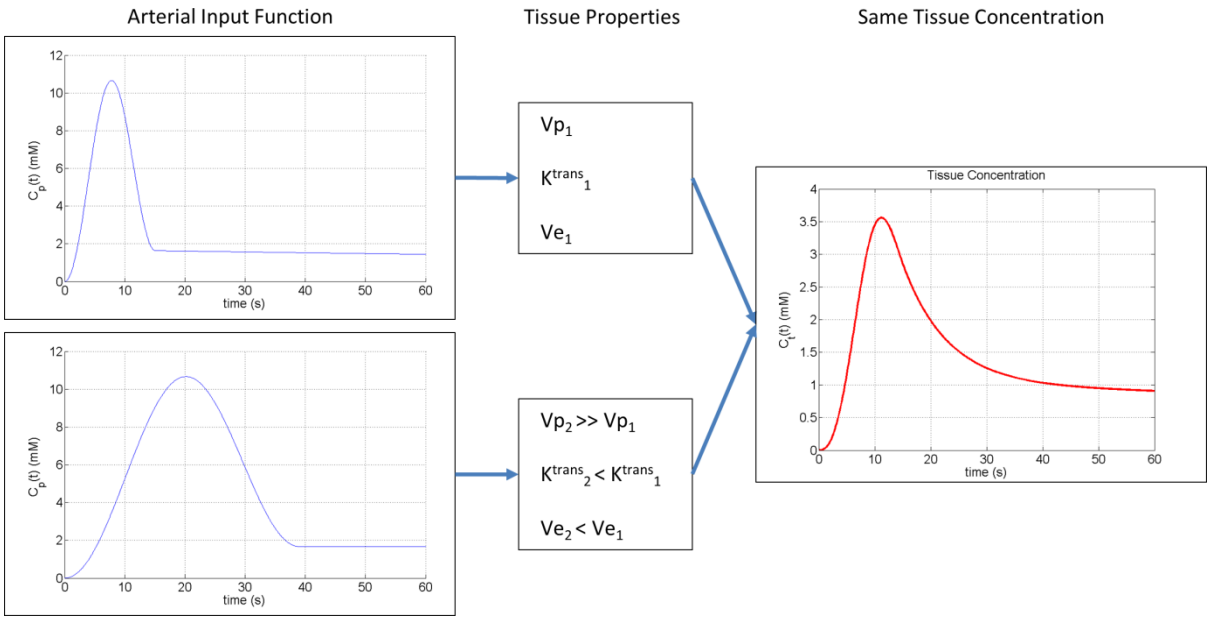

Figure 6.1: Illustration of the need for an accurate estimation of the Arterial input function. Depending on the input contrast agent concentration, tissue with very different characteristics can present similar time concentration curves (adapted from Calamante [28]).

Thus an inaccurate AIF may lead to erroneous tissue characterisation when fitting a pharmacokinetic model to a given enhancement curve. In spite of this most studies based on DCE-MRI analysis use a single AIF per subject [130], [133] or for a group of subjects [21], [134]. However, the fitting of a single upstream arterial input function does not allow for subsequent bolus dispersion through bifurcating and narrowing vasculature and thus the obtained parameters are sensitive to bolus dispersion over the path from the reference arterial region, rather than being specific to the local voxel. If these changes to the global reference AIF can be accounted for by calculation of a region-specific AIF, the subsequent pharmacokinetic model parameters will describe the local tissue more accurately [28], [132].

Some studies have investigated the possibility of using a locally varying AIF. Calamante et al. described the dispersion of the bolus in DSC-MRI using a vascular transport function convolved with the AIF measured in a major artery [26], [27]. This vascular transport function can be modelled as an exponential decay, or using a more complex parametric model of microvasculature [135]. Fluckiger et al. used region specific AIFs based on blind estimation [131], [132].

Motivated by comparable work extending the Tofts model to account for passive diffusion of contrast agent in tissue [136], we show in this work that additional constraints on the fitting of the extended Tofts model to DCE-MRI data derived from independent fitting to diffusion weighted imaging DW-MRI can be used to constrain DCE parameter estimation. Our hypothesis is that since the DW-MRI provides information on the local tissue microstructure (i.e. perfusion at low b-values, cellularity, extracellular space tortuosity and cell membranes' integrity), this in principle allows inference on the local volume available for bulk flow and the local tortuosity given the restrictiveness of the cellular and extra-cellular space. Here we use the ADC, which can be seen as a mixture between diffusion and perfusion in local tissue microstructure, to constrain the fitting of the DCE-MRI, specifically via local variations of arterial input function.

Although the two types of imaging have been associated in many studies [134], [137], [138], these two models for diffusion weighted and contrast enhanced imaging have never been combined in this way. In this work we show that there is some utility in multi-modal, multi-compartment model fitting on pharmacokinetic parameter estimation in head and neck cancer data.

6.4 Proposed approach

The identification of an accurate AIF describing the arrival of contrast agent in the tissue of interest is the main focus of this work. We make use of an analytical AIF given by the Orton model [139] representing a symmetric bolus shape convolved with a transfer function modelling the interaction with body tissue on circulation:

$$C_p(t) = a_b(1 - \cos(\mu_b)) \otimes a_g \exp(\mu_g t) \quad (6.1)$$

This model provides an analytical form that may be closely fitted to a population model [111], but additionally is flexible enough to be fitted on a subject specific basis [43], [140], for instance to a major artery. In equation (6.1), a_b and μ_b are experimental parameters of the local bolus shape whilst a_g and μ_g describe the interaction of this bolus in transit to the tissue and thus these are region-dependent parameters. The effect of these parameters is described in Figure 6.2.

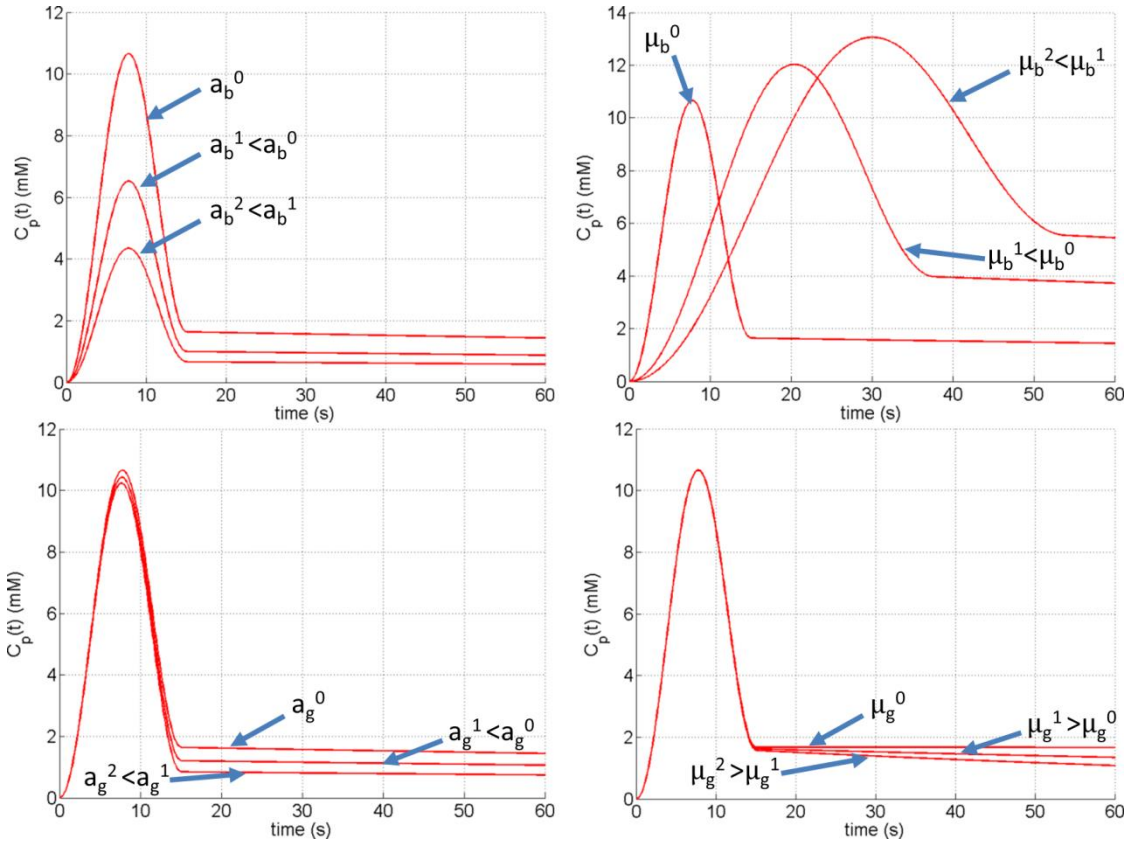

Figure 6.2: Illustration of the effect of the Orton model parameters on the shape of the AIF, $C_p(t)$

Specifically μ_b describes how the shape of the bolus changes as it passes through the local vasculature, strong interaction with local tissue will thus cause the bolus to become more disperse and delayed, with the impact that μ_b is locally decreased.

For a given dataset, a global AIF (parameterized by a_b^0, μ_b^0, a_g^0, and μ_g^0) can be obtained by fitting the Orton model to the enhancing signal from an artery ROI. By using the changes in ADC value with respect to the reference ADC for free water diffusion (ADC_{Ref} set to 3x10^{-3} mm^2/s), we can derive a local AIF reflecting the microstructure for specific ROI, or each pixel p in the FOV. This is achieved using the following heuristic changes on the Orton model:

$$C_p(p,t) = a_b^0(1 - \cos(\mu_b^*(p))) \otimes a_g^*(p)\exp(\mu_g^*(p)t) \qquad (6.2)$$

where,

$$\mu_b^*(p) = \mu_b^0 \exp\left(\frac{ADC(p)}{ADC_{Ref}} - 1\right)$$

$$a_g^*(p) = a_g^0 \exp\left(\frac{ADC(p)}{ADC_{Ref}} - 1\right) \quad (6.3)$$

$$\mu_g^*(p) = \mu_g^0 \frac{ADC(p)}{ADC_{Ref}}$$

The proposed modifications are based on the assumption that a lower ADC value broadly represents an environment with increased cellularity; thus vessels passing through this region may be more tortuous or narrower and blood flow is altered such that the bolus becomes more disperse. This increase in dispersion may be encoded by a locally decreased μ_g, a_g and μ_b. The effect of such modifications is illustrated in Figure 6.3.

Pixel wise fitting of the mono-exponential diffusion model provides the ADC parameter to modify the AIF locally and thus produces a map that provides local tissue specific information on the response to contrast agent bolus.

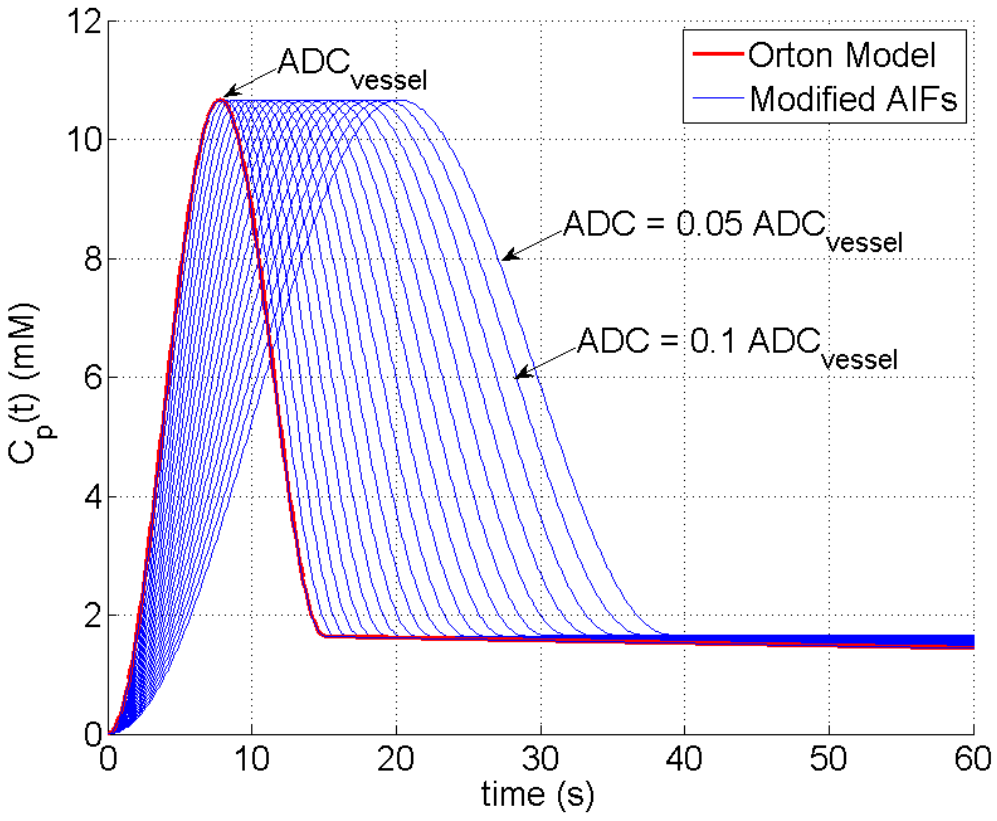

Figure 6.3: Illustration of the effect of ADC based modifications of the Orton AIF model. The lower the ADC the wider the bolus

6.5 Application to Clinical data

6.5.1 Data

Multi-parametric MR data of head and neck were acquired for twenty nine subjects (20 patients and 9 healthy volunteers). Imaged patients satisfied inclusion criteria of histologically confirmed squamous cell carcinoma with unilateral cervical nodal metastatic disease at pre-therapy staging. All images were obtained from a 1.5T Siemens (Siemens, Erlangen, Germany) Avanto magnet with the manufacturer's carotid coils. DCE time-series were acquired in the coronal plane using a spoiled gradient echo sequence with TR/TE=2.89ms/1.01ms and a flip angle of 25^{o}. Images were acquired with a slice thickness of 2.5 mm and matrix size was 256×256. In total 50 time frames were acquired with a temporal resolution of 3s. Axial DW images of the neck were acquired using EPI. Trace DW images of the head and neck were acquired with two receiver coils using GRAPPA. Images were averaged four times for improved SNR. Diffusion gradients were applied in 3 orthogonal directions at each of 6 b-values (0, 50, 100, 300, 600 and 1000 s/mm^{2}). Images were acquired with TR/TE = 8.7s/88ms and a 128x128 matrix size. Total acquisition time for diffusion MR imaging was 6 minutes and 10 seconds. For each subject, four T1 weighted MR images were acquired in the coronal plane also using a spoiled gradient echo sequence with multiple flip angles (5^{o}, 15^{o}, 25^{o} and 35^{o}) with TR/TE=2.89s/1.01ms and 256×256 matrix size. The same type of sequence was chosen for both DCE and multiple flip angle data to minimize the influence of changes in T1 that might not be related to GD-DTPA. Cervical nodes regions of interest (ROIs) for subsequent model fitting were contoured in each subject by a radiologist: cancerous in patients (20 ROIs) and normal in healthy subjects (12 ROIs).

6.5.2 Data pre-processing

Before parametric mapping, the DCE-MRI and multiple flip angle pre-contrast T1-weighted volumes were registered using a 3D version of RDDR. These were then re-sliced in the axial plane to match the diffusion weighted data. DW-MR data were registered using a NMI based FFD technique. For each subject the physical slice(s) containing the contoured ROIs were extracted for subsequent analysis.

6.5.3 Parametric mapping

T1 and proton density (S_0) mapping was computed using a pixel by pixel approach as the multi-flip angle data had been registered along with the DCE data. ADC maps were computed using a maximum probability scheme to a mono-exponential decay (as described in section 3.5.1.1). For each ROI two arterial input functions were computed: first we applied the Orton model, fitted to the time-intensity curve of the common carotid artery section to provide a subject specific global AIF and second we modify this baseline AIF using the mean ADC in the considered ROI to create a local AIF as described in 6.4. Subsequent fitting of the extended Tofts model to obtain estimates for V_e, V_p and K^{Trans} was achieved using a non-linear least squares algorithm with conversion from signal intensity to contrast agent concentration C(t) achieved using the pre-computed AIFs. T1 and S_0 values were included in the estimated parameters to give more flexibility to the fitting. The previously computed T1 and S_0 were used as initial guesses. A pixel wise coarse-to-fine approach with two resolution levels was used to avoid convergence to local minima. Within the fitting V_e and V_p values were restricted to the range [0.01 1], and K^{Trans} to the range [0 5] min^{-1} to avoid convergence to unphysical values. The pharmacokinetic models obtained with both models of AIF were compared to assess the proposed method.

An additional experiment was conducted based on the range of ADC values observed in both cancer and normal tissue. In order to assess the validity of the proposed heuristic, series of modified AIFs were generated for each subject using all the values in the ADC range. For each data set, residual errors obtained afters fitting the extended Tofts Model with the different AIFs were computed. The ADC value producing the lowest fitting error was then compared to the actual ADC obtained for the corresponding subject.

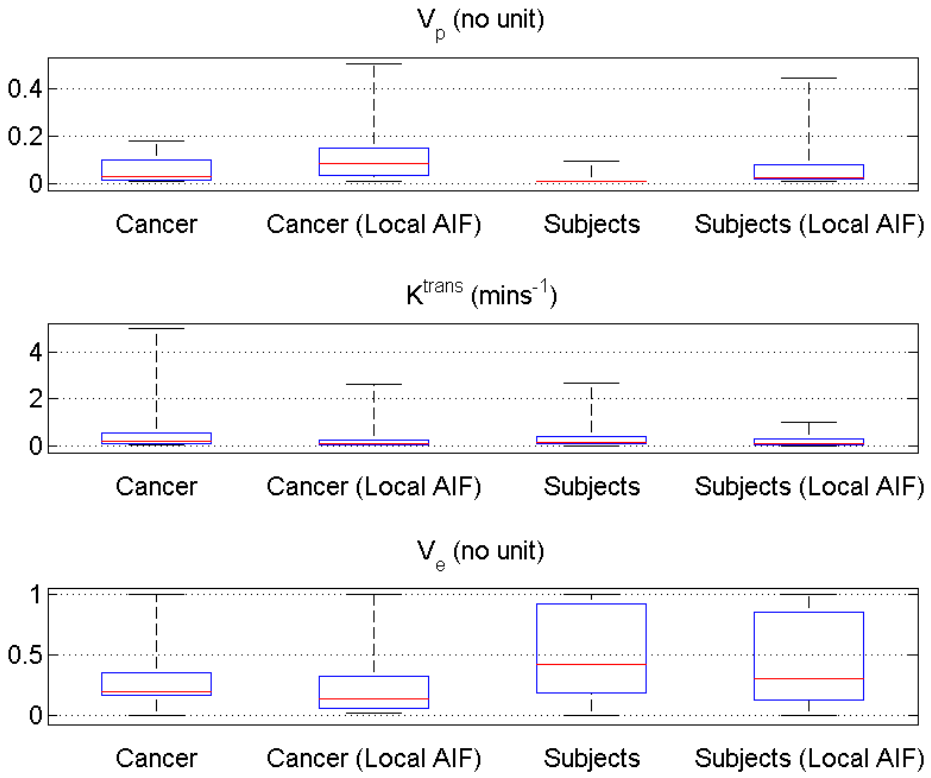

Figure 6.4: Box and whisker plots of the estimated pharmacokinetic parameters across all ROIs for both cancerous and normal nodes, Overall the use of a local model increases V_p and decreases V_e and K^{trans}. Each plot shows: the median error (red line), the 25th and 75th percentile (blue box), and the full data extent (black dashed line).

6.6 Results

The estimated Tofts model parameters across all data are summarized in Figure 6.4. As predicted by the theory the effect of a local AIF with delayed and spread bolus tends to increase the estimated values of V_p and decrease V_e and K^{trans}. However these changes were only significant in the case of V_p ($p < 0.01$). A decrease in the K^{trans} parameter inter-quartile range was observed in both patients (global 0.44 min^{-1}; local 0.19 min^{-1}) and subjects (global 0.32 min^{-1}; local 0.26 min^{-1}).

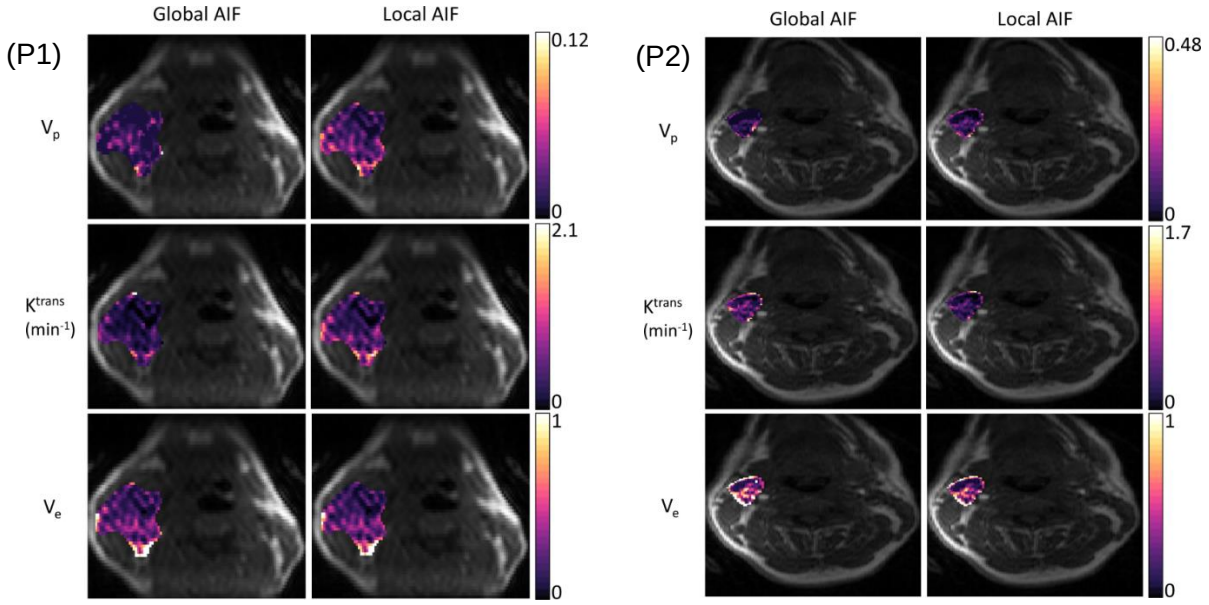

Figure 6.5: Example of parametric maps obtained for two patients with large cancerous nodes. Across both tumours the use of a local AIF model yields a significant increase in V_p and more homogeneous K^{trans} values.

Example parametric maps for two patients (P1 and P2) along with representative enhancement curves and model fit are presented Figure 6.5 and 6.6. In both P1 and P2 the lower ADC in the tumour region causes the local AIF peak to be delayed with a wider peak and a slower washout phase compared to the global model. Such effect results in a fitting with important reduction of the residual error: by 51% in P1 and by 53% in P2. In addition, an offset in the baseline signal can be observed in the model fit with the global AIF for the two patients. This effect is due to the changes in T1 and S_0 allowed in the fitting, may be related to an attempt of compensating for a potentially inaccurate AIF by the modelling scheme.

More detailed results are available in Table 6.1 and 6.2. Interestingly, in 9 out of the 12 healthy subject's ROIs, pharmacokinetic modelling with global AIFs resulted in median V_p values equal to the pre-set lower bound. This indicates possible convergence to local minima. However such a phenomenon was not observed with local AIFs. Also, in 2 out of the 12 subjects and 2 out of the 20 patients, the median V_e value reached the pre-set upper bound. This was observed for both the local and the global model. Again this suggests that the fitting scheme may have not converged to an optimal solution.

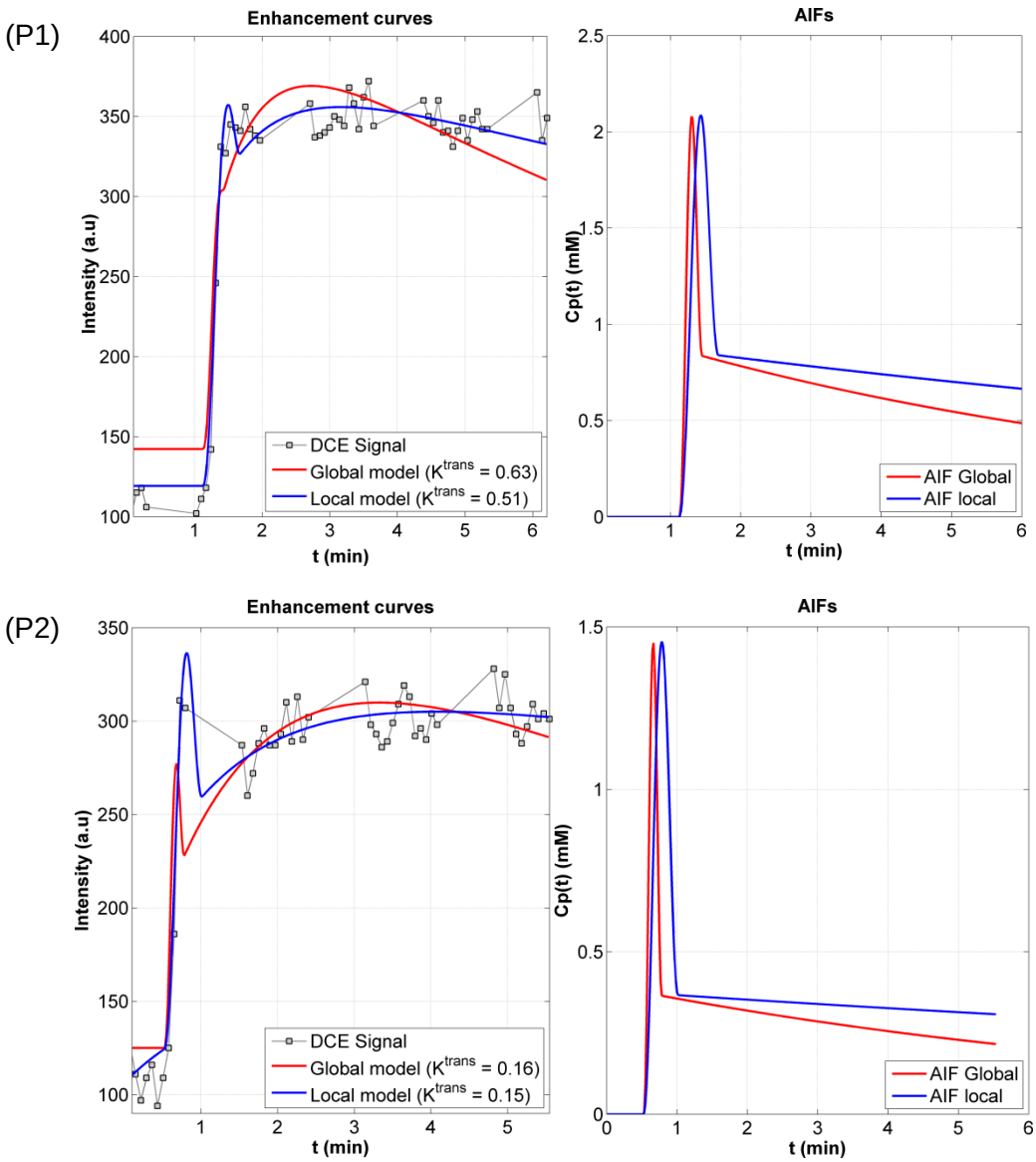

Figure 6.6: Representative time intensity curves and model fit for the two patients (P1 and P2) along with the two AIF models. In both cases the slightly delayed peak and slower washout in the AIF leads to a more sensible model fit.

Result from the validation experiment are showed in Table 6.3 and 6.4. Local AIF models provided the lowest fitting error in 7 out of 20 patients and in 7 out of 12 subjects. ADC values were ranged between 0.5 and 1.65 10^{-3} s/mm^2 in patients, and between 0.6 and 2.4 10^{-3} s/mm^2 in normal subjects. In patients, there was at least a 20% difference between the ADC yielding the minimal errors and the actual ADC value, except in 1 case were the difference was 2% of the real ADC. In normal subjects, that difference was higher than 40% in most cases except 1 where its value was 5% of the actual ADC. These difference

suggest that the proposed heuristic might not produce accurate modification of the shape of the AIF.

Cancer Nodes	Model	Vp	K^{trans} (min^{-1})	Ve	ADC (10^{-3} s/mm^2)
1	**Global**	0.112 (0.075)	0.367 (0.360)	0.174 (0.149)	0.86
	Local	0.106 (0.034)	0.141 (0.108)*	)0.073 (0.111)*	
2	**Global**	0.017 (0.079)	0.140 (0.020)	0.203 (0.145)	0.53
	Local	0.045 (0.087)	0.064 (0.029)	0.197 (0.174)	
3	**Global**	0.012 (0.009)	0.328 (0.303)	0.237 (0.174)	0.96
	Local	0.051 (0.035)*	0.088 (0.063)*	0.105 (0.077)*	
4	**Global**	0.054 (0.024)	0.317 (0.357)	0.266 (0.270)	1.03
	Local	0.157 (0.090)*	0.347 (0.286)	0.140 (0.277)*	
5	**Global**	0.019 (0.029)	0.032 (0.114)	0.081 (0.312)	1.25
	Local	0.028 (0.045)*	0.045 (0.095)	0.049 (0.186)	
6	**Global**	0.010 (0.023)	0.474 (0.607)	0.120 (0.177)	0.81
	Local	0.032 (0.038)*	0.139 (0.223)*	0.019 (0.061)*	
7	**Global**	0.017 (0.022)	0.596 (0.749)	0.208 (0.070)	0.83
	Local	0.076 (0.052)*	0.096 (0.038)*	0.070 (0.040)*	
8	**Global**	0.050 (0.034)	0.110 (0.079)	0.152 (0.079)	1.08
	Local	0.087 (0.072)*	0.050 (0.523)*	0.058 (0.050)*	
9	**Global**	0.030 (0.019)	0.185 (0.216)	0.195 (0.112)	1.37
	Local	0.051 (0.026)*	0.151 (0.112)*	0.151 (0.072)*	
10	**Global**	0.124 (0.049)	0.079 (0.052)	0.175 (0.109)	1.11
	Local	0.115 (0.056*)	0.049 (1.807)*	0.042 (0.176)*	
11	**Global**	0.179 (0.356)	0.094 (0.079)	0.421 (0.572)	1.32
	Local	0.099 (0.215)	0.028 (0.031)	0.138 (0.757)	
12	**Global**	0.010 (0.087)	0.093 (0.320)	0.191 (0.524)	0.96
	Local	0.010 (0.098)	0.078 (0.338)	0.531 (0.094)*	
13	**Global**	0.010 (0.012)	0.174 (0.156)	0.188 (0.079)	1.25
	Local	0.038 (0.031)*	0.158 (0.104)*	0.164 (0.082)	
14	**Global**	0.042 (0.024)	0.077 (0.861)	0.000 (0.015)	1.23
	Local	0.010 (0.006)*	0.023 (0.025)*	0.037 (0.151)	
15	**Global**	0.135 (0.087)	0.163 (0.051)	0.285 (0.298)	1.15
	Local	0.143 (0.043)	0.089 (0.012)*	0.151 (0.295)*	
16	**Global**	0.023 (0.022)	0.643 (0.795)	1.000 (0.545)	1.03
	Local	0.172 (0.124)*	0.644 (0.544)	1.000 (0.626)*	
17	**Global**	0.087 (0.539)	0.862 (0.731)	1.000 (0.465)	0.96
	Local	0.367 (0.477)*	0.759 (0.719)*	1.000 (0.783)*	
18	**Global**	0.021 (0.010)	0.064 (0.096)	0.108 (0.101)	0.85
	Local	0.033 (0.010)*	0.069 (0.083)	0.068 (0.071)*	
19	**Global**	0.010 (0.245)	5.000 (1.398)	0.723 (0.289)	1.46
	Local	0.505 (0.475)*	2.381 (0.887)*	0.449 (0.287)*	
20	**Global**	0.112 (0.202)	4.596 (2.094)	0.742 (0.219)	1.66
	Local	0.286 (0.265)*	6.619 (2.115)	0.657 (0.227)*	

Table 6.1: Detailed Tofts model fit parameters and ADC values for cancerous cervical nodes using both global and local AIFs. Pharmacokinetic parameters values are given as median (IQR). Significant difference between the local and global model is indicated by '*'.

Normal Nodes	Model	Vp	K^{trans} (min^{-1})	Ve	ADC (10^{-3} s/mm^2)
1	**Global**	0.010 (0.017)	2.662 (1.630)	0.856 (0.457)	0.87
	Local	0.445 (0.568)*	0.882 (0.435)*	0.316 (0.123)*	
2	**Global**	0.010 (0.007)	0.023 (0.016)	1.000 (0.791)	2.4
	Local	0.010 (0.007)	0.023 (0.016)	1.000 (0.797)	
3	**Global**	0.010 (0.000)	0.501 (0.763)	0.372 (0.379)	0.59
	Local	0.092 (0.066)*	0.268 (0.198)*	0.236 (0.121)*	
4	**Global**	0.010 (0.023)	0.212 (0.144)	0.987 (0.669)	1.17
	Local	0.022 (0.018)	0.204 (0.135)*	1.000 (0.547)	
5	**Global**	0.010 (0.120)	0.119 (0.133)	0.472 (0.798)	1.02
	Local	0.025 (0.025)	0.054 (0.043)*	0.496 (0.492)	
6	**Global**	0.093 (0.019)	0.095 (0.050)	0.203 (0.022)	0.89
	Local	0.026 (0.009)*	0.026 (0.001)*	0.128 (0.017)	
7	**Global**	0.010 (0.047)	0.183 (0.148)	0.673 (0.434)	1.37
	Local	0.062 (0.078)	0.071 (0.023)*	0.701 (0.691)	
8	**Global**	0.010 (0.004)	0.140 (0.114)	0.144 (0.109)	0.89
	Local	0.018 (0.011)*	0.031 (0.050)*	0.084 (0.055)	
9	**Global**	0.010 (0.010)	0.010 (0.010)	0.000 (0.149)	1.47
	Local	0.010 (0.010)	0.010 (0.010)	0.000 (0.115)	
10	**Global**	0.010 (0.019)	0.325 (0.234)	0.376 (0.198)	1.59
	Local	0.015 (0.009)	0.312 (0.216)	0.296 (0.143)	
11	**Global**	0.010 (0.076)	1.464 (0.277)	1.000 (0.446)	1.13
	Local	0.205 (0.342)*	1.021 (0.190)*	1.000 (0.472)	
12	**Global**	0.027 (0.059)	0.089 (0.219)	0.161 (0.370)	0.91
	Local	0.026 (0.072)	0.084 (0.231)	0.126 (0.297)	

Table 6.2: Detailed Tofts model fit parameters and ADC values for normal cervical nodes using both global and local AIFs. Pharmacokinetic parameters values are given as median (IQR). Significant difference between the local and global model is indicated by '*'.

Cancer Nodes	Residual Global AIF model)	Residual (Local AIF model)			ADC min (10^{-3} s/mm^2)	ADC real (10^{-3} s/mm^2)
		Median	IQR	Min		
1	0.142	0.147	0.003	0.144	1.55	0.86
2	0.143	0.145	0.001	0.144	1.55	0.53
3	0.149	0.136	0.020	0.126	1.65	0.96
4	0.141	0.148	0.001	0.145	1.65	1.03
5	0.144	0.144	0.001	0.144	1.60	1.25
6	0.137	0.150	0.003	0.145	0.65	0.81
7	0.134	0.153	0.013	0.143	1.65	0.83
8	0.130	0.156	0.009	0.143	1.55	1.08
9	0.121	0.164	0.017	0.149	1.65	1.37
10	0.087	0.181	0.038	0.148	1.65	1.11
11	0.140	0.148	0.012	0.140	1.35	1.32
12	0.147	0.142	0.037	0.108	1.60	0.96
13	0.130	0.157	0.018	0.141	1.65	1.25
14	0.150	0.138	0.002	0.137	1.65	1.23
15	0.133	0.153	0.008	0.148	1.65	1.15
16	0.160	0.127	0.001	0.126	1.30	1.03
17	0.176	0.104	0.006	0.099	0.50	0.96
18	0.136	0.152	0.007	0.146	1.65	0.85
19	0.137	0.152	0.008	0.143	0.50	1.46
20	0.139	0.149	0.008	0.142	0.60	1.66

Table 6.3: Comparison of fitting residual errors obtained with the global AIF model and local AIFs models for a range of ADC values observed in Patients data. The last two columns show the ADC producing the minimum residual error and the actual ADC for each patients. For each patient the minimal residual error between the different AIFs is highlighted.

Normal Nodes	Residual (Global AIF model)	Residual (Local AIF model)			ADC min (10^{-3} s/mm^2)	ADC real (10^{-3} s/mm^2)
		Median	IQR	Min		
1	0.149	0.140	0.004	0.136	1.65	0.87
2	0.129	0.103	0.009	0.095	0.60	2.40
3	0.112	0.121	0.004	0.116	2.40	0.59
4	0.108	0.125	0.010	0.110	2.35	1.17
5	0.123	0.109	0.005	0.103	1.70	1.02
6	0.106	0.123	0.014	0.110	2.40	0.89
7	0.118	0.113	0.004	0.110	1.45	1.37
8	0.118	0.111	0.007	0.108	1.60	0.89
9	0.109	0.124	0.009	0.116	0.85	1.47
10	0.107	0.126	0.011	0.113	2.40	1.59
11	0.107	0.132	0.023	0.105	2.05	1.13
12	0.115	0.117	0.002	0.115	2.40	0.91

Table 6.4: Comparison of fitting residual errors obtained with the global AIF model and local AIFs models for a range of ADC values observed in normal subjects data. The last two columns show the ADC producing the minimum residual error and the actual ADC for each patients. For each subject the minimal residual error between the different AIFs is highlighted.

6.7 Discussion

In this chapter we attempted to address the challenge of obtaining an accurate Arterial input function for the modelling of tissue properties in DCE-MRI. Theoretically, a technique that allows more accurate modelling of the local arterial injection of contrast agent may be advantageous. For instance, this type of local model might be beneficial where important vascularization changes can be expected such as in the liver or during the early stage of a tumour growth. By absorbing the changes caused by subsequent bolus dispersion of the global reference AIF in transit to the tissue into the local AIF, the influence of these are removed from the subsequent Tofts model parameters, a modification that may be beneficial for accurate local assessment of the pharmacokinetic parameters.

The results obtained here are modest but encouraging. Potential benefit of the local AIF model include more homogeneous K^{trans} maps, although the last experiment did not highlight a particular benefit in terms of residual fitting errors. However, other types of modifications also based on information from DWI could be beneficial and provide a more robust estimation of the AIF than the global model. In any case further comparison with existing techniques using automated local AIF modelling [132] would be of interest.

6.7.1 Limitations

There are a number of limitations to this work that should separately be investigated, some of which are not only applicable to this study but to DCE and DW imaging in general. Also, the proposed modification to the AIF shape parameters is very heuristic and the way it describes the complex bolus-tissue interaction may not be fully accurate, thus a more sophisticated modification to the arterial input function such as a model of bolus transit between artery and capillary bed might provide a more accurate representation of tissue pharmacokinetic properties. The value used as reference for ADC assumes free diffusion, a better approximation should be based on the properties of blood in bigger arteries.

The assumption that lower ADC values reflect an increased vessel tortuosity and more disperse input seems intuitively correct in the case of a tumour. However, in many situation changes in ADC are not related to vasculature. For instance, in acute stroke ADC can be decreased by 40% [1] whereas the local vasculature remains unchanged (although local tissue perfusion is altered).

With regards to the DCE-MRI, part of the enhancement peak was missing in the measured AIF in some cases. While this can be corrected to a degree through the use of an AIF model, a more finely sampled bolus arrival period may be advantageous. Also, T1 fitting procedures are generally found to be noisy, especially in head and neck data because of complex anatomical features and pronounced susceptibilities [141], which can lead to important errors in the pharmacokinetic parameters estimates [142]. If the conversion of pixel intensities to changes in contrast agent concentration is embedded in the pharmacokinetic modelling, some flexibility might be given to tissue native T1 and proton density in order to improve the fitting. However this increases the number of degrees of freedom and makes the modelling more complex. Each of these last points also relies on an appropriate optimisation strategy for which non-linear least square routines may be insufficient. Lastly, the assessment of accuracy in DCE-MRI model fitting is notoriously difficult – in this work the application shows some changes that need to be compared to an accepted measurement of the local tissue perfusion [143].

6.7.2 DWI modelling

The proposed heuristic uses DWI to locally modify the AIF which has the advantage of including microstructural information. In this work we generated ADC maps using a mono-exponential decay model. Such a model was preferred to bi-exponential decay (section 2.3.2.2) because a single parameter that summarizes the information from DWI (thought to be a mixture of perfusion and diffusion) was simpler to incorporate into the AIF model. More complex modifications based on bi-exponential decay parameters (pseudo-diffusion

component, ADC and perfusion fraction) would be of interest. However care should be taken to clearly identify the physiological link between these parameters and those involved in the Orton model.

6.7.3 ROI or pixel based analysis

An ROI based approach was chosen − instead of a pixel by pixel computation of the local AIFs − in order to avoid errors due to mismatching features between the DWI and DCE-MRI data. An additional registration step might be used to compensate for distortions appearing in DWI data. However this was not applied here because of the relatively poor resolution in the re-sliced axial DCE-MRI data. Visual delineation of ROIs was thought to be more reliable for the pharmacokinetic modelling. Nevertheless local AIFs defined pixel wise or using clusters of pixels [132] might have enough flexibility to reflect possible heterogeneity within the tumour. In some cases the passage of the bolus can vary between the different parts of the same tumour region (e.g. tumour rim and necrotic tumour core). Even though a better understanding of the effect of perfusion on the ADC is needed, the incorporation of a spatially varying input function might increase the sensitivity of the modelling to tissue vascular properties at finer scales.

6.8 **Conclusion**

This last chapter has discussed the potential benefit of using DWI to locally constrain the AIF and obtain more specific information on tissue perfusion in the quantitative analysis of DCE-MRI. Although other techniques based on a similar concept have been developed, the method introduced here investigates an alternative which does not require blind estimation. The concept may also be extended to include other imaging information that relates to micro-structure or perfusion, for example ASL data. Some changes were observed when using a local AIF model, although the conducted preliminary validation did not highlight any

significant improvements. However, such an approach can be investigated more in depth and modelling of the local AIF using multi-parametric MRI could be possible.

Finally, this work combines all the different aspects of the work undertaken during this PhD (DWI modelling, registration) within a multi-parametric analysis of DCE-MRI data. The proposed method also introduces a way to gather different elements of multi-parametric quantitative MRI. A more evidence-based combination of the microstructural sensitivity of DWI with the perfusion specificity of DCE-MRI might provide useful information on tissue properties.

7 Conclusions and Future Directions

7.1 Advances made

The overall aim of this thesis was to contribute to quantitative MRI through the improvement of data processing and analysis. In the work presented in the different chapters, a number of challenges were addressed: noise modelling and bias correction, motion correction, and extension of physiological models. Some of the main quantitative MRI techniques were considered (DWI, DCE-MRI) as well as some more specific measurement techniques (Dynamic MRI of the small bowel).

The problem of bias due to noise in the modelling of low SNR diffusion weighted data was treated in chapter 3. Different methods, with varying degree of complexity were considered to correct for such bias when estimating the apparent diffusion coefficient. A relatively simple maximum likelihood approach was first considered assuming uniform, stationary noise distribution across the imaged field of view. More complex solutions were also considered to account for spatially varying noise due to parallel imaging as well as changes caused by data averaging. These included a theoretical approach to provide a model for the noise distribution, and a more practical approach using a direct bias correction, assuming certain noise characteristics, prior to tissue properties estimation. Although no ideal solution was found, this project highlighted the necessity to use accurate noise modelling in clinical DWI and the important influence of acquisition strategies on the expected nature of the noise distribution.

Chapter 4 introduced a novel registration technique for correction of misalignments induced by inter-frame motion in DCE-MRI. The proposed method, named Robust Data Decomposition Registration (RDDR), utilizes iterative separation of motion and contrast enhancement effects to avoid unphysical changes likely to appear with more classic registration algorithms. RDDR has been published in [82]. It allowed significant improvement of tissue time intensity curves compared to existing techniques. The purely mathematical nature of data decomposition in RDDR can be a source of limitations.

However the successful registration of multiple types of data and imaged organs (liver, small bowel, prostate) using the same algorithm settings suggests the method is robust.

An extension of RDDR was introduced in chapter 5 for an alternative application to small bowel motility quantification in the presence of free breathing. In that case the ability of RDDR to work as a non-linear filter in terms of motion compensation is demonstrated.

RDDR can remove undesirable effects while preserving information on a mechanism of interest. Such a scheme could have an important impact in the future as it could alleviate the need for breath holding during dynamic MRI acquisitions and potentially allow longer dynamic acquisition leading to a better understanding of the different components of small bowel peristalsis.

The last chapter dealt with the modelling of the arterial input function for DCE-MRI analysis, using prior knowledge from DWI to create a local model of blood perfusion in tissue. By taking advantage of the work presented in the previous chapters, a full pipeline for data processing and pharmacokinetic modelling was set up. Although the results obtained are modest, the use of a local AIF model showed a difference in the estimated tissue properties in the analysed data. If well validated, the idea of combining microstructural information from DWI with perfusion specific DCE-MRI may provide useful information.

From a general point of view, this thesis explored different aspects of quantitative MRI with a focus on signal perturbation related to data acquisition and the modelling of such signal. The common goal of the presented studies is to extend and increase the feasibility of using the MRI scanner as an objective measurement tool in the context of clinical routine or to assess response to potential therapies. The work undertaken led to the observation that well suited data (pre-) processing is essential in quantitative MRI for consistent estimation of tissue physiology. It can also lead to significant improvement of the accuracy of the parameters derived from image data. This is highly valuable in various applications such as treatment monitoring, early diagnosis in oncology or to get a better understanding of the development of tumours. An additional benefit related to the presented techniques may be the increase in correlation between diseases characteristics and MR parameters. Such an

effect could lead to more accurate assessment and benefit clinical trials by reducing the number of subjects required.

7.2 Future directions

A number of future directions might be considered. The use of RDDR is not limited to the applications presented in this thesis and can be extended to other imaging techniques that have common characteristics with DCE-MRI, such as DSC-MRI, Positron Emission Tomography or contrast enhanced CT. Investigating the ability of RDDR to register multiple measurements in DWI datasets (multiple directions of the diffusion gradient and multiple b-values) could be of interest as well.

A few refinements of the algorithm could also be of interest in future work: the use of robust data principal component analysis to decompose the imaged data requires a fine tuning of the trade-off parameter (as detailed in 4.3.4). Although satisfying results were obtained using the proposed heuristic, finding analytically suitable setting for the decomposition might further improve the performance of the algorithm.

DRAM provides a pipeline for respiratory motion correction followed by quantification of the remaining physiological motion (e.g. contractions and expansions of features). One of the potential alternative applications of this method could be the analysis of free breathing cardiac MRI. This could allow the assessment of myocardial function from data acquired over longer imaging periods. It could also remove the possible changes in heart beat and blood flow, due to stress and pressure changes caused by breath holding. Alternatively, it may allow for a wider gating window in respiratory gated scans, resulting in a more efficient use of the scan time.

The modelling of local AIF using diffusion requires more extensive investigation. Although promising results were obtained with the proposed heuristic, a complete validation is necessary to fully assess the potential benefit of such a model. The proposed method was

presented in the context of DCE-MRI only. However this, as well as RDDR, could be useful in other imaging techniques such as DSC-MRI.

7.3 Conclusions

This thesis has described a number of ways of improving the extraction of information from quantitative MRI through compensation of the effect of noise and motion, and further development of a perfusion model. Such improvements can be beneficial in several areas including oncology and clinical trials. More widespread adoption of the proposed methods and ideas through integration into data processing pipelines could have a significant impact on the clinical use of multi parametric MRI and on the use of imaging biomarkers in the assessment of diseases and treatment response.

Bibliography

[1] D. W. McRobbie, E. A. Moore, M. J. Graves, and M. R. Prince, *MRI from picture to proton*. New York: Cambridge University Press, 2007.

[2] P. C. Lauterbur, "Image Formation by Induced Local Interactions: Examples Employing Nuclear Magnetic Resonance," *Nature*, vol. 242, no. 5394. pp. 190–191, 1973.

[3] M. A. Griswold, P. M. Jakob, R. M. Heidemann, M. Nittka, V. Jellus, J. Wang, B. Kiefer, and A. Haase, "Generalized autocalibrating partially parallel acquisitions (GRAPPA).," *Magn. Reson. Med.*, vol. 47, no. 6, pp. 1202–10, Jun. 2002.

[4] K. P. Pruessmann, M. Weiger, M. B. Scheidegger, and P. Boesiger, "SENSE : Sensitivity Encoding for Fast MRI," *Magn. Reson. Med.*, vol. 42, no. 5, pp. 952–962, 1999.

[5] D. Le Bihan, E. Breton, D. Lallemand, P. Grenier, E. Cabanis, and M. Javal-Jeantet, "MR Imaging of Intravoxel Incoherent Motions: Application to Diffusion and Perfusion in Neurologic Disorders," *Radiology*, vol. 161, pp. 401–407, 1986.

[6] D. LeBihan, E. Breton, D. Lallemand, M.-L. Aubin, J. Vignaud, and M. Laval-Jeantet, "Separation of Diffusion and Perfusion in Intravoxel Incoherent Motion MR Imaging," *Radiology*, vol. 168, no. 2, pp. 497–505, 1988.

[7] K. M. Bennett, K. M. Schmainda, R. T. Bennett, D. B. Rowe, H. Lu, and J. S. Hyde, "Characterization of continuously distributed cortical water diffusion rates with a stretched-exponential model.," *Magn. Reson. Med.*, vol. 50, no. 4, pp. 727–34, Oct. 2003.

[8] P. S. Tofts and A. G. Kermode, "Measurement of the blood-brain barrier permeability and leakage space using dynamic MR imaging. 1. Fundamental concepts.," *Magn. Reson. Med.*, vol. 17, no. 2, pp. 357–367, 1991.

[9] S. Kety, "The theory and applications of the exchange of inert gas at the lungs and tissues," *Pharmacol. Rev.*, vol. 3, no. 1, pp. 1–41, 1951.

[10] S. P. Sourbron and D. L. Buckley, "On the scope and interpretation of the Tofts models for DCE-MRI.," *Magn. Reson. Med.*, vol. 66, no. 3, pp. 735–45, Sep. 2011.

[11] P. S. Tofts, "Modeling tracer kinetics in dynamic Gd-DTPA MR imaging," *J. Magn. Reson. Imaging*, vol. 7, no. 1, pp. 91–101, 1997.

[12] H. B. Larsson and P. S. Tofts, "Measurement of blood-brain barrier permeability using dynamic Gd-DTPA scanning--a comparison of methods.," *Magn. Reson. Med.*, vol. 24, no. 1, pp. 174–176, 1992.

[13] G. Brix, W. Semmler, R. Port, L. Schad, G. Layer, and W. Lorenz, "Pharmacokinetic parameters in CNS Gd-DTPA enhanced MR imaging," *J. Comput. Assist. Tomogr.*, vol. 15, no. 4, pp. 621–628, 1991.

[14] P. S. Tofts, G. Brix, D. L. Buckley, J. L. Evelhoch, E. Henderson, M. V Knopp, H. B. W. Larsson, T. Lee, N. a Mayr, G. J. M. Parker, R. E. Port, J. Taylor, and R. M. Weisskoff, "Contrast-Enhanced T 1 -Weighted MRI of a Diffusable Tracer : Standardized Quantities and Symbols," *J. Magn. Reson. Imaging*, vol. 10, pp. 223–232, 1999.

[15] S. P. Sourbron and D. L. Buckley, “Tracer kinetic modelling in MRI: estimating perfusion and capillary permeability.,” *Phys. Med. Biol.*, vol. 57, no. 2, pp. R1–R33, Jan. 2012.

[16] E. K. Fram, R. J. Herfkens, G. A. Johnson, G. H. Glover, J. P. Karis, A. N. N. Shimakawa, T. O. M. G. Perkins, and N. J. Pact, “Rapid calculation of T1 using variable flip angle gradient refocused imaging,” *Magn. Reson. Imaging*, vol. 5, pp. 201–208, 1987.

[17] D. C. Look and R. D. Locker, “Time Saving in Measurement of NMR and EPR Relaxation Times,” *Rev. Sci. Instrum.*, vol. 41, no. 2, p. 250, 1970.

[18] D. R. Messroghli, A. Radjenovic, S. Kozerke, D. M. Higgins, M. U. Sivananthan, and J. P. Ridgway, “Modified Look-Locker inversion recovery (MOLLI) for high-resolution T1 mapping of the heart.,” *Magn. Reson. Med.*, vol. 52, no. 1, pp. 141–6, Jul. 2004.

[19] A. Jackson, J. P. B. O’Connor, G. J. M. Parker, and G. C. Jayson, “Imaging tumor vascular heterogeneity and angiogenesis using dynamic contrast-enhanced magnetic resonance imaging.,” *Clin. Cancer Res.*, vol. 13, no. 12, pp. 3449–3459, Jun. 2007.

[20] B. Türkbey, D. Thomasson, Y. Pang, M. Bernardo, and P. L. Choyke, “The role of dynamic contrast-enhanced MRI in cancer diagnosis and treatment.,” *Diagnostic Interv. Radiol. Ankara Turkey*, vol. 16, no. 3, pp. 186–192, Sep. 2010.

[21] M. O. Leach, K. M. Brindle, J. L. Evelhoch, J. R. Griffiths, M. R. Horsman, a Jackson, G. C. Jayson, I. R. Judson, M. V Knopp, R. J. Maxwell, D. McIntyre, a R. Padhani, P. Price, R. Rathbone, G. J. Rustin, P. S. Tofts, G. M. Tozer, W. Vennart, J. C. Waterton, S. R. Williams, and P. Workman, “The assessment of antiangiogenic and antivascular therapies in early-stage clinical trials using magnetic resonance imaging: issues and recommendations.,” *Br. J. Cancer*, vol. 92, no. 9, pp. 1599–610, May 2005.

[22] P. S. Tofts, “T 1 -weighted DCE Imaging Concepts : Modelling , Acquisition and Analysis,” *Magnetom Flash*, vol. 45, no. 3, pp. 30–38, 2010.

[23] K. E. Bae, S. Y. Kim, S. S. Lee, K. W. Kim, H. J. Won, Y. M. Shin, P. N. Kim, and M.-G. Lee, “Assessment of hepatic function with Gd-EOB-DTPA-enhanced hepatic MRI.,” *Dig. Dis.*, vol. 30, no. 6, pp. 617–22, Jan. 2012.

[24] M. L. W. Ziech, C. Lavini, M. W. A. Caan, C. Y. Nio, P. C. F. Stokkers, S. Bipat, C. Y. Ponsioen, A. J. Nederveen, and J. Stoker, “Dynamic contrast-enhanced MRI in patients with luminal Crohn’s disease.,” *Eur. J. Radiol.*, vol. 81, no. 11, pp. 3019–27, Nov. 2012.

[25] D. Peruzzo, A. Bertoldo, F. Zanderigo, and C. Cobelli, “Automatic selection of arterial input function on dynamic contrast-enhanced MR images.,” *Comput. Methods Programs Biomed.*, vol. 104, no. 3, pp. e148–57, Dec. 2011.

[26] F. Calamante, “Bolus dispersion issues related to the quantification of perfusion MRI data.,” *J. Magn. Reson. Imaging*, vol. 22, no. 6, pp. 718–22, Dec. 2005.

[27] F. Calamante, P. J. Yim, and J. R. Cebral, “Estimation of bolus dispersion effects in perfusion MRI using image-based computational fluid dynamics,” *Neuroimage*, vol. 19, no. 2, pp. 341–353, Jun. 2003.

[28] F. Calamante, “Arterial input function in perfusion MRI: A comprehensive review.,” *Prog. Nucl. Magn. Reson. Spectrosc.*, vol. 74, pp. 1–32, Oct. 2013.

[29] F. Calamante, D. L. Thomas, G. S. Pell, J. Wiersma, and R. Turner, “Measuring cerebral blood flow using magnetic resonance imaging techniques.,” *J. Cereb. Blood Flow Metab.*, vol. 19, no. 7, pp. 701–35, Jul. 1999.

[30] J. M. Pollock, H. Tan, R. A. Kraft, C. T. Whitlow, J. H. Burdette, and J. A. Maldjian, “Arterial Spin Labeled MRI Perfusion Imaging: Clinical Applications,” *Magn. Reson. Imaging Clin. N. Am.*, vol. 17, no. 2, pp. 315–338, 2009.

[31] A. R. Deibler, J. M. Pollock, R. A. Kraft, H. Tan, J. H. Burdette, and J. A. Maldjian, “Arterial spin-labeling in routine clinical practice, part 1: technique and artifacts.,” *Am. J. Neuroradiol.*, vol. 29, no. 7, pp. 1228–34, Aug. 2008.

[32] J. M. Froehlich, M. a Patak, C. von Weymarn, C. F. Juli, C. L. Zollikofer, and K.-U. Wentz, “Small bowel motility assessment with magnetic resonance imaging.,” *J. Magn. Reson. Imaging*, vol. 21, no. 4, pp. 370–5, Apr. 2005.

[33] E. Husebye, “The patterns of small bowel motility: physiology and implications in organic disease and functional disorders.,” *Neurogastroenterol. Motil.*, vol. 11, no. 3, pp. 141–61, Jun. 1999.

[34] F. Odille, A. Menys, A. Ahmed, S. Punwani, S. A. Taylor, and D. Atkinson, “Quantitative assessment of small bowel motility by nonrigid registration of dynamic MR images,” *Magn. Reson. Med.*, vol. 68, no. 3, pp. 1–11, Sep. 2012.

[35] J. M. Froehlich, M. a Patak, C. von Weymarn, C. F. Juli, C. L. Zollikofer, and K.-U. Wentz, “Small bowel motility assessment with magnetic resonance imaging.,” *J. Magn. Reson. Imaging*, vol. 21, no. 4, pp. 370–5, Apr. 2005.

[36] A. Menys, S. A. Taylor, A. Emmanuel, A. Ahmed, A. A. Plumb, and F. Odille, “Global Small Bowel Motility : Assessment with Dynamic MR Imaging,” *Radiology*, vol. 269, no. 2, pp. 443–450, 2013.

[37] A. Menys, D. Atkinson, F. Odille, A. Ahmed, M. Novelli, M. Rodriguez-Justo, I. Proctor, S. Punwani, S. Halligan, and S. A. Taylor, “Quantified terminal ileal motility during MR enterography as a potential biomarker of Crohn’s disease activity: a preliminary study.,” *Eur. Radiol.*, vol. 22, no. 11, pp. 2494–501, Nov. 2012.

[38] J. V. Hajnal, D. J. Hawkes, and D. L. G. Hill, “Medical Image Registration,” *Phys. Med. Biol.*, vol. 46, pp. R1–R45, 2001.

[39] D. L. Donoho, “Compressed sensing,” *Ieee Trans. Inf. Theory*, vol. 52, pp. 1289–1306, 2006.

[40] M. L. Wood, “MR image artifacts from periodic motion,” *Med. Phys.*, vol. 12, no. 2, p. 143, 1985.

[41] F. Odille, P.-A. Vuissoz, P.-Y. Marie, and J. Felblinger, “Generalized reconstruction by inversion of coupled systems (GRICS) applied to free-breathing MRI.,” *Magn. Reson. Med.*, vol. 60, no. 1, pp. 146–157, Jul. 2008.

[42] A. Lemke, B. Stieltjes, L. R. Schad, and F. B. Laun, “Toward an optimal distribution of b values for intravoxel incoherent motion imaging.,” *Magn. Reson. Imaging*, vol. 29, no. 6, pp. 766–776, 2011.

[43] M. R. Orton, K. Miyazaki, D.-M. Koh, D. J. Collins, D. J. Hawkes, D. Atkinson, and M. O. Leach, "Optimizing functional parameter accuracy for breath-hold DCE-MRI of liver tumours.," *Phys. Med. Biol.*, vol. 54, no. 7, pp. 2197–2215, Apr. 2009.

[44] J. Ferlay, H.-R. Shin, F. Bray, D. Forman, C. Mathers, and D. M. Parkin, "Estimates of worldwide burden of cancer in 2008: GLOBOCAN 2008.," *Int. J. Cancer*, vol. 127, no. 12, pp. 2893–917, Dec. 2010.

[45] E. M. Charles-Edwards and N. M. DeSouza, "Diffusion-weighted magnetic resonance imaging and its application to cancer," *Cancer Imaging*, vol. 6, no. 1, pp. 135–143, Jan. 2006.

[46] K. Kitajima, Y. Kaji, Y. Fukabori, K. Yoshida, N. Suganuma, and K. Sugimura, "Prostate cancer detection with 3 T MRI: comparison of diffusion-weighted imaging and dynamic contrast-enhanced MRI in combination with T2-weighted imaging.," *J. Magn. Reson. Imaging*, vol. 31, no. 3, pp. 625–31, Mar. 2010.

[47] B. Zelhof, M. Pickles, G. Liney, P. Gibbs, G. Rodrigues, S. Kraus, and L. Turnbull, "Correlation of diffusion-weighted magnetic resonance data with cellularity in prostate cancer.," *BJU Int.*, vol. 103, no. 7, pp. 883–888, Apr. 2009.

[48] S. Verma, A. Rajesh, H. Morales, L. Lemen, G. Bills, M. Delworth, K. Gaitonde, J. Ying, R. Samartunga, and M. Lamba, "Assessment of aggressiveness of prostate cancer: correlation of apparent diffusion coefficient with histologic grade after radical prostatectomy.," *Ajr Am. J. Roentgenol.*, vol. 196, no. 2, pp. 374–381, Feb. 2011.

[49] N. Dikaios, S. Punwani, V. Hamy, P. Purpura, H. Fitzke, S. Rice, S. Taylor, and D. Atkinson, "Maximum likelihood ADC parameter estimates improve selection of metastatic cervical nodes for patients with head and neck squamous cell cancer," in *Proceedings of the International Society of Magnetic Resonance in Medicine*, 2012, vol. 62, no. 2, p. 3653.

[50] S. Chawla, S. Kim, L. Dougherty, S. Wang, L. A. Loevner, H. Quon, and H. Poptani, "Pretreatment diffusion-weighted and dynamic contrast-enhanced MRI for prediction of local treatment response in squamous cell carcinomas of the head and neck.," *Am. J. Roentgenol.*, vol. 200, no. 1, pp. 35–43, 2013.

[51] S. Walker-Samuel, M. Orton, L. D. McPhail, and S. P. Robinson, "Robust Estimation of the Apparent Diffusion Coefficient (ADC) in Heterogeneous Solid Tumors," *Magn. Reson. Med.*, vol. 62, no. 2, pp. 420–429, Aug. 2009.

[52] V. Hamy, S. Walker-Samuel, S. Punwani, and D. Atkinson, "Comparison of Least Squares and Maximum Likelihood for Apparent Diffusion Coefficient Estimation in Prostate DW-MRI," in *Medical Image Understanding and Analysis*, 2011, no. 1.

[53] V. Hamy, S. Walker-Samuel, D. Atkinson, and S. Punwani, "Comparison of least squares and maximum likelihood for apparent diffusion coefficient estimation in prostate diffusion-weighted MRI (DW-MRI)," in *Proceedings of RSNA*, 2011.

[54] V. Hamy, S. Walker-Samuel, D. Atkinson, and S. Punwani, "Apparent diffusion coefficient estimation in prostate DW-MRI using maximum likelihood.," in *Proceedings of the International Society of Magnetic Resonance in Medicine*, 2012, vol. 62, no. 2, p. 1854.

[55] N. Dikaios, S. Punwani, V. Hamy, P. Purpura, S. Rice, M. Forster, R. Mendes, S. Taylor, and D. Atkinson, "Noise estimation from averaged diffusion weighted images: Can unbiased quantitative decay parameters assist cancer evaluation?," *Magn. Reson. Med.*, p. In press.

[56] R. M. Henkelman, "Measurement of Signal intensities in the presence of noise in MR images," *Med. Phys.*, vol. 12, no. 2, pp. 232–233, 1985.

[57] H. Gudbjartsson and S. Patz, "The rician distribution of noisy MR data," *Magn. Reson. Med.*, vol. 34, pp. 910–914, 1995.

[58] O. Dietrich, J. G. Raya, S. B. Reeder, M. Ingrisch, M. F. Reiser, and S. O. Schoenberg, "Influence of multichannel combination, parallel imaging and other reconstruction techniques on MRI noise characteristics.," *Magn. Reson. Imaging*, vol. 26, no. 6, pp. 754–762, Jul. 2008.

[59] O. Dietrich, J. G. Raya, S. B. Reeder, M. Ingrisch, M. F. Reiser, and S. O. Schoenberg, "Influence of multichannel combination, parallel imaging and other reconstruction techniques on MRI noise characteristics.," *Magn. Reson. Imaging*, vol. 26, no. 6, pp. 754–762, Jul. 2008.

[60] S. Aja-Fernández and A. Tristán-Vega, "Influence of noise correlation in multiple-coil statistical models with sum of squares reconstruction.," *Magn. Reson. Med.*, vol. 67, no. 2, pp. 580–5, Feb. 2012.

[61] A. Kristoffersen, "Optimal estimation of the diffusion coefficient from non-averaged and averaged noisy magnitude data.," *J. Magn. Reson.*, vol. 187, no. 2, pp. 293–305, Aug. 2007.

[62] C. D. Constantinides, E. Atalar, and E. R. McVeigh, "Signal-to-noise measurements in magnitude images from NMR phased arrays.," *Magn. Reson. Med.*, vol. 38, no. 5, pp. 852–857, 1997.

[63] S. Aja-Fernández, A. Tristán-Vega, and W. S. Hoge, "Statistical noise analysis in GRAPPA using a parametrized noncentral Chi approximation model.," *Magn. Reson. Med.*, vol. 65, no. 4, pp. 1195–1206, May 2011.

[64] C. G. Koay and P. J. Basser, "Analytically exact correction scheme for signal extraction from noisy magnitude MR signals.," *J. Magn. Reson.*, vol. 179, no. 2, pp. 317–322, Apr. 2006.

[65] P. Coupé, J. V Manjón, E. Gedamu, D. Arnold, M. Robles, and D. L. Collins, "Robust Rician noise estimation for MR images.," *Med. Image Anal.*, vol. 14, no. 4, pp. 483–93, Aug. 2010.

[66] J. Sijbers, a J. Den Dekker, P. Scheunders, and D. Van Dyck, "Maximum-likelihood estimation of Rician distribution parameters," *IEEE Trans. Med. Imaging*, vol. 17, no. 3, pp. 357–361, 1998.

[67] A. Cardenas-Blanco, M. Nezamzadeh, C. Fottit, and I. Cameron, "Accurate Noise Bias Correction Applied to Individual Pixels," in *Proceedings of the International Society of Magnetic Resonance in Medicine*, 2007, vol. 03, no. 2, p. 3445.

[68] E. Olariu, A. Cardenas-Blanco, and I. Cameron, "Noise Bias Correction for Signal Averaged Images," in *Proceedings of the International Society of Magnetic Resonance in Medicine*, 2009, vol. 12, no. 2, p. 4651.

[69] J. Ren, Y. Huan, H. Wang, H. Zhao, Y. Ge, Y. Chang, and Y. Liu, “Diffusion-weighted imaging in normal prostate and differential diagnosis of prostate diseases.,” *Abdom. Imaging*, vol. 33, no. 6, pp. 724–728, 2008.

[70] T. Tamada, T. Sone, Y. Jo, S. Toshimitsu, T. Yamashita, A. Yamamoto, D. Tanimoto, and K. Ito, “Apparent diffusion coefficient values in peripheral and transition zones of the prostate: comparison between normal and malignant prostatic tissues and correlation with histologic grade.,” *J. Magn. Reson. Imaging*, vol. 28, no. 3, pp. 720–6, Sep. 2008.

[71] H. U. Ahmed, Y. Hu, T. Carter, N. Arumainayagam, E. Lecornet, A. Freeman, D. Hawkes, D. C. Barratt, and M. Emberton, “Characterizing clinically significant prostate cancer using template prostate mapping biopsy.,” *J. Urol.*, vol. 186, no. 2, pp. 458–64, Aug. 2011.

[72] J. J. Meeks, C. S. Thaxton, S. Loeb, K. a Roehl, B. T. Helfand, and W. J. Catalona, “Comparison of prostate specific antigen velocity in screened versus referred patients with prostate cancer.,” *J. Urol.*, vol. 179, no. 4, pp. 1340–3, Apr. 2008.

[73] J. M. Mayes, V. Mouraviev, L. Sun, M. Tsivian, J. F. Madden, and T. J. Polascik, “Can the conventional sextant prostate biopsy accurately predict unilateral prostate cancer in low-risk, localized, prostate cancer?,” *Urol. Oncol.*, vol. 29, no. 2, pp. 166–70, 2011.

[74] H. U. Ahmed, A. Kirkham, M. Arya, R. Illing, A. Freeman, C. Allen, and M. Emberton, “Is it time to consider a role for MRI before prostate biopsy?,” *Nat. Rev. Clin. Oncol.*, vol. 6, no. 4, pp. 197–206, Apr. 2009.

[75] W. E. Barzell and M. R. Melamed, “Appropriate patient selection in the focal treatment of prostate cancer: the role of transperineal 3-dimensional pathologic mapping of the prostate--a 4-year experience.,” *Urology*, vol. 70, no. 6 Suppl, pp. 27–35, Dec. 2007.

[76] V. a Morgan, S. Kyriazi, S. E. Ashley, and N. M. DeSouza, “Evaluation of the potential of diffusion-weighted imaging in prostate cancer detection.,” *Acta Radiol. Stock. Sweden 1987*, vol. 48, no. 6, pp. 695–703, Jul. 2007.

[77] M. Sumi, N. Sakihama, T. Sumi, M. Morikawa, M. Uetani, H. Kabasawa, K. Shigeno, K. Hayashi, H. Takahashi, and T. Nakamura, “Discrimination of metastatic cervical lymph nodes with diffusion-weighted MR imaging in patients with head and neck cancer.,” *Am. J. Neuroradiol.*, vol. 24, no. 8, pp. 1627–1634, 2003.

[78] J. Wang, S. Takashima, F. Takayama, S. Kawakami, A. Saito, T. Matsushita, M. Momose, and T. Ishiyama, “Head and neck lesions: characterization with diffusion-weighted echo-planar MR imaging.,” *Radiology*, vol. 220, no. 3, pp. 621–630, 2001.

[79] A. R. Padhani, G. Liu, D. Mu-koh, T. L. Chenevert, H. C. Thoeny, B. D. Ross, M. Van Cauteren, D. Collins, D. A. Hammoud, G. J. S. Rustin, and B. Taouli, “Diffusion-Weighted Magnetic Resonance Imaging as a Cancer Biomarker : Consensus and Recommendations,” *Neoplasia*, vol. 11, no. 2, pp. 102–125, 2009.

[80] V. Hamy, A. Melbourne, B. Trémoulhéac, S. Punwani, and D. Atkinson, “Registration of DCE-MRI using Robust Data Decomposition,” in *Proceedings of the International Society of Magnetic Resonance in Medicine*, 2012, vol. 29, no. 11, p. 2197.

[81] V. Hamy, S. Punwani, J. Makanyanga, S. Taylor, and D. Atkinson, “Motion Correction in Small Bowel DCE-MRI using Robust Data Decomposition Registration,” in *Proceedings of the International Society of Magnetic Resonance in Medicine*, 2013, vol. 81, no. 2, p. 3686.

[82] V. Hamy, N. Dikaios, S. Punwani, A. Melbourne, A. Latifoltojar, J. Makanyanga, M. Chouhan, E. Helbren, A. Menys, S. Taylor, and D. Atkinson, “Respiratory Motion Correction in Dynamic MRI using Robust Data Decomposition Registration – Application to DCE-MRI,” *Med. Image Anal.*, vol. 18, no. 2, pp. 301–313, Nov. 2014.

[83] C. Plathow, S. Ley, C. Fink, M. Puderbach, W. Hosch, A. Schmähl, J. Debus, and H.-U. Kauczor, “Analysis of intrathoracic tumor mobility during whole breathing cycle by dynamic MRI.,” *Int. J. Radiat. Oncol. Biol. Phys.*, vol. 59, no. 4, pp. 952–9, Jul. 2004.

[84] M. Filipovic, P. Vuissoz, a Codreanu, M. Claudon, and J. Felblinger, “Motion compensated generalized reconstruction for free-breathing dynamic contrast-enhanced MRI.,” *Magn. Reson. Med.*, vol. 65, no. 3, pp. 812–822, Mar. 2011.

[85] C. Studholme, D. L. G. Hill, and D. J. Hawkes, “An overlap invariant entropy measure of 3D medical image alignment,” *Pattern Recognit.*, vol. 32, no. 1, pp. 71–86, Jan. 1999.

[86] T. Rohlfing, C. R. Maurer, D. a Bluemke, and M. a Jacobs, “Volume-preserving nonrigid registration of MR breast images using free-form deformation with an incompressibility constraint.,” *IEEE Trans. Med. Imaging*, vol. 22, no. 6, pp. 730–41, Jun. 2003.

[87] S. Marsland, C. J. Twining, and C. J. Taylor, “Groupwise non-rigid registration using polyharmonic clamped-plate splines,” in *Proceedings of Medical Image Computing and Computer-Assisted Intervention*, 2003, pp. 771–779.

[88] C. Tanner, J. A. Schnabel, D. L. G. Hill, D. J. Hawkes, A. Degenhard, M. O. Leach, D. R. Hose, M. a Hall-Craggs, and S. I. Usiskin, “Quantitative evaluation of free-form deformation registration for dynamic contrast-enhanced MR mammography.,” *Med. Phys.*, vol. 34, no. 4, pp. 1221–1233, 2007.

[89] D. Rueckert, L. I. Sonoda, C. Hayes, D. L. G. Hill, M. O. Leach, and D. J. Hawkes, “Nonrigid registration using free-form deformations: application to breast MR images,” *IEEE Trans. Med. Imaging*, vol. 18, no. 8, pp. 712–721, 1999.

[90] C. Tanner, J. A. Schnabel, D. Chung, M. J. Clarkson, D. Rueckert, and D. L. G. Hill, “Volume and Shape Preservation of Enhancing Lesions when Applying Non-rigid Registration to a Time Series of Contrast Enhancing MR Breast Images,” in *Proceedings of Medical Image Computing and Computer-Assisted Intervention*, 2000, pp. 327–337.

[91] Y. Zheng, A. D. A. Maidment, and J. C. Gee, “Accurate registration of dynamic contrast-enhanced breast MR images with robust estimation and linear programming,” in *Proceedings of IEEE International Conference on Biomedical Imaging*, 2010, pp. 536–539.

[92] Z. Li, M. Caan, M. L. W. Ziech, and J. Stoker, “3D non-rigid motion correction of free-breathing abdominal DCE-MRI data,” in *Proceedings of Medical Image Computing and Computer-Assisted Intervention*, 2012, vol. 7029, pp. 44–50.

[93] J. Ashburner and K. J. Friston, “Spatial Normalization using Basis Functions,” *Hum. Brain Mapp.*, vol. 7, pp. 254–266, 2003.

[94] P. Hayton, M. Brady, L. Tarassenko, and N. Moore, “Analysis of dynamic MR breast images using a model of contrast enhancement.,” *Med. Image Anal.*, vol. 1, no. 3, pp. 207–224, 1997.

[95] C. Xiaohua, M. Brady, J. L.-C. Lo, and N. Moore, “Simultaneous segmentation and registration of contrast-enhanced breast MRI.,” in *Procceding of Information Processing in Medical Imaging*, 2005, vol. 19, pp. 126–137.

[96] G. a Buonaccorsi, J. P. B. O’Connor, A. Caunce, C. Roberts, S. Cheung, Y. Watson, K. Davies, L. Hope, A. Jackson, G. C. Jayson, and G. J. M. Parker, “Tracer kinetic model-driven registration for dynamic contrast-enhanced MRI time-series data.,” *Magn. Reson. Med.*, vol. 58, no. 5, pp. 1010–1019, Nov. 2007.

[97] M. Bhushan, J. A. Schnabel, L. Risser, M. P. Heinrich, J. M. Brady, and M. Jenkinson, “Motion Correction and Parameter Estimation in dceMRI Sequences: Application to Colorectal Cancer,” in *Proceedings of Medical Image Computing and Computer-Assisted Intervention*, 2011, vol. 6891, no. Pt 1, pp. 476–483.

[98] A. Melbourne, D. Atkinson, M. White, D. Collins, M. Leach, and D. J. Hawkes, “Registration of dynamic contrast-enhanced MRI using a progressive principal component registration (PPCR),” *Phys. Med. Biol.*, vol. 52, no. 17, pp. 5147–5156, Sep. 2007.

[99] A. Melbourne, J. Hipwell, M. Modat, T. Mertzanidou, H. Huisman, S. Ourselin, and D. J. Hawkes, “The effect of motion correction on pharmacokinetic parameter estimation in dynamic-contrast-enhanced MRI.,” *Phys. Med. Biol.*, vol. 56, no. 24, pp. 7693–708, Dec. 2011.

[100] M. Modat, G. R. Ridgway, Z. a Taylor, M. Lehmann, J. Barnes, D. J. Hawkes, N. C. Fox, and S. Ourselin, “Fast free-form deformation using graphics processing units,” *Comput. Methods Programs Biomed.*, vol. 98, no. 3, pp. 278–284, 2010.

[101] G. Wollny, P. Kellman, A. Santos, and M. J. Ledesma-Carbayo, “Automatic motion compensation of free breathing acquired myocardial perfusion data by using independent component analysis.,” *Med. Image Anal.*, vol. 16, no. 5, pp. 1015–28, Jul. 2012.

[102] E. J. Candès, X. Li, Y. Ma, and J. Wright, “Robust Principal Component Analysis?,” *J. ACM*, vol. 58, no. 3, pp. 1–37, Dec. 2011.

[103] A. Myronenko and X. Song, “Intensity-Based Image Registration by Minimizing Residual Complexity,” *IEEE Trans. Med. Imaging*, vol. 29, no. 11, pp. 1882–1891, 2010.

[104] V. Chandrasekaran, S. Sanghavi, P. A. Parrilo, and A. S. Willsky, “Rank-Sparsity Incoherence for Matrix Decomposition,” *SIAM J. Optim.*, vol. 02139, no. 2, pp. 572–596, 2009.

[105] X. Yuan and J. Yang, “Sparse and low-rank matrix decomposition via alternating direction methods,” *Convergence*, vol. Preprint, pp. 1–11, 2009.

[106] Z. Lin, M. Chen, and L. Wu, “The Augmented Lagrange Multiplier Method for Exact Recovery of Corrupted Low-Rank Matrices,” Cornell University Library, 2010.

[107] R. M. Larsen, “Lanczos bidiagonalization algorithm with partial reorthogonalization,” 1998.

[108] Y. Peng, A. Ganesh, J. Wright, W. Xu, and Y. Ma, “RASL: robust alignment by sparse and low-rank decomposition for linearly correlated images.,” *IEEE Trans. Pattern Anal. Mach. Intell.*, vol. 34, no. 11, pp. 2233–46, Nov. 2012.

[109] R. Otazo, D. K. Sodickson, and E. J. Candès, “Low-rank + sparse (L+S) reconstruction for accelerated dynamic MRI with seperation of background and dynamic components,” vol. 8858, no. 88581Z, pp. 1–8, Sep. 2013.

[110] N. Dikaios, B. Tremoulheac, A. Menys, V. Hamy, and S. Arridge, “Joint reconstruction of low-rank and sparse components from undersampled (k , t) -space small bowel data,” in *IEEE Nuclear Science Symposium and Medical Imaging*, 2013, p. in press.

[111] G. J. M. Parker, C. Roberts, A. Macdonald, G. a Buonaccorsi, S. Cheung, D. L. Buckley, A. Jackson, Y. Watson, K. Davies, and G. C. Jayson, “Experimentally-derived functional form for a population-averaged high-temporal-resolution arterial input function for dynamic contrast-enhanced MRI.,” *Magn. Reson. Med.*, vol. 56, no. 5, pp. 993–1000, Nov. 2006.

[112] A. Melbourne, D. Atkinson, and D. J. Hawkes, “Influence of organ motion and contrast enhancement on image registration.,” in *Proceedings of Medical Image Computing and Computer-Assisted Intervention*, 2008, vol. 11, no. Pt 2, pp. 948–955.

[113] M. Medved, G. Karczmar, C. Yang, J. Dignam, T. F. Gajewski, H. Kindler, E. Vokes, P. MacEneany, M. T. Mitchell, and W. M. Stadler, “Semiquantitative analysis of dynamic contrast enhanced MRI in cancer patients: Variability and changes in tumor tissue over time.,” *J. Magn. Reson. Imaging*, vol. 20, no. 1, pp. 122–128, 2004.

[114] D. Balvay, F. Frouin, G. Calmon, B. Bessoud, E. Kahn, N. Siauve, O. Clément, and C. a Cuenod, “New criteria for assessing fit quality in dynamic contrast-enhanced T1-weighted MRI for perfusion and permeability imaging.,” *Magn. Reson. Med.*, vol. 54, no. 4, pp. 868–77, Oct. 2005.

[115] V. Hamy, A. Menys, E. Helbren, F. Odille, S. Taylor, and D. Atkinson, “Respiratory Motion Correction in Dynamic-MRI : Application to Small Bowel Motility Quantification during Free Breathing,” in *Proceedings of Medical Image Computing and Computer-Assisted Intervention*, 2013, vol. 8150, pp. 132–140.

[116] A. Menys, V. Hamy, C. Hoad, J. Makanyanga, F. Odille, P. Gowland, S. A. Taylor, and D. Atkinson, “Dual Registration of Abdominal Motion in free-breathing data sets acquired using dynamic MRI,” in *Proceedings of the International Society of Magnetic Resonance in Medicine*, 2014, vol. 22, no. 11, p. 2494.

[117] H. Caroline, A. Menys, and V. Hamy, “Colonic Motiliy Abstract,” in *Proceedings of the International Society of Magnetic Resonance in Medicine*, 2014, vol. 142.

[118] J. M. Froehlich, C. Waldherr, C. Stoupis, S. M. Erturk, and M. A. Patak, “MR motility imaging in Crohn’s disease improves lesion detection compared with standard MR imaging.,” *Eur. Radiol.*, vol. 20, no. 8, pp. 1945–1951, 2010.

[119] M. Pimentel, E. E. Soffer, E. J. Chow, Y. Kong, and H. C. Lin, “Lower frequency of MMC is found in IBS subjects with abnormal lactulose breath test, suggesting bacterial overgrowth.,” *Dig. Dis. Sci.*, vol. 47, no. 12, pp. 2639–2643, 2002.

[120] J. M. Fell, V. V Smith, and P. J. Milla, *Infantile chronic idiopathic intestinal pseudo-obstruction: the role of small intestinal manometry as a diagnostic tool and prognostic indicator.*, vol. 39, no. 2. 1996, pp. 306–311.

[121] R. F. Pfeiffer, "Gastrointestinal, urological, and sexual dysfunction in Parkinson's disease.," *Mov. Disord.*, vol. 25 Suppl 1, pp. S94–S97, 2010.

[122] M. Camilleri, W. L. Hasler, H. P. Parkman, E. M. Quigley, and E. Soffer, "Measurement of gastrointestinal motility in the GI laboratory.," *Gastroenterology*, vol. 115, no. 3, pp. 747–762, 1998.

[123] A. M. J. Sprengers, M. P. Van Der Paardt, F. M. Zijta, M. W. A. Caan, R. M. Lamerichs, A. J. Nederveen, and J. Stoker, "Use of continuously MR tagged imaging for automated motion assessment in the abdomen: A feasibility study.," *J. Magn. Reson. Imaging*, vol. 36, no. 2, pp. 492–7, 2012.

[124] S. Bickelhaupt, R. Cattin, J. M. Froehlich, S. Raible, H. Bouquet, U. Bill, and M. a Patak, "Automatic detection of small bowel contraction frequencies in motility plots using lomb-scargle periodogram and sinus-fitting method-initial experience.," *Magn. Reson. Med.*, vol. 71, no. 2, pp. 628–634, 2013.

[125] V. Hamy, M. Modat, N. Dikaios, J. Cleary, S. Punwani, R. Shipley, S. Ourselin, D. Atkinson, and A. Melbourne, "Multi-modal pharmacokinetic modelling for DCE-MRI : using diffusion weighted imaging to constrain the local arterial input function," in *SPIE Medical Imaging*, 2014, no. Ivim.

[126] P. S. Tofts, G. Brix, D. L. Buckley, J. L. Evelhoch, E. Henderson, M. V Knopp, H. B. W. Larsson, T. Lee, N. a Mayr, G. J. M. Parker, R. E. Port, J. Taylor, and R. M. Weisskoff, "Contrast-Enhanced T 1 -Weighted MRI of a Diffusable Tracer : Standardized Quantities and Symbols," *Imaging*, vol. 232, no. 3, pp. 223–232, 1999.

[127] Orton, J. d'Arcy, S. Walker-Samuel, D. Hawkes, D. Atkinson, D. Collins, and M. Leach, "Computationally efficient vascular input function models for quantitative kinetic modelling using DCE-MRI.," *Phys. Med. Biol.*, vol. 53, no. 5, pp. 1225–1239, Mar. 2008.

[128] K. Murase, K. Kikuchi, H. Miki, T. Shimizu, and J. Ikezoe, "Determination of arterial input function using fuzzy clustering for quantification of cerebral blood flow with dynamic susceptibility contrast-enhanced MR imaging.," *J. Magn. Reson. Imaging*, vol. 13, no. 5, pp. 797–806, May 2001.

[129] K. Mouridsen, S. Christensen, L. Gyldensted, and L. Ostergaard, "Automatic selection of arterial input function using cluster analysis.," *Magn. Reson. Med.*, vol. 55, no. 3, pp. 524–31, Mar. 2006.

[130] L. Shi, D. Wang, W. Liu, K. Fang, Y.-X. J. Wang, W. Huang, A. D. King, P. A. Heng, and A. T. Ahuja, "Automatic detection of arterial input function in dynamic contrast enhanced MRI based on affinity propagation clustering.," *J. Magn. Reson. Imaging*, pp. 1–11, Oct. 2013.

[131] J. U. Fluckiger, M. C. Schabel, and E. V. R. Dibella, "Model-based blind estimation of kinetic parameters in dynamic contrast enhanced (DCE)-MRI.," *Magn. Reson. Med.*, vol. 62, no. 6, pp. 1477–86, Dec. 2009.

[132] J. U. Fluckiger, M. C. Schabel, and E. V. R. DiBella, “Toward local arterial input functions in dynamic contrast-enhanced MRI.,” *J. Magn. Reson. Imaging*, vol. 32, no. 4, pp. 924–34, Oct. 2010.

[133] Y.-S. Kim, H. K. Lim, J.-H. Kim, H. Rhim, B. K. Park, B. Keserci, M. O. Köhler, D.-S. Bae, B.-G. Kim, J.-W. Lee, T.-J. Kim, S. Sokka, and J. H. Lee, “Dynamic Contrast-Enhanced Magnetic Resonance Imaging Predicts Immediate Therapeutic Response of Magnetic Resonance-Guided High-Intensity Focused Ultrasound Ablation of Symptomatic Uterine Fibroids,” *Invest. Radiol.*, vol. 46, no. 10, pp. 639–47, 2011.

[134] T. E. Yankeelov, M. Lepage, A. Chakravarthy, E. E. Broome, K. J. Niermann, M. C. Kelley, I. Meszoely, I. a Mayer, C. R. Herman, K. McManus, R. R. Price, and J. C. Gore, “Integration of quantitative DCE-MRI and ADC mapping to monitor treatment response in human breast cancer: initial results.,” *Magn. Reson. Imaging*, vol. 25, no. 1, pp. 1–13, Jan. 2007.

[135] K. Mouridsen, K. Friston, N. Hjort, L. Gyldensted, L. Østergaard, and S. Kiebel, “Bayesian estimation of cerebral perfusion using a physiological model of microvasculature.,” *Neuroimage*, vol. 33, no. 2, pp. 570–9, Nov. 2006.

[136] J. U. Fluckiger, M. E. Loveless, S. L. Barnes, M. Lepage, and T. E. Yankeelov, “A diffusion-compensated model for the analysis of DCE-MRI data : theory , simulations and experimental results,” *Phys. Med. Biol.*, vol. 58, pp. 1983–1998, 2013.

[137] S. P. Li and A. R. Padhani, “Tumor response assessments with diffusion and perfusion MRI.,” *J. Magn. Reson. Imaging*, vol. 35, no. 4, pp. 745–63, Apr. 2012.

[138] T. T. Batchelor, D. G. Duda, E. di Tomaso, M. Ancukiewicz, S. R. Plotkin, E. Gerstner, A. F. Eichler, J. Drappatz, F. H. Hochberg, T. Benner, D. N. Louis, K. S. Cohen, H. Chea, A. Exarhopoulos, J. S. Loeffler, M. a Moses, P. Ivy, a G. Sorensen, P. Y. Wen, and R. K. Jain, “Phase II study of cediranib, an oral pan-vascular endothelial growth factor receptor tyrosine kinase inhibitor, in patients with recurrent glioblastoma.,” *J. Clin. Oncol.*, vol. 28, no. 17, pp. 2817–23, Jun. 2010.

[139] Orton, J. d’Arcy, S. Walker-Samuel, D. Hawkes, D. Atkinson, D. Collins, and M. Leach, “Computationally efficient vascular input function models for quantitative kinetic modelling using DCE-MRI.,” *Phys. Med. Biol.*, vol. 53, no. 5, pp. 1225–1239, Mar. 2008.

[140] Orton, J. d’Arcy, S. Walker-Samuel, D. Hawkes, D. Atkinson, D. Collins, and M. Leach, “Computationally efficient vascular input function models for quantitative kinetic modelling using DCE-MRI.,” *Phys. Med. Biol.*, vol. 53, no. 5, pp. 1225–1239, Mar. 2008.

[141] J. Yuan, S. K. K. Chow, D. K. W. Yeung, A. T. Ahuja, and A. D. King, “Quantitative evaluation of dual-flip-angle T1 mapping on DCE-MRI kinetic parameter estimation in head and neck.,” *Quant. Imaging Med. Surg.*, vol. 2, no. 4, pp. 245–53, Dec. 2012.

[142] P. Di Giovanni, C. a Azlan, T. S. Ahearn, S. I. Semple, F. J. Gilbert, and T. W. Redpath, “The accuracy of pharmacokinetic parameter measurement in DCE-MRI of the breast at 3 T.,” *Phys. Med. Biol.*, vol. 55, no. 1, pp. 121–32, Jan. 2010.

[143] P. Vajkoczy, H. Roth, P. Horn, T. Lucke, C. Thomé, U. Hubner, G. T. Martin, C. Zappletal, E. Klar, L. Schilling, and P. Schmiedek, “Continuous monitoring of regional cerebral blood flow: experimental and clinical validation of a novel thermal diffusion microprobe,” *J. Neurosurg.*, vol. 93, no. 2, pp. 265–274, 2000.